

UCLA

UCLA Electronic Theses and Dissertations

Title

Scalability of Superconducting Qubits for Noisy Intermediate Scale Quantum Computers

Permalink

<https://escholarship.org/uc/item/28z443wg>

Author

Banerjee, Ananyo

Publication Date

2023

Peer reviewed|Thesis/dissertation

UNIVERSITY OF CALIFORNIA

Los Angeles

Scalability of Superconducting Qubits for Noisy Intermediate Scale Quantum Computers

A thesis submitted in partial satisfaction

of the requirements for the degree

Master of Science in Electrical and Computer Engineering

by

Ananyo Banerjee

2023

© Copyright by  
Ananyo Banerjee  
2023

## ABSTRACT OF THE THESIS

Scalability of Superconducting Qubits for Noisy Intermediate Scale Quantum Computers

by

Ananyo Banerjee

Master of Science in Electrical and Computer Engineering

University of California, Los Angeles, 2023

Professor Chee Wei Wong, Chair

In the evolving landscape of quantum computing, the emergence of quantum computers in the Noisy Intermediate Scale Quantum (NISQ) regime marks a significant stride. Superconducting qubits have garnered popularity in both academic and industrial groups. However, the journey towards achieving a large-scale, fully error-corrected quantum computer faces challenges. This thesis addresses some of these challenges within an academic setup. One prominent challenge with superconducting qubits is Purcell decay. This work aims to tackle the issue by delving into the implementation of on-chip Purcell filters with Transmon qubits. The overarching goal is to pave the way for further scalability by ensuring compatibility of these designs with scalability plans. The thesis also introduces novel architectures for superconducting qudit processors, focusing on their already presented implementation in 3D cavities. Efforts are directed towards transitioning these processors to a planar platform for enhanced scalability. The coupling of these processors to environment is explored using coplanar waveguides, with the system's physics governed by the principles of circuit quantum electrodynamics. Finally, the thesis also delves into the packaging of planar qubit devices, aiming to facilitate easy scalability. This platform enables interfacing the devices with control equipment, shielding from stray fields, and offers the essential thermal link to the dilution refrigerator where they are housed. Each section of the thesis presents results emphasizing potential areas for improvement and refinement of the systems.

The thesis of Ananyo Banerjee is approved.

Sudhakar Pamarti

Kang L. Wang

Chee Wei Wong, Committee Chair

University of California, Los Angeles

2023

To my family and friends.

## TABLE OF CONTENTS

<b>1</b>	<b>Introduction</b>	<b>1</b>
1.1	What is Quantum Computing	2
1.1.1	Advantage	4
1.1.2	Current Architectures	5
1.1.3	Performance	10
1.1.4	Challenges	11
1.2	Scalability of Quantum Computers	12
1.2.1	Need for Scalability	12
1.2.2	Progress with Scalability and Future Plans	14
1.2.3	Roadblocks with Scalability	14
<b>2</b>	<b>Superconducting Qubits</b>	<b>17</b>
2.1	Physics of Oscillators	17
2.2	Josephson Junction	22
2.3	Transmon Qubit	23
2.4	Circuit Quantum Electrodynamics	26
<b>3</b>	<b>Methods</b>	<b>32</b>
3.1	Device Design and Simulation	32
3.1.1	Qiskit Metal	32
3.1.2	Lumped Oscillator Model	33
3.1.3	Energy Participation Ratio (EPR)	35
3.1.4	PCB Design and Simulation	38
3.2	Experimental Setup and Characterization Methodology	39

3.2.1	Measurement Setup and Dilution Fridge . . . . .	39
3.2.2	Josephson Parametric Amplifier . . . . .	41
<b>4</b>	<b>Planar Qubits . . . . .</b>	<b>47</b>
4.1	Planar qubit with on-chip Purcell Filters . . . . .	48
4.1.1	Transmon Qubit with a Notch Filter . . . . .	49
4.1.2	X-mon Qubit with a BandPass Filter . . . . .	52
<b>5</b>	<b>High Dimensional Qudit – Trimon . . . . .</b>	<b>56</b>
5.1	3D Trimon . . . . .	56
5.2	Planar Trimon . . . . .	58
<b>6</b>	<b>Multi-Planar Qubit Packaging . . . . .</b>	<b>62</b>
6.1	Existing Architecture . . . . .	63
6.2	Current Designs . . . . .	64
6.2.1	Packaging 2 Qubit Devices . . . . .	65
6.2.2	Packaging 8 Qubit Devices . . . . .	71
<b>7</b>	<b>Conclusion . . . . .</b>	<b>74</b>
7.1	Summary . . . . .	74
7.2	Scope of Improvement . . . . .	75
7.3	Outlook . . . . .	75
<b>A</b>	<b>Fabrication of Test Chips . . . . .</b>	<b>76</b>
	<b>References . . . . .</b>	<b>80</b>

## LIST OF FIGURES

1.1	Representing a qubit on a Bloch sphere. The conventional north pole of the Bloch sphere is assigned to the state $ 0\rangle$ , and correspondingly, the south pole to $ 1\rangle$ . The vector denotes the current state of the qubit, and any operation on the qubit moves the vector along the Bloch sphere. A common operation is to apply a $\pi$ -pulse, as illustrated in the figure. [1] . . . . .	4
1.2	Simplified stack for a superconducting qubit setup. Operating any quantum computing platform requires synchronization between numerous sophisticated control and measurement tools interacting with the physical qubit. Typically, the qubit is placed inside a dilution refrigerator to keep the devices isolated and at cryogenic temperatures. Image adapted from [2] . . . . .	6
1.3	Illustration of a fundamental difference in the energy level spacing in a quantum harmonic oscillator (QHO) formed by an LC circuit and the anharmonic oscillator by introducing a Josephson junction. (a) denotes an LC oscillator with inductance $L$ and capacitance $C$ . The phase on the superconducting island is denoted by $\phi$ , and the ground node is referenced to have a zero phase. (b) Energy levels of the LC oscillator (a). The energy levels in a QHO are equally spaced by $\hbar\omega$ , where $\omega = \sqrt{\frac{1}{LC}}$ . (c) represents a lumped element model of a superconducting qubit where the linear inductor is replaced by a Josephson junction of energy $E_J$ . (d) Illustrates the change in the harmonic potential with respect to a QHO (blue); this introduction of anharmonicity yields non-equal energy spacing necessary to operate a 2-level system.[3] . . .	7
1.4	Illustration of popular spin qubit configuration profiles and the corresponding energy levels and definition of each qubit state. (a) Loss-DiVincenzo qubit. (b) Singlet-triplet qubit. (c) Exchange-Only qubit. (d) Hybrid qubit with the same computational basis states. (e) Donor-bounded $e^-$ qubit. Image adapted from [4] . . . . .	8

1.5	Illustrates a trapped ion qubit’s state preparation, control, and readout. (a) State preparation involves optically pumping the ion to an ancillary state ( $ e\rangle_{SP}$ ) from the stable and long-lived state ( $ 0\rangle$ ), which rapidly decays to the state ( $ 1\rangle$ ). (b) The control of the qubit is achieved by coupling the states ( $ 0\rangle$ ) and ( $ 1\rangle$ ) using electric quadrupole transitions. (c) Readout of the state is achieved by shining light at the transition frequency of ( $ 1\rangle$ ) – ( $ e\rangle_R$ ) and observing the photons emitted from the transition decay (if any). [5] . . . . .	9
2.1	Extension of Figure 1.1. (a), (b) represents an LC quantum harmonic oscillator with phase on the island defined by $\phi$ and the corresponding energy level diagram for the QHO with energy subsequent levels spaced by $\hbar\omega_r$ , respectively. (c) and (d) represent replacing the linear inductor in the QHO by a Josephson Junction to introduce the effects of a non-linear inductor and the subsequent anharmonic oscillator with the two-lowest energy levels forming the computational subspace with the unequal energy spacing $\hbar\omega_{01}$ and $\hbar\omega_{12}$ . [6]	19
2.2	Simplified illustration of a Josephson junction depicts two superconducting electrodes separated by a thin layer of insulator, allowing electrons to quantum-mechanically tunnel through the barrier. The overlap of the macroscopic wave functions, as illustrated here, enables the tunneling of the Cooper pair. [7] . . .	22
2.3	Simplified illustrations of popular superconducting circuits in various $E_J/E_C$ ratio regimes, each functioning as qubits. [8] . . . . .	23
2.4	The qubit Hamiltonian’s eigen energies ( $E_m$ ), depicting the initial three levels, exhibit variation based on the effective offset charge ( $n_g$ ) for varying $E_J/E_C$ ratios. These energies are normalized with respect to the transition energy of the first two states ( $E_{01}$ ) at the $n_g = 1/2$ degeneracy point, with the energy baseline set at the bottom of the $m = 0$ level. Notably, vertical dashed lines in (a) highlight the charge ideal zone of operation at half-integer $n_g$ . [9] . . .	24

2.5	A microscopic image of a Transmon qubit device revealing its structure. Transmon comprises a Josephson junction shunted by two large capacitor islands. The corresponding circuit diagram illustrates the Transmon qubit coupled to the readout resonator through a coupling capacitor. Image from [10] . . . . .	25
2.6	Various superconducting qubit devices plotted based on their $E_J/E_C$ ratio. Image taken from [11] . . . . .	26
2.7	Illustrates a lumped element model of a superconducting resonator in (a). The same resonator is then depicted coupled to a transmission line and the immediate environment, referred to as a bath. This environment is typically the source of undesired noisy signals during the control and readout of qubits and poses an active challenge for the dephasing of superconducting qubits. Image from [12] . . . . .	27
2.8	Lumped element representation of a resonator coupled to a Transmon qubit and the energy level diagram of the corresponding subsystems. Image taken from [12] . . . . .	28
3.1	Displays the Graphical User Interface (GUI) provided by Qiskit Metal. This interface allows users to adjust design parameters and observe layout changes before finalizing the design. The GUI can be utilized either in conjunction with Python or as a standalone interface. . . . .	33

3.2	<p>Illustration provides an overview of the methodology employed by the Lumped Oscillator Model. (a) This illustration showcases a section of the layout from a larger quantum processor. The highlighted section considers a transmon qubit with two large capacitive plates and four co-planar waveguides used for readout, bus coupling resonators, and a charge line. The partition illustrates the classification into subsystems and the corresponding Hamiltonian for each subsystem that LOM intends to evaluate. (b) Further subdivision of the subsystems into simulation cells is illustrated. (c) The partial schematic defines the subsystem network to effectively evaluate the pairwise interaction Hamiltonian in the presence of all the subsystems in the network. (d) The illustration depicts the reduced, dressed subsystems, serving as essential building blocks, along with their dressed interactions. Image source [13] . . . . .</p>	34
3.3	<p>Illustration provides a conceptual overview of the method with an example quantum device. (b), Results from a finite-element eigenmode analysis (FEe) of the Josephson circuit linearized about its equilibrium are presented, showcasing the eigenfrequency and electric/magnetic fields. Notably, additional FE-driven simulations (FEd) are unnecessary, and the impedance matrix is not calculated. In (c), the Hamiltonian <math>\hat{H}_{\text{full}}</math>, encompassing nonlinear interactions to arbitrary order, is computed directly from eigenanalysis via Energy Participation Ratios. Dissipative contributions are also calculated from loss EPRs, which is unique to the EPR method. The iterative modification of the classical model's geometry allows for the extraction of desired dissipative and Hamiltonian parameters. Image source [14] . . . . .</p>	36

3.4	Schematic of the experimental setup for qubit characterization within the Bluefors dilution fridge. The outer box represents the dilution fridge, with each inner dashed line depicting a cooling stage. The devices operate in the bottom most stage, maintaining temperatures $15mK$ . The blue lines in the schematic denote the microwave lines responsible for conveying input signals to the device and transmitting output signals to and from the room-temperature electronics. . . . .	40
3.5	JPA TM-2035 by Raytheon (top) circuit schematic (below) was installed and characterized.[15] . . . . .	41
3.6	Schematic of a superconducting quantum interference device (SQUID). [16] .	42
3.7	Schematic of the experimental setup for characterizing the qubit. The input signals were sent from a vector network analyzer (VNA) at room temperature, and in the input line was attuned by -60dB (not shown in the figure). A cavity with a qubit was placed in the circuit, and the effects of the same are pronounced in the results obtained during characterization. . . . .	43
3.8	Phase of $S_{21}$ , with a specific bias current, as the frequency is swept across the vicinity of the cavity frequency. . . . .	44
3.9	Phase of $S_{21}$ for the JPA, covering a complete sweep of bias current and frequency across the vicinity of the cavity frequency. Sweeps from left to right zoom in on a smaller range of bias current to find an optimal current of operation. . . . .	44
3.10	Presents the magnitude of $S_{21}$ measurements, with a sweep of bias current and pump frequency. The JPA input signal power was set at -70 dB for all the experiments, and subsequent experiments were also performed by sweeping the JPA pump power, as illustrated in each section while keeping the other sweeping ranges the same. . . . .	45

3.11	Illustrates the performance of the JPA with and without RF pump. Panels a. and b. show the JPA’s performance when no pump is applied, indicating no amplification. Panel A sweeps the input power against the input frequency in the vicinity of $\omega_{signal}$ . Panel B reports the magnitude and phase of the output signal for different input signal powers. Note that the signal power is close to the cavity frequency. Panels c. and d. depict the performance of the JPA with the RF pump, showing an amplification of 10 dB in this case. The experimental setup and conditions for both trials were kept the same. . . . .	46
4.1	Transmon qubit coupled to a 3D cavity. Illustration of a Transmon placed in a 3D cavity (left), Picture of fabricated cavity and zoomed-in image of Transmon placed inside the cavity. Figure from ref [17] . . . . .	47
4.2	Circuit and device layout proposed in [18] . . . . .	49
4.3	Depicts the layout for Device 1, featuring a Transmon qubit with SQUID junctions for flux tunability. The design incorporates charge and flux lines for qubit control. The readout resonator is a $\lambda/2$ waveguide open to the ground on both ends, coupled using finger capacitors $C_{in}$ ( $C_{out}$ ) on the input (output) side for effective input-output coupling control. Filter stubs 1 and 2 serve as the notch filter, implemented as $\lambda/4$ coplanar waveguides. All input-output lines are impedance-matched to $50 \Omega$ . . . . .	50
4.4	The first three eigenmodes for the device are presented here: Mode 1 at 4.29 GHz, Mode 2 at 4.56 GHz, and Mode 3 at 7.43 GHz. . . . .	51
4.5	Shows the transmission through the readout resonator with the filters incorporated in the design. . . . .	51
4.6	Illustrates (a) the device layout and lumped element model and (b) the frequency response of the 4-qubit device designed for high-speed measurements, as presented in [19]. . . . .	52

4.7	The device layout features an X-Mon with a tunable SQUID junction, along with labeled charge and flux lines for qubit control. The coupling resonator utilizes a claw coupler, as indicated in the label, and is capacitively coupled to the filter/readout resonator. The charge and flux lines, along with the readout resonator are impedance-matched to $50 \Omega$ . . . . .	53
4.8	The first three eigenmodes for the X-mon qubit and peripheral circuit elements are presented here: Mode 1 at 5.46 GHz, Mode 2 at 6.81 GHz, and Mode 3 at 7.04 GHz. . . . .	54
4.9	Simulation results of transmission parameters through readout resonator of the device. . . . .	54
5.1	Trimon and its operation as described in [20]. (a) Illustrates the circuit model of a Trimon, while (b) shows the Josephson ring modulator structure at the center of the Trimon with four Josephson junctions. Inset: a complete Trimon device. (c) The device is placed in a cavity, and qubit (mode) A of the Trimon couples to the cavity. Qubits (modes) B and C are not coupled to the cavity, providing Purcell Protection. States of qubits B and C are measured using the dispersive shift of A, dependent on the states of B and C. (d) The energy level diagram illustrates the coupled two-qubit subspace involving qubits A and B, while qubit C remains in its ground state. The $\sigma_z\sigma_z$ coupling results in the transition frequency of each qubit being dependent on the state of the other, enabling the readout of qubits B and C while A couples to the cavity. Image from ref [20] . . . . .	57
5.2	Layout of a Trimon device, highlighting the pads and the associated contributions towards the capacitances in the schematic illustrated in Figure 5.1 . . . . .	59

5.3	Trimon device with 2 resonators coupling to mode A of the device. The frequencies for each qubit mode ( $\omega_q$ ) are identified as $\omega_A : 5.625$ GHz; $\omega_B : 7.072$ GHz, and $\omega_C : 7.971$ GHz. The corresponding anharmonicities extracted from EPR are $\alpha_A = 48.3$ MHz; $\alpha_B = 78.7$ MHz, and $\alpha_C = 99.7$ MHz. Modes 4 ( $\omega_{r1} = 8.897$ GHz) and 5 ( $\omega_{r2} = 8.899$ GHz) were expected at the same frequency, attributed to resonator frequencies, and are hypothesized to be separated due to numerical errors. Here, qubit B can be observed to couple to the resonators, which is undesirable and creates a decoherence channel for Qubit B, in contrast to the 3D Trimons. . . . .	60
5.4	Trimon with improved coupling of resonators. The frequencies for each qubit are extracted as $\omega_A : 5.557$ GHz; $\omega_B : 7.100$ GHz, and $\omega_C : 7.984$ GHz. The corresponding anharmonicities are $\alpha_A = 46.8$ MHz; $\alpha_B = 79.3$ MHz, and $\alpha_C = 98.9$ MHz. Modes 4 ( $\omega_{r1} = 8.884$ GHz) and 5 ( $\omega_{r2} = 8.846$ GHz) were expected as the resonator frequencies. Inset: Coupling the resonator to capacitor pads on either side to improve coupling to mode A. . . . .	61
6.1	Illustration of various packaging methods for superconducting qubit processors presented in published literature. Images (a) from ref [21] and (b) from ref [22] © (2021 IEEE, Reprinted, with permission), respectively, showcase examples of chips directly mounted on a PCB and wirebonded to associated tracks for interfacing with control electronics, with a metal shield protecting the superconducting chips from external electric and magnetic fields during operation. Careful design of the PCB for RF and cryogenic applications is essential, and it is easier to implement, as all the techniques used are easily accessible to users, even in an academic setup. Images (c) ref [23] and (d) [24] © (2018 IEEE, Reprinted, with permission) present a proposal for flip-chip bonding of an integrated superconducting processor, along with fabricated results of flip-chip bonding performed on superconducting qubit devices. . . .	64

6.2	The figure presents the comprehensive stack-ups, featuring copper layers (depicted in gold) for signal layers and ground planes, along with Rogers/Megatron 6 (in green) as the core dielectric and prepreg layers (in light-green). Rogers was selected for its favorable properties: $\epsilon_r$ (dielectric constant) of 3.48, dissipation factor of 0.0037, and a Z-axis coefficient of thermal expansion of 32 ppm/°C. On the other hand, Megatron 6 offers $\epsilon_r$ of 3.4, a dissipation factor of 0.004, and a Z-axis coefficient of thermal expansion of 45 ppm/°C. Both stack-ups are well-suited for cryogenic applications. . . . .	66
6.3	Eigenmode simulations using SIwave for the PCB stack-ups revealed certain PCB-based eigenmodes within the operational frequency range. To mitigate any potential impact on the qubits, strategic positioning of shielding vias was implemented, aiming to avoid modes near the chip that could potentially introduce a package-based dephasing channel for the qubits. . . . .	66
6.4	Microwave packaging including PCB and a test chip. The bottom enclosure accommodates the PCB and is directly attached to the mounting plate of the dilution refrigerator. Constructed from copper, the bottom enclosure is chosen owing to the thermal conductivity and lower dielectric losses. The top enclosure serves the purpose of shielding the chip from external radiation. It contains an outer shield made of copper, while it incorporates a 1 mm thick layer of aluminum to protect the chip from stray magnetic fields in the surrounding environment. Non-magnetic SMA contact connectors are used to interface with SMA cables within the dilution refrigerator. . . . .	67
6.5	Eigenmode simulations on ANSYS HFSS report the box modes to start from 25.11 GHz. The calculations are in agreement with the expression 6.1 . . . . .	68
6.6	Assembled microwave package. Inset: Wirebonded test chip. . . . .	69
6.7	Transmission and crosstalk performance characterization of the microwave package was conducted in the frequency range of 1 GHz to 10 GHz. All these experiments were performed at room temperature. . . . .	70

6.8	Measurements using the Megatron6 PCB exhibited unwanted frequency modes, as indicated in repeated experiments. . . . .	71
6.9	PCB layout (all layers), designed to package 8 qubit devices. This specific PCB configuration supports 16 RF channels and includes 1 DC channel designed to function as a flux line for tunable qubits. In the layout, the green and orange tracks represent RF channels on different layers, while the blue track indicates the DC flux line. . . . .	72
6.10	Analysis of near-end crosstalk performed using SIwave. It indicates that cross-layer crosstalk is negligible. However, higher crosstalk is observed in the charge lines that are closely packed on the right side of the chip footprint. . . . .	73
6.11	Box modes were evaluated using ANSYS HFSS and were observed to start at 12.07 GHz . . . . .	73
A.1	Layout of the test chips. Test chips TC1 to TC4 feature distinct layouts of coplanar waveguides. . . . .	76
A.2	Bonding pad with finger capacitor. Inset: Zoomed-in image of the finger capacitor with critical dimensions (units $\mu\text{m}$ ). . . . .	78
A.3	Fabrication result and challenges. a-d. present successful outcomes for chips TC1-TC4, respectively. e-h. highlight various challenges. e. depicts the result of overexposure of the pattern. f. and g. display cases where the finger capacitor, as presented in Figure A.2, did not form when hard contact was used on the contact aligner instead of vacuum contact. h. represents a case where the properly exposed and developed finger capacitor region was damaged during an improper liftoff process. i. and j. exhibit instances where the results show proper formation of the finger capacitors using the reported recipe. . . . .	79

## LIST OF TABLES

1.1	Comparison of superconducting qubits, spin qubits, and trapped ion qubits based on basic metrics to benchmark the performance of any quantum computing system. <b>Note:</b> <i>The performances noted below attempt to consolidate some of the best performances of each platform reported. These are reported from different devices and experiments, which might not provide an all-around comparison of each system. This table intends to convey the progress each of these qubit platforms has made over the years.</i> . . . . .	11
4.1	Device parameters for Transmon with Notch Filter extracted using EPR method.	51
4.2	Device variations in final tapeout to experimentally verify the effects of variation in input-output coupling and incorporation of flux line in the device. . . . .	52
4.3	Device parameters for X-mon with BandPass Filter extracted using EPR analysis. . . . .	54
4.4	Design variations for the X-mon based qubit devices included in the final tapeout. . . . .	55

## ACKNOWLEDGMENTS

I extend my sincere gratitude to Prof. Chee Wei Wong for introducing me to the field of superconducting qubits and providing the opportunity and resources to conduct research with his group for my master's thesis.

I am also grateful and honored to have Prof. Kang L. Wang and Prof. Sudhakar Pamarti, and appreciate their time and commitment towards their pivotal roles in my thesis committee.

My journey as a master's student in the Mesoscopic Optics and Quantum Electronics Laboratory was enriched by the constant guidance and support of Murat Can Sarihan, Cody Fan, Madeline Taylor, Kerry Yu, and Jin Ho Kang. Special acknowledgment is also due to Talha Yerebakan for his assistance in navigating the intricacies of cleanroom processes.

I am also grateful for the fruitful discussions on microwave packaging for superconducting qubits with Dr. Yaniv Rosen, Stijn de Graaf and Benyamin Fallahi Motlagh. I would also like to thank Nick Millkey for his help with wirebonding the test chips for the microwave package.

I would also like to extend my thanks to Prof. Jason Petta for proofreading the thesis and providing guidance on its overall structure.

I express my gratitude to the publishers for granting copyright permission for certain images in this thesis.

A heartfelt thank you to Anuj Agrawal, Harshita Khandelwal, and Namarta Sarraf for their support during critical junctures of graduate school. I am also thankful to all my peers and colleagues at UCLA for contributing to the memorable experiences of my graduate school journey.

Lastly, my deepest appreciation goes to my parents back in India for their unwavering support throughout my master's program.

# CHAPTER 1

## Introduction

Quantum computing has emerged as a captivating and promising 21st-century technology nearly a century following the formulation of quantum mechanics in the early 1900s. If harnessed to its full potential, this technology possesses the capacity to revolutionize the methodologies of information processing and problem-solving. Unlike classical computers, which utilize bits as their fundamental units operating on binary logic (0 and 1), quantum computers employ qubits – the quantum analog of bits – which leverage the intrinsic principles of superposition and entanglement of states. Through these quantum properties, qubits enable the execution of specific computations at unparalleled speeds, offering the prospect of solving currently intractable problems within feasible timeframes.

In recent years, significant strides have been achieved in comprehending and engineering physically viable quantum computers. However, despite their immense promise, quantum computing is beset by inherent errors stemming from the principles of quantum mechanics. These challenges include qubit-environment coupling, which must be managed to avoid state decoherence, along with the complexities of control, characterization, and the crucial aspect of scalability within existing quantum computers. Both academia and industry have dedicated efforts to confront these obstacles, each devising novel architectures and techniques to overcome them. This thesis addresses the engineering hurdles tied to scalability, particularly within the context of Noisy Intermediate Scale Quantum (NISQ) Computers. It delves into diverse planar superconducting qubit architectures, exploring meticulous microwave engineering, precise control mechanisms, scalable packaging, and other innovative designs that could potentially enhance the scalability of the quantum computers employing superconducting qubits.

## 1.1 What is Quantum Computing

Quantum computers are machines that aim to exploit the complexity of many-particle wavefunctions to solve computational problems with a time advantage over any available classical computer.

The beginning of the field of quantum computing is a debatable discussion, with significant progress in physics, engineering, and computer science over the years leading to the unified domain of quantum computing and quantum information. Richard Feynman is often credited with proposing the concept of using hardware-based quantum mechanical phenomena to simulate physical phenomena in his 1981 paper, 'Simulating Physics with Computers' [25]. Additionally, Paul Benioff's work on representing a quantum mechanical Hamiltonian model of a computer as Turing machines [26] has contributed to the foundation of quantum computing.

In the following years, quantum key distribution emerged as an instrumental concept for enhancing information security [27], laying the groundwork for future progress and the development of quantum algorithms. Notable examples include the Deutch-Jozsa algorithm in 1992 [28], Bernstein-Varizani algorithm for solving a hidden shift problem in 1993 [29], Simon's algorithm in 1994 [30], and the prominent Shor's algorithm [31] for prime factorization by Peter Shor. Shor's algorithm, in particular raised interest in the industry and academic groups to work towards building practical and scalable quantum computers.

In the early 2000's David DiVincenzo from IBM, focusing on the practical implementation of a physical quantum computer and information processing, introduced criteria now known as DiVincenzo's criteria for selecting a physical platform for quantum computing applications [32]:

1. A scalable physical system with well-characterized qubits or states defining the basis states for quantum computing applications.
2. The ability to initialize qubits to a simple fiducial state, for example,  $|000\dots 0\rangle$ .

3. The quantum system must remain coherent during the entire cycle of quantum operations, including the initialization, application of quantum gates, and measurement.
4. The system must be capable of supporting a universal set of quantum gates.
5. The ability to read or measure the quantum register at the end of all quantum operations.

In the past couple of decades, numerous groups in academia and industry have used DiVincenzo’s criteria as a baseline to explore different platforms for implementing a scalable quantum computer, making varying levels of progress.

While the theoretical aspects of a scaled-up quantum computer are better understood today than a couple of decades ago, current systems are still plagued by the decoherence of states, depending on the platforms defining the qubits. Though no practical system is free of decoherence, some level of it can be countered using various error correction techniques, albeit at the cost of using a higher number of qubits, a milestone not yet reached by state-of-the-art quantum computers. Presently, processors with less than 1000 qubits are referred to as noisy intermediate-scale quantum (NISQ) [33], a term coined by John Preskill in 2018 [34]. These systems are not advanced enough to be fault-tolerant or to apply any quantum error correction techniques [35]. The scale of these systems is defined by a parameter called quantum volume, based on the number of qubits in a system and their associated gate fidelity.

It is essential to note that quantum computers are not an advanced version of classical computers in scale, speed, or otherwise. They are an altogether different kind of physical platform with the capability to solve various tractable computational problems with a significant advantage in terms of computational times and problem scale.

The following subsections discuss the advantages of a quantum computer over any classical computer, the current and popular physical platforms and architectures, as well as their performance and challenges.

The following subsections discuss the advantages of a quantum computer over any

classical computer, the current and popular physical platforms and architectures, as well as their performance and challenges.

### 1.1.1 Advantage

To comprehend the advantage of quantum computing over state-of-the-art classical computing, it is essential to start with the difference in their basis states. Classical computers use bits (0 and 1) and binary logic, while quantum computers encode qubits in the basis states of  $|0\rangle$  and  $|1\rangle$ , represented as two-dimensional vectors in Hilbert space. Figure 1.1 visually represents a quantum-bit; qubit, and the corresponding wavefunction ( $|\Psi\rangle$ ) on a Bloch sphere, showcasing their unique characteristics.

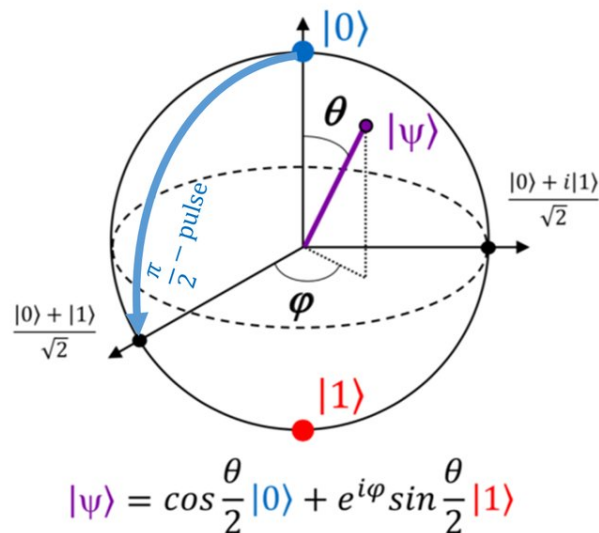


Figure 1.1: Representing a qubit on a Bloch sphere. The conventional north pole of the Bloch sphere is assigned to the state  $|0\rangle$ , and correspondingly, the south pole to  $|1\rangle$ . The vector denotes the current state of the qubit, and any operation on the qubit moves the vector along the Bloch sphere. A common operation is to apply a  $\pi$ -pulse, as illustrated in the figure. [1]

While any qubit can exist in its basis states or a complex sum of them, the quantum phenomena of superposition and entanglement play a crucial role. Superposition allows a qubit to be a complex sum of  $|0\rangle$  and  $|1\rangle$ , while entanglement involves qubits acting as an inseparable group. Although different platforms exploit these phenomena uniquely, the fundamental physics of a qubit remains consistent across diverse quantum computing

systems.

The computational differences between classical and quantum computing paradigms aim to speed up computational times. As efforts to scale up reliable quantum computers progress, parallel research identifies specific problem types where quantum computers excel, including combinatorial optimization, complex linear algebra, differential equations, and factorization. Industries, from physical and biomedical technology to financial institutions, anticipate employing quantum technology for industry-specific use cases [36, 37].

Quantum computers have shown promise in molecular simulations for material synthesis [38], enhancing machine learning algorithms [39, 40], structural search [41], and improving Monte Carlo simulations for risk analysis [42] and portfolio optimizations in financial institutions [43, 44]. The evolving understanding of quantum computing’s potential benefits and targeted improvements for specific users and use cases have driven tremendous growth in the field over the past decade.

However, it’s crucial to note that the current state of quantum computers remains in the NISQ regime. The immediate challenge is identifying the physical and engineering complications affecting the scalability of platforms to an error-corrected regime.

### 1.1.2 Current Architectures

The physical implementation of qubits, as discussed above, is varied and has an ever-evolving history. Any physical platform for quantum computing is not a standalone system but requires associated measurement and control equipment, along with an associated classical computer to integrate all the pieces of instruments into one. Figure 1.2 illustrates a simplified version of the stack-up for a quantum computing hardware setup and the associated technologies necessary to operate the system.

The choice of a physical platform depends on various factors, including physical scale, manufacturability of the physical qubits, control protocols and setup ease, access to the qubits, and susceptibility to decoherence in the immediate environment. In most cases, an associated cryogenic system is used to shield the physical platforms from the environment

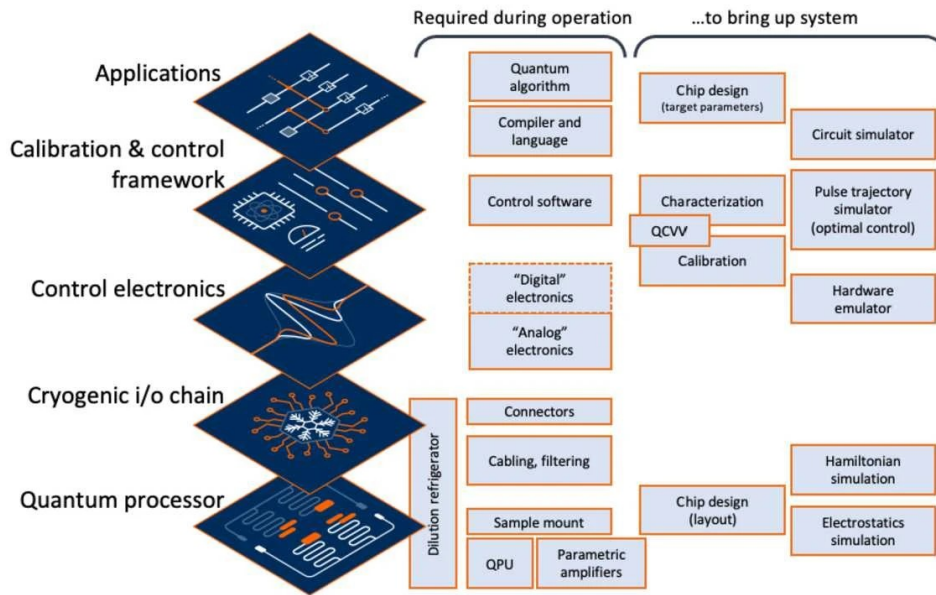


Figure 1.2: Simplified stack for a superconducting qubit setup. Operating any quantum computing platform requires synchronization between numerous sophisticated control and measurement tools interacting with the physical qubit. Typically, the qubit is placed inside a dilution refrigerator to keep the devices isolated and at cryogenic temperatures. Image adapted from [2]

and eliminate potential sources of noise. While none of these efforts provide a perfect qubit, ongoing attempts are made every day to get one step closer at a time to building an error-free qubit platform. The following subsections provide an overview of the most popular quantum computing platforms that have emerged in recent years, both in industry and academia.

### 1.1.2.1 Superconducting Qubits

Superconducting qubits have gained popularity in the recent quantum computing race. These solid-state devices utilize the energy levels of an anharmonic LC oscillator, introducing anharmonicity through a Josephson junction (Figure 1.3). Controlled and measured using microwave signals, these qubits offer advantages in terms of design flexibility, scalability using existing semiconductor manufacturing techniques, and ease of coupling and readout due to their circuit nature.

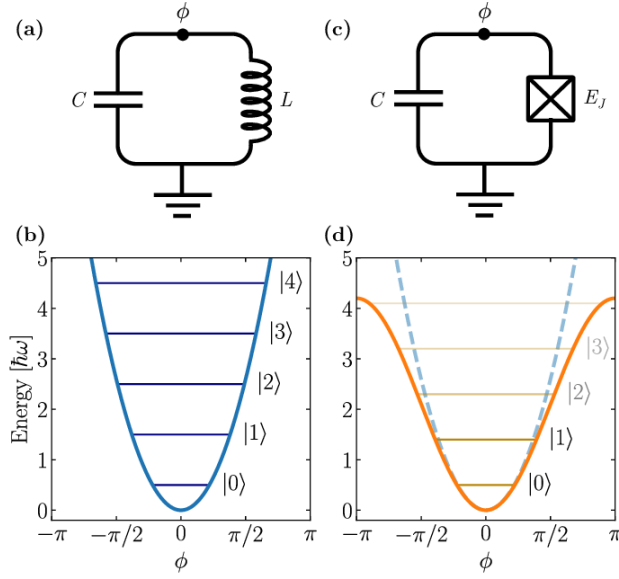


Figure 1.3: Illustration of a fundamental difference in the energy level spacing in a quantum harmonic oscillator (QHO) formed by an LC circuit and the anharmonic oscillator by introducing a Josephson junction. (a) denotes an LC oscillator with inductance  $L$  and capacitance  $C$ . The phase on the superconducting island is denoted by  $\phi$ , and the ground node is referenced to have a zero phase. (b) Energy levels of the LC oscillator (a). The energy levels in a QHO are equally spaced by  $\hbar\omega$ , where  $\omega = \sqrt{\frac{1}{LC}}$ . (c) represents a lumped element model of a superconducting qubit where the linear inductor is replaced by a Josephson junction of energy  $E_J$ . (d) Illustrates the change in the harmonic potential with respect to a QHO (blue); this introduction of anharmonicity yields non-equal energy spacing necessary to operate a 2-level system.[3]

While superconducting qubits seem favorable for large-scale quantum computers, challenges remain, including tunability, device scale, and the inherent possibility of transitions from a  $|1\rangle$  to  $|2\rangle$  state. Some groups have explored these transitions for high-dimensional quantum devices [45], but careful control is required to avoid them in qubit devices. Additionally, the use of dilution refrigerators to achieve milli-Kelvin temperatures raises scalability concerns in discussions of large-scale and error-corrected quantum computing systems.

### 1.1.2.2 Spin Qubits

Spin qubits, as the name suggests, utilize the spin degree of freedom of electrons (or electrons) to define qubits. They are generally formed by creating a quantum dot using

sophisticated gate structures in Silicon and other platforms, and their initialization and control involve energy-dependent tunneling of electrons.[46]

Semiconductors have emerged as the most popular candidates to host spin qubits due to the accessible methods to chemical and isotopic enrichment of Silicon and the ability to leverage state-of-the-art semiconductor manufacturing techniques to fabricate these complex devices. In terms of scaling, spin qubits are promising candidates, as they are significantly smaller in size compared to their superconducting counterparts.

Spin qubits come in multiple flavors depending on how a qubit is defined (Figure 1.4), illustrating some popular architectures adopted over the years to define different types of spin qubits.

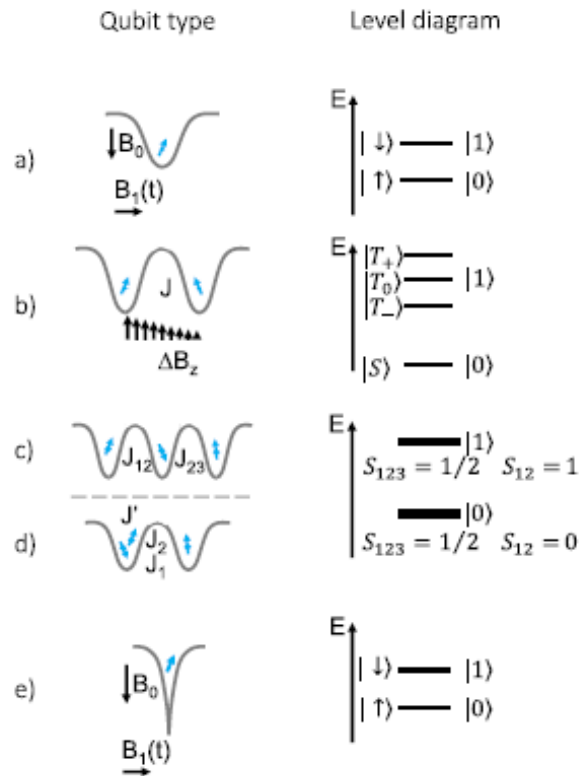


Figure 1.4: Illustration of popular spin qubit configuration profiles and the corresponding energy levels and definition of each qubit state. (a) Loss-DiVincenzo qubit. (b) Singlet-triplet qubit. (c) Exchange-Only qubit. (d) Hybrid qubit with the same computational basis states. (e) Donor-bounded  $e^-$  qubit. Image adapted from [4]

Spin qubits have gained popularity in academic and industrial groups due to the

evident upsides of the platform. Companies like Intel and HRL heavily invest in studying and working towards scaling this architecture for a fault-tolerant quantum computer. Although high fidelities have been achieved for initialization and single and two-qubit gates on spin qubit platforms, there are still evident challenges associated with the complex engineering issues of addressing each qubit and achieving sufficient connectivity.

### 1.1.2.3 Trapped Ion Qubits

The idea of utilizing a multi-level system for quantum information is quite intuitive, and a formal proposal addressing the physics and engineering aspects was made as early as 1995 [47]. Current quantum computing systems defining qubits use the different hyperfine energy levels of trapped ions. Figure 1.5 illustrates a simplified protocol for the state-preparation, control, and readout of trapped ion qubits.

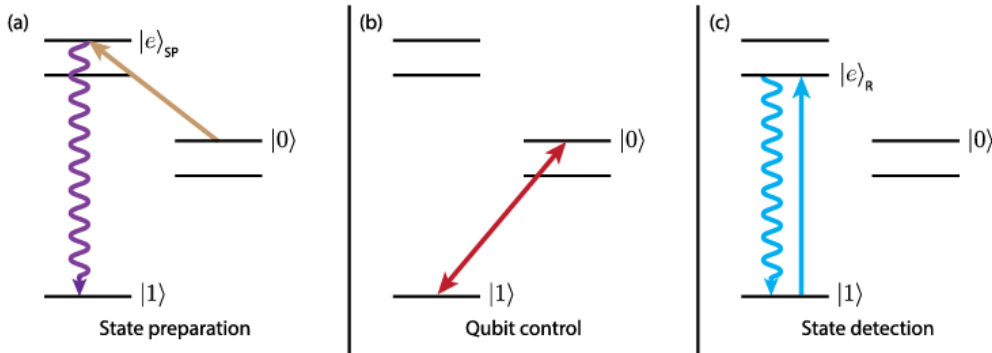


Figure 1.5: Illustrates a trapped ion qubit’s state preparation, control, and readout. (a) State preparation involves optically pumping the ion to an ancillary state ( $|e\rangle_{SP}$ ) from the stable and long-lived state ( $|0\rangle$ ), which rapidly decays to the state ( $|1\rangle$ ). (b) The control of the qubit is achieved by coupling the states ( $|0\rangle$ ) and ( $|1\rangle$ ) using electric quadrupole transitions. (c) Readout of the state is achieved by shining light at the transition frequency of ( $|1\rangle$ ) – ( $|e\rangle_R$ ) and observing the photons emitted from the transition decay (if any). [5]

Ions are commonly trapped using Paul or Penning traps and held in position using laser cooling techniques. Recent efforts have seen the use of microfabricated surface ion traps [48], moving away from traditionally used linear traps to scale the systems better.

Trapped ion qubits have performed remarkably well, with reported single qubit gate fidelities of 99.9999% [49] and two-qubit gate fidelities of 99.9% [50]. While the idea of

using trapped ions and their hyperfine energy levels as qubits is lucrative, challenges arise in scaling up the platform for a higher number of qubits, especially considering the vulnerability of planar traps to stray photons and decoherence during RF loss at dielectric interfaces [51].

#### 1.1.2.4 Topological Systems as Qubits

Employing topological systems has emerged as an alternate platform to realize a qubit. The theoretical proposal was put forth by Alexei Kitaev in 1997 [52] and utilized quasiparticles named Anyons, whose world lines pass through one another to form braids in three-dimensional spacetime. The proposal used these braids to form logic gates, identified to be much more stable than trapping particles for quantum computation.

Anyons are classified neither as Bosons nor Fermions and hence cannot occupy the same energy state. Hence, the defined world-lines cannot interact and tend to form stable braids in spacetime. Excitations in a two-dimensional electron gas in the presence of a strong magnetic field have been observed to form Anyons, a phenomenon known as the Fractional Quantum Hall effect [53], where experimental work indicates that these systems are worth exploring.

While the use of these systems for quantum computation are mostly theoretical, some numerous experimental efforts are pushing to create a qubit system capable of quantum computation. Companies like Microsoft [54] are invested in exploring topological systems for developing a scalable quantum computing platform.

#### 1.1.3 Performance

Different platforms aiming at scalable quantum computing have grown significantly over the past two decades. Table 1.1 below compares the platforms discussed in the preceding sub-sections and their performance to date using commonly utilized parameters to benchmark progress against one another.

Although these platforms are still not in an error-free regime, and most of these devices

Table 1.1: Comparison of superconducting qubits, spin qubits, and trapped ion qubits based on basic metrics to benchmark the performance of any quantum computing system. **Note:** The performances noted below attempt to consolidate some of the best performances of each platform reported. These are reported from different devices and experiments, which might not provide an all-around comparison of each system. This table intends to convey the progress each of these qubit platforms has made over the years.

	Qubits Achieved	Coherence Times	Initialization Fidelity	Readout Fidelity	1-Qubit Gate Fidelity	2-Qubit Gate Fidelity	Gate Time	Connectivity
<b>Superconducting Qubits</b>	433 [55]	1.48 ms [56]	99% [57]	99.5% [58]	99.9% [56]	99.88% [59]	30 ns [60]	Nearest Neighbor
<b>Spin Qubits</b>	12 [61]	120 $\mu$ s [62]	99% [63]	99.975% [64]	99.957% [65]	99.8% [66]	10 ns [67]	Nearest Neighbor
<b>Trapped Ion Qubits</b>	32 [68]	5500 s [69]	99.991% [70]	99.99% [71]	99.995% [72]	99.9% [73]	5 $\mu$ s [72]	All-to-All

have been optimized to perform the best in at least one aspect, this exhibits significant progress. Understanding these systems has improved with the evolution of the associated technologies involved. However, none of these are exempt from challenges native to every platform. The following subsection discusses the overall challenges plaguing the popular quantum computing platforms.

#### 1.1.4 Challenges

As the field of quantum computing is maturing at a staggering pace and is already entering the NISQ regime, it is essential to take note of the impending challenges that affect the performance of the current systems. The inherent nature of a qubit to decay or decohere, losing all the properties of its state to the immediate environment, has always been a source of concern.

As the systems are getting more densely packed in an attempt to scale up, the problems become more prominent and challenging to deal with. Various protocols are in place to counter the effects of decoherence in the respective qubit platforms. However, more is needed to take these limitedly scaled platforms to an error-free regime. Also, although the initialization, readout, and gate fidelities look significantly better now than even half a decade back, these performance metrics differ from the available classical computing systems.

Building full-scale quantum computers poses the same central challenges: maintaining the simultaneous abilities to control quantum systems, measure them, and preserve their strong isolation from uncontrolled parts of their environment. As discussions on quantum supremacy intensify, the challenge of achieving comparable benchmarked performance of quantum processors remains ongoing for physicists and engineers.

## 1.2 Scalability of Quantum Computers

The state-of-the-art quantum computers today can handle small-scale chemistry simulations or exhibit advantages over classical computing on a limited scale. However, to achieve practical-sized quantum computations, these systems need to scale. Moving from NISQ to an error-corrected regime demands a significantly higher number of qubits on the platform to implement any practical error-correction protocols. It is essential to understand, in the context of scaling a quantum computer, that the physical size of qubits is not the only point of consideration. The full stack of the computer effectively needs to scale with the increased number of qubits, which also must be subsequently scaled up.

The following subsections detail the needs, progress, and challenges associated with scaling the available quantum computing systems.

### 1.2.1 Need for Scalability

Understanding the need for scaling any platform, in this case, quantum computers, starts with grasping the current performance of the system, its basic requirements, and the benefits a scaled-up system provides over the existing classical computing technology already available. The NISQ regime of quantum computers has served as a reasonably good platform to address skeptics of quantum computing who doubted overcoming the challenges of building and controlling such devices to surpass the power of any classical Turing machine.

The inherent concern of state decoherence and effectively benchmarking the perfor-

mance of these systems against available classical computers has been a challenge. This is where the NISQ regime has proven its purpose well. Noise, in the context of NISQ, implies that these systems are still prone to errors and decoherence, and their computational capabilities have been limited and intermediate points out to the fact that they must not be directly compared to the brute force capabilities of classical computers but are still large enough to be error-corrected in small scale and run existing quantum algorithms in a limited scale. Running many-body quantum simulations might not be possible with the current state of quantum computers. The already available quantum computers have exhibited a notable advantage using quantum algorithms. There have been limited scale demonstrations of the algorithms as mentioned earlier, like Shor’s algorithm, Grover’s algorithm, or Deutsch–Jozsa’s algorithm on early noisy quantum computers [74, 75, 76], but at this stage, it won’t provide any significant advantage in the case of quantum computers by scaling these algorithms, given the current error rates in these systems which would be enough to ruin any precision of the results.

NISQ has always been termed as a step towards full-scale fault-tolerant quantum computing by providing us with a deeper understanding of the physics and engineering challenges of the technology while also developing tools along the way necessary to scale these systems better for the future. [77]

Considering that we need a higher number of qubits to perform meaningful full multi-body quantum simulations using these machines, it has been noted in the literature that we would likely need at least a million physical qubits to have a fully error-corrected quantum computer.[78]

Given the current state of these systems, much progress has been made in the last couple of decades to scale these quantum systems in a meaningful manner, and a discussion on it is detailed in the following subsection, with plans laid out by various prominent teams.

### 1.2.2 Progress with Scalability and Future Plans

Quantum computing systems have scaled up significantly in recent years, aiming to enhance accuracy, computational scale, control, and overall system integration. Industrial groups, notably IBM, have led in achieving the highest number of qubits, with the most recent being a 433-qubit superconducting quantum computer accessible via their cloud network, maintaining its status as the highest online quantum computer [36]. Atom Computing has announced a 1000-qubit processor, intending to make it available for users by 2024 [79]. Other industrial players, such as Google Quantum AI (superconducting), Rigetti Computing (superconducting), IonQ (trapped ion), Xanadu (photonic), and more, are actively working in the field, striving to make their quantum computers live for users and aiming for further scalability. All these systems are currently in the NISQ regime, and each team has a roadmap to scale them further to reach the error-corrected regime in the near future, with the understanding that an error-corrected system would require at least a million physical qubits. [80, 81]

As the race to scale physical qubit platforms strengthens, some teams also focus on scaling or optimizing the control equipment. Recognizing that control systems must efficiently scale up alongside qubit platforms, Intel has developed fully integrated cryo-CMOS SoC Horse Ridge 1 and Horse Ridge 2 using their 22nm technology node, operating at 4K for qubit control and readout [82]. While companies like Quantum Machines and Zurich Instruments, among others, are dedicated to scaling and optimizing control equipment as physical qubit platforms expand.

Despite active efforts, quantum computing systems still face significant challenges in scaling up. The following subsection details the active roadblocks limiting the scaling of current quantum computing platforms.

### 1.2.3 Roadblocks with Scalability

The advancements in understanding qubit platforms have also shed light on the engineering challenges associated with scaling up quantum computing platforms in recent years. The

diversity among qubit platforms introduces non-uniformity in developing technologies for controlling and measuring qubits. While one platform may excel in scaling, it may not perform optimally for others. Consequently, the scaling progress across platforms is quite non-uniform. Superconducting qubits have achieved a remarkable milestone of over 400 physical qubits, whereas spin and trapped ion qubits struggle to scale beyond 50 qubits on a chip.

This non-uniformity in scaling stems from various issues, including qubit coherence times, crosstalk and susceptibility to noise from the immediate environment. Another engineering challenge emerges in the initialization and gate operating times of each qubit. The full operation of the quantum circuit, involving the initialization, manipulation, and readout of qubits, must significantly outpace the decoherence times to mitigate any computation errors. Efficient synthesis of quantum circuits has to evolve, focusing on gate decomposition, time reduction, and optimizing initialization and readout times while managing SPAM errors within acceptable margins.

Another challenge in scaling quantum computing platforms is the organization of the qubit plane. Most physical qubits are connected to their nearest neighbors, posing difficulties in applying multi-qubit gates. The use of multiple swap gates to facilitate multi-qubit gates has proven error-prone, emphasizing the need for improved qubit connectivity.

Scaling platforms to a higher number of qubits and implementing effective error correction platforms are essential for reaching an error-free regime. Current quantum computing systems operate with error rates of  $10^{-2}$  to  $10^{-3}$  errors per gate operation, whereas classical CMOS technology maintains error rates of  $10^{-15}$  errors per operation [83]. The current quantum computing systems face significant challenges in reducing error rates.

Finally, the scalable fabrication of qubits poses engineering challenges that researchers and engineers are actively addressing. The need for operation of the devices in the milli-Kelvin range temperatures inside a dilution fridge and platforms with a lesser

propensity for states to decohere, minimal crosstalk, and ideal parsing of control signals is crucial. The physical size of qubits presents a balance between scalability, optimizing fabrication processes, and scaling down devices—a significant engineering challenge. While superconducting qubits have successfully scaled to over 433 qubits [55], scaling them to a million qubits poses challenges considering their physical sizes range from 300 to 500 micrometers [84]. Similarly, spin qubits have smaller device dimensions, but complex fabrication techniques and crosstalk effects from densely packed quantum dots pose scaling challenges. Intel’s work on cryo-CMOS technology [82] for scalable control units for qubit platforms addresses some of these challenges. However, imminent engineering challenges still remain in understanding the viability of ultra-low-power cryoelectronics to scale up qubit platforms.

Despite persistent challenges in scaling up quantum computers, numerous teams worldwide are tackling these issues one at a time, working towards the goal of a scaled-up quantum computer in the near future. The aim is to develop systems capable of performing real-world computations that these platforms are intended to tackle.

## CHAPTER 2

### Superconducting Qubits

Superconducting qubits have emerged as prime candidates for scalable quantum computing applications over the last decade, with significant efforts focused on understanding the finer nuances of this cross-disciplinary venture and scaling up the system as a whole. The work presented in this thesis involves efforts on scaling Transmon-based qubits in an academic setup. The subsections below are dedicated to discussing the physics of superconducting qubits, highlighting the importance and theory of Transmon qubits, and identifying the devices used in academic and industrial settings to investigate Transmon qubits further, eyeing better efficiency of the devices and eventual platform scale-up.

#### 2.1 Physics of Oscillators

The preceding section compared various qubit platforms. Before delving into the design of Transmon qubits, it is essential to discuss the underlying physics of engineering superconducting qubits.

Starting the discussion with time-dependent Schrödinger's equation that governs any quantum mechanical system with state  $|\Psi\rangle$  is essential in this context. Following the mathematical derivations from [6, 12].

$$\hat{H}|\psi(t)\rangle = i\hbar\frac{d}{dt}|\psi(t)\rangle \quad (2.1)$$

While a quantum mechanical system can be described by (2.1) and solving the first-order differential equation described by Schrödinger's equation above, the quantum

systems can further be described by a linear dimensional system with a formal solution described by:

$$|\psi(t)\rangle = e^{-i\omega t}|\psi(0)\rangle \quad (2.2)$$

The exponential term here enables the time-independent Hamiltonian to govern the system's time evolution. While a general description of a quantum mechanical system is provided above, a discussion on superconducting qubits is better initiated with the formal description of an LC oscillator, as shown in Figure 2.1. In this system, the energy of the system oscillates between the magnetic energy of an inductor and the capacitive (electric) energy stored in a capacitor. The instantaneous energy in each of the constituents of the circuit can be defined by,

$$E(t) = \int_{-\infty}^t V(t')I(t') dt' \quad (2.3)$$

here  $V(t')$  and  $I(t')$  denote the instantaneous voltage and current of the corresponding elements of the circuit.

Now, with the intention of deriving the classical Hamiltonian using the Lagrange-Hamilton formulation, the circuit elements are represented in terms of the generalized circuit coordinates of charge, or in this case, flux, as denoted below.

$$\Phi(t) = \int_{-\infty}^t V(t') dt' \quad (2.4)$$

At this point, utilizing 2.3 and 2.4 and using our preexisting knowledge of the relations  $V = L\frac{dI}{dt}$  and  $I = C\frac{dV}{dt}$ , the capacitive and inductive energy in terms of node flux can be represented as,

$$T_c = \frac{1}{2}C\dot{\Phi} \quad (2.5)$$

$$U_L = \frac{1}{2}L\Phi^2 \quad (2.6)$$

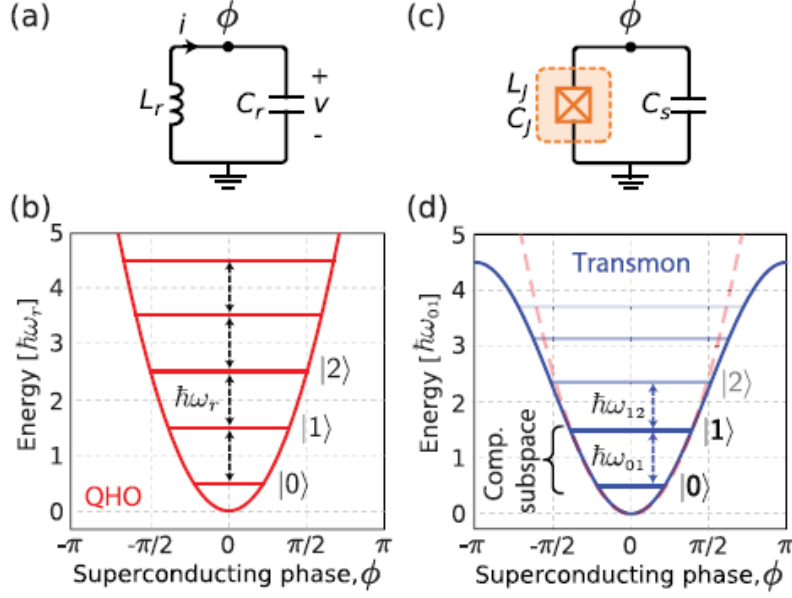


Figure 2.1: Extension of Figure 1.1. (a), (b) represents an LC quantum harmonic oscillator with phase on the island defined by  $\phi$  and the corresponding energy level diagram for the QHO with energy subsequent levels spaced by  $\hbar\omega_r$  respectively. (c) and (d) represent replacing the linear inductor in the QHO by a Josephson Junction to introduce the effects of a non-linear inductor and the subsequent anharmonic oscillator with the two-lowest energy levels forming the computational subspace with the unequal energy spacing  $\hbar\omega_{01}$  and  $\hbar\omega_{12}$ . [6]

As the Lagrangian is denoted as the difference in the kinetic and potential energy terms, drawing parallels to a classical harmonic oscillator, the Lagrangian here can be defined as:

$$L = T_c - U_L = \frac{1}{2}C\dot{\Phi} - \frac{1}{2}L\Phi^2 \quad (2.7)$$

Now, to derive the Hamiltonian, Legendre transformations are used further to calculate the conjugate to the flux; in this case, the charge on the capacitor,

$$Q = \frac{\partial L}{\partial \dot{\Phi}} = C\dot{\Phi} \quad (2.8)$$

Finally using 2.7 and 2.8 the Hamiltonian of the system can be defined as,

$$H = Q(\dot{\Phi})\dot{\Phi} - L = \frac{Q^2}{2C} + \frac{\Phi^2}{2L} = \frac{1}{2}CV^2 + \frac{1}{2}LI^2 \quad (2.9)$$

Drawing parallels to a mechanical oscillator, capacitance of the circuit can be equated to the mass of the object, and the resonant frequency here can be described by  $\omega = \frac{1}{\sqrt{LC}}$ .

The description of the system thus far has been in a classical regime. To effectively discuss the quantum-mechanical picture of the system, it is essential to define the corresponding charge and flux operators of the LC circuit, while the above classical coordinates satisfy the Poisson bracket criteria.

$$\{f, g\} = \frac{\delta f}{\delta \Phi} \frac{\delta g}{\delta Q} - \frac{\delta g}{\delta \Phi} \frac{\delta f}{\delta Q}$$

In this case,

$$\{\Phi, Q\} = \frac{\delta \Phi}{\delta \Phi} \frac{\delta Q}{\delta Q} - \frac{\delta Q}{\delta \Phi} \frac{\delta \Phi}{\delta Q} = 1 - 0 = 1 \quad (2.10)$$

The respective charge and flux operators also satisfy the commutation relation.

$$[\hat{\Phi}, \hat{Q}] = \hat{\Phi}\hat{Q} - \hat{Q}\hat{\Phi} = i\hbar \quad (2.11)$$

So, far all the discussed circuit elements are linear in nature and defining the reduced flux and charge to simplify the Hamiltonian we have,

$$\text{Reduced Flux} - \phi = \frac{2\pi\Phi}{\Phi_0}$$

and

$$\text{Reduced Charge} - n = \frac{Q}{2e}$$

Here operators are defined without the hat for simplicity of the expressions. Hence,

the simplified quantum-mechanical Hamiltonian for the circuit is defined as:

$$H = 4E_C n^2 + \frac{1}{2} E_L \phi^2 \quad (2.12)$$

Where the charging energy  $E_C = \frac{e^2}{2C}$  is the energy required to add each electron of the Cooper pair to the island, and the inductive energy  $E_L = \frac{(\frac{\phi_0}{2\pi})^2}{L}$ , where  $\phi_0 = \frac{h}{2e}$  is the superconducting magnetic flux quantum.

Solving 2.12 for the eigenvalues provides an infinite series of eigenstates  $|k\rangle$ , where each eigenstate corresponds to an energy state  $E_k$  equidistant in the energy plot from the preceding and the succeeding state. The energy spacing between the energies is provided by,

$$E_{k+1} - E_k = \hbar\omega_r \quad (2.13)$$

$$\text{where, } \omega_r = \frac{\sqrt{8E_L E_C}}{\hbar} = \frac{1}{\sqrt{LC}}$$

The Hamiltonian in (12) can also be represented with using the annihilation and creation operators as

$$H = \hbar\omega_r (a^\dagger a + \frac{1}{2}) \quad (2.14)$$

It must be noted that the equidistant energy states stem from the linear characteristics of the circuit components and are not optimal to define a computational subspace. To introduce an element of non-linearity to the LC circuit-based QHO, Josephson Junctions are introduced to the circuit, replacing the linear inductor to introduce a factor of anharmonicity in energy spacing, which effectively provides the system with the desired computational subspace.

## 2.2 Josephson Junction

Josephson junction is a crucial component in superconducting sensing and, more recently, in qubit technology. It is a simple device fabricated by separating two superconducting electrodes with a thin insulating barrier, as illustrated in Figure 7.

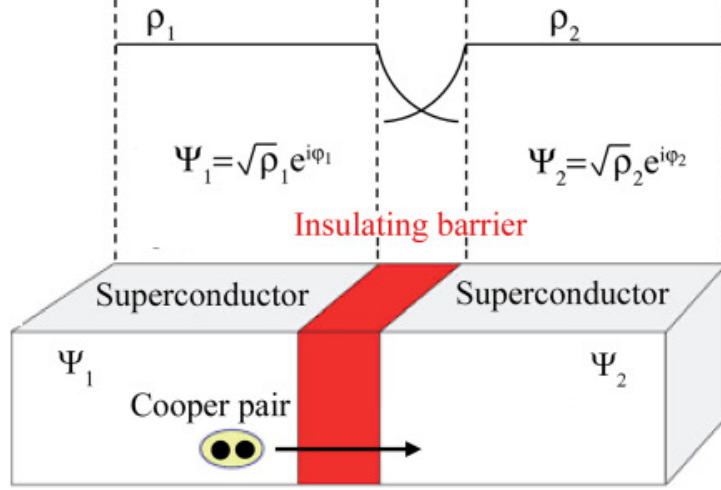


Figure 2.2: Simplified illustration of a Josephson junction depicts two superconducting electrodes separated by a thin layer of insulator, allowing electrons to quantum-mechanically tunnel through the barrier. The overlap of the macroscopic wave functions, as illustrated here, enables the tunneling of the Cooper pair.[7]

The Josephson effect describes a supercurrent of Cooper pairs across an insulating junction due to a macroscopic overlap of the wavefunction of Cooper pairs across the thin insulator, leading to their tunneling across the junction [85]. The supercurrent through the junction is defined as:

$$I_J = I_0 \sin(\delta) \quad (2.15)$$

$$V = \frac{\Phi_0}{2\pi} \frac{d\delta}{dt} \quad (2.16)$$

where,  $\delta = \phi_1 - \phi_2$  and  $I_0$  is critical current through the junction.

Differentiating 2.15 and replacing  $d\delta/dt$  with  $V$  as per 2.16 we get,

$$\frac{dI_J}{dt} = I_0 \cos(\delta) \frac{2\pi}{\Phi_0} V \quad (2.17)$$

As the time derivative of current appears proportional to voltage, the mathematical expression can be equated to an inductor, where the inductance of the junction can be defined as:

$$L_J = \frac{\Phi_0}{2\pi I_0 \cos(\delta)} \quad (2.18)$$

The inversely proportional term  $\cos\delta$  introduces the nonlinear inductance, which is exploited to create the desired anharmonicity of energy states in a superconducting qubit, providing us with a desired computational subspace.

Using 2.3, 2.14 and 2.15 we can now define the modified Hamiltonian of the system as

$$H = 4E_C n^2 - E_L \cos(\delta) \quad (2.19)$$

## 2.3 Transmon Qubit

Superconducting qubits have diversified into various types, with three main categories: charge qubits, flux qubits, and phase qubits (illustrated in Figure 2.3). The key distinction lies in modulating the inductive-to-capacitive energy ratio in the circuit, impacting the dominant energy that governs system dynamics, as reflected in the  $E_J/E_C$  ratio.

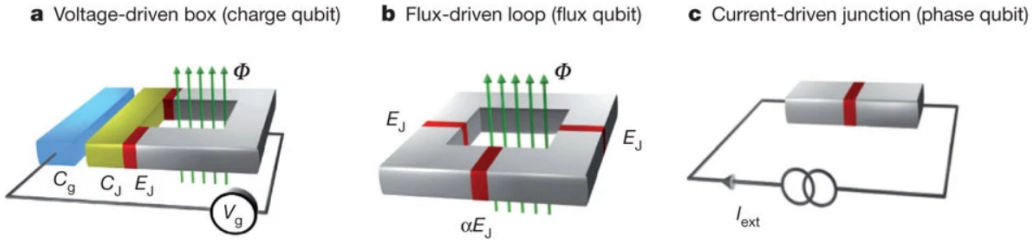


Figure 2.3: Simplified illustrations of popular superconducting circuits in various  $E_J/E_C$  ratio regimes, each functioning as qubits. [8]

Three distinct superconducting qubit configurations are illustrated in Figure 2.3. Firstly, a charge qubit, governed by a gate voltage ( $V_g$ ), integrates a SQUID loop where the effective Josephson coupling energy adapts to the threading magnetic flux  $\phi$ . The various components, such as the gate capacitor plate (blue), superconducting island

(gold), and segment of a superconducting loop (grey), play crucial roles, with each red component representing the thin insulating layer of a Josephson junction. Moving to the phase regime, the second configuration involves a superconducting loop disrupted by three Josephson junctions. Two identical Josephson junctions exhibit coupling energy ( $E_J$ ) and capacitance ( $C$ ), while the smaller junction experiences reduction by a factor  $\alpha$  ( $0.5 < \alpha < 1$ ). This three-junction loop is flux-biased with  $\phi$ . Lastly, in the same phase regime, the third configuration features a Josephson junction biased by current  $I_{ext}$ , displaying a significantly larger ratio  $E_J/E_C$ . These diverse setups demonstrate the versatility and adaptability of superconducting qubits in quantum computing applications.

When designing circuits with  $E_J \gg E_C$ , the qubit becomes less sensitive to charge noise but more prone to flux noise. Conversely, when  $E_J \ll E_C$ , the qubit becomes highly sensitive to charge noise, posing challenges in achieving high coherence. Current technologies provide flexibility in engineering the inductive part of the Hamiltonian, making it advantageous to work in the  $E_J \gg E_C$  limit, enhancing sensitivity to potential Hamiltonian changes.

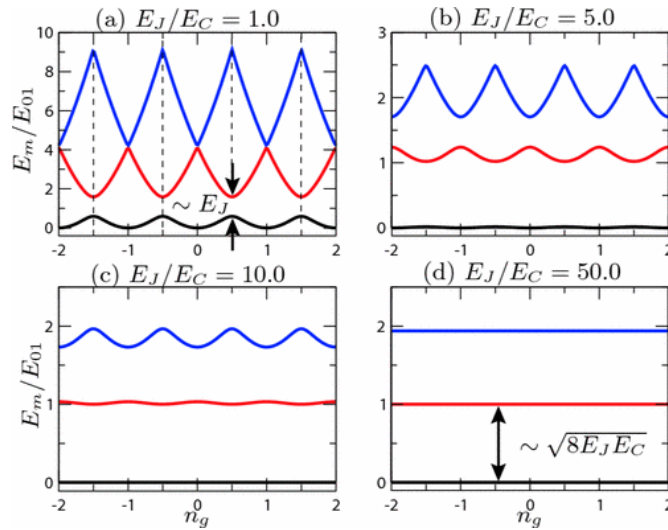


Figure 2.4: The qubit Hamiltonian's eigen energies ( $E_m$ ), depicting the initial three levels, exhibit variation based on the effective offset charge ( $n_g$ ) for varying  $E_J/E_C$  ratios. These energies are normalized with respect to the transition energy of the first two states ( $E_{01}$ ) at the  $n_g = 1/2$  degeneracy point, with the energy baseline set at the bottom of the  $m = 0$  level. Notably, vertical dashed lines in (a) highlight the charge ideal zone of operation at half-integer  $n_g$ . [9]

Transmons with significantly larger  $E_J/E_C$  ratios have emerged as a charge qubit designed to mitigate sensitivity to charge noise for superconducting quantum computing. It achieves this by significantly increasing the ratio of Josephson energy to charging energy, primarily through a large shunting capacitor (Figure 2.5). The result is energy level spacings that are nearly independent of offset charge. The term "Transmon" is derived from "transmission line shunted plasma oscillation qubit."

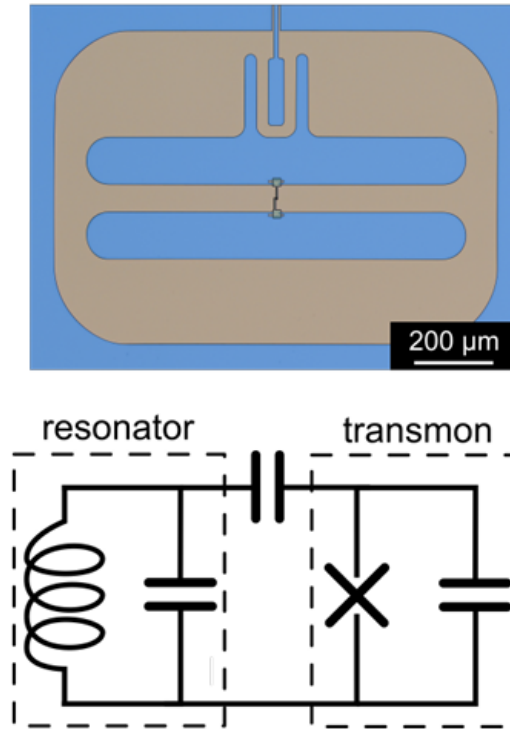


Figure 2.5: A microscopic image of a Transmon qubit device revealing its structure. Transmon comprises a Josephson junction shunted by two large capacitor islands. The corresponding circuit diagram illustrates the Transmon qubit coupled to the readout resonator through a coupling capacitor. Image from [10]

Transmons have become a preferred choice for leading industrial and academic groups due to their insensitivity to charge noise and scalability. The research presented here predominantly focuses on Transmon-based qubits, emphasizing their favorable characteristics in the pursuit of scalable and noise-resistant quantum computation. Figure 2.6 compares different superconducting qubits and their corresponding  $E_J/E_C$  ratios.

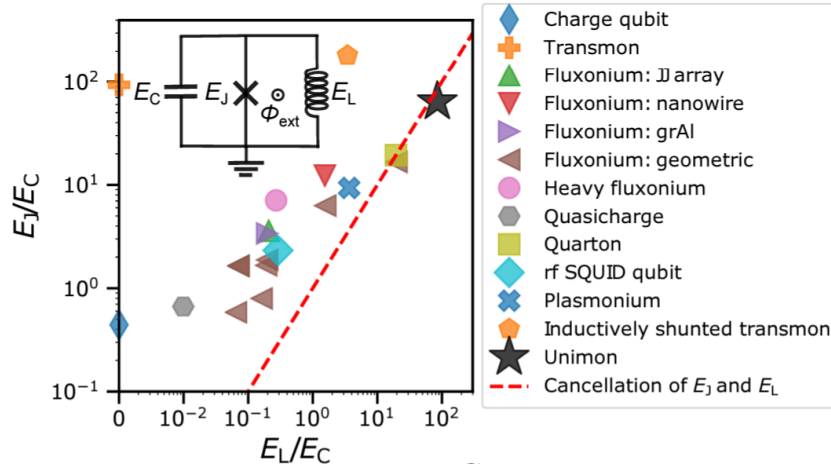


Figure 2.6: Various superconducting qubit devices plotted based on their  $E_J/E_C$  ratio. Image taken from [11]

## 2.4 Circuit Quantum Electrodynamics

Having discussed the physics of qubit devices, specifically Transmon qubits, it is essential to comprehend the dynamics of the photon-matter interaction that enables the control and readout of these qubits. The field of Circuit Quantum Electrodynamics (cQED) deals with the engineering of circuit elements to effectively couple the Transmon qubits with the environment and manipulate and measure the states while ensuring the qubit is protected from decoherence of states to the immediate environment. Any planar Transmon aimed at scalability is coupled to the environment using a superconducting resonator as a coplanar waveguide on the chip. These superconducting resonators can be considered as a collection of quantum LC oscillators discussed earlier with a well-defined resonance frequency. Figure 2.7 below shows a circuit model of a superconducting resonator in discussion.

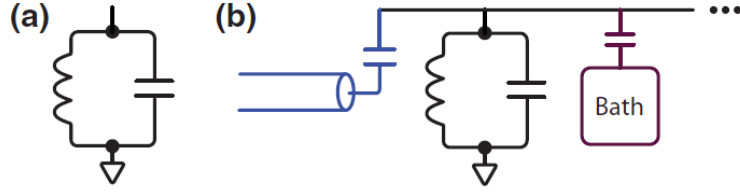


Figure 2.7: Illustrates a lumped element model of a superconducting resonator in (a). The same resonator is then depicted coupled to a transmission line and the immediate environment, referred to as a bath. This environment is typically the source of undesired noisy signals during the control and readout of qubits and poses an active challenge for the dephasing of superconducting qubits. Image from [12]

As discussed earlier, the Hamiltonian for an LC oscillator can be described by,

$$H = 4E_C n^2 + \frac{1}{2} E_L \phi^2$$

$$\text{where, } \omega_r = \frac{\sqrt{8E_L E_C}}{\hbar} = \frac{1}{\sqrt{LC}} \text{ and } Z_0 = \sqrt{\frac{L}{C}}$$

the Hamiltonian here can be modified further to the form,

$$H = \hbar\omega \left( \frac{R_Q}{2Z_0} \phi^2 + \frac{Z_0}{2R_Q} n^2 \right) \quad (2.20)$$

where, reduced resistance quantum  $R_Q = \frac{\hbar}{(2e)^2} = 1.027 \text{ k}\Omega$ ,  $\frac{R_Q}{Z_0} = \sqrt{\frac{E_L}{8E_C}}$ , and  $\phi$  is the flux through the inductor.

Diagonalizing 2.20 and evaluating the ladder operators here, we obtain,

$$a = \sqrt{\frac{R_Q}{2Z_0}} \phi + i \sqrt{\frac{Z_0}{2R_Q}} n \quad (2.21)$$

The expression above assists us in obtaining the observables for charge  $n$  and flux  $\phi$ , explicitly providing a physical sense of the zero-point fluctuations defined by,

$$\phi^{\text{ZPF}} = \sqrt{\frac{Z_0}{2R_Q}}, \quad \text{where } \phi = \phi^{\text{ZPF}} (a + a^\dagger) \quad (2.22)$$

$$n^{\text{ZPF}} = \sqrt{\frac{R_Q}{2Z_0}}, \quad \text{where } n = n^{\text{ZPF}}(a - a^\dagger) \quad (2.23)$$

Now, to understand the setup where this superconducting resonator is coupled to a Transmon qubit with the intention to control and measure the qubit using microwave signals. The description now treats the resonator coupled to a microwave transmission line that provides drive and measurement tones to the system.  $a_{\text{in}}(t)$  and  $a_{\text{out}}(t)$  are used to represent the incoming and outgoing fields of the transmission line, which eventually interacts with the qubit system. It is essential to note that fields at different instances of time are not related to each other, as described below.

$$[a_{\text{out}}(t), a_{\text{out}}^\dagger(t')] = [a_{\text{in}}(t), a_{\text{in}}^\dagger(t')] = \delta(t - t') \quad (2.24)$$

And the input-output relation of the fields can be described by,

$$a_{\text{out}} = a_{\text{in}} + \sqrt{\kappa_c} a \quad (2.25)$$

where  $\kappa_c$  is the frequency-independent coupling rate of the oscillator with the transmission line. Figure 2.8 illustrates the system of a superconducting resonator coupled with a Transmon with the corresponding energy level diagrams.

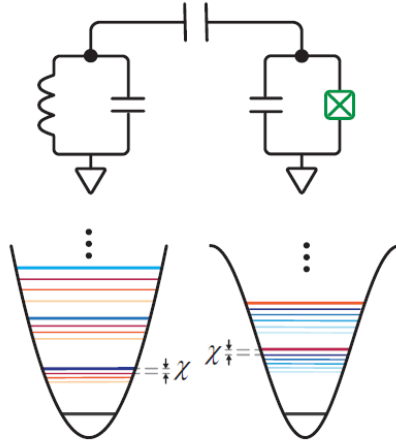


Figure 2.8: Lumped element representation of a resonator coupled to a Transmon qubit and the energy level diagram of the corresponding subsystems. Image taken from [12]

Considering the incoming and outgoing fields, the differential equation in the Heisenberg's picture can be formulated as follows:

$$\frac{\partial a}{\partial t} = -\frac{i}{\hbar}[a, H] - \frac{\kappa}{2}a - \sqrt{\kappa_c}a_{\text{in}} \quad (2.26)$$

$$\text{where } \kappa = \kappa_c + \kappa_i$$

The first term in the quantum Langevin equation 2.4 identifies the damping of the field at the rate of  $\frac{\kappa}{2}$ . Here,  $\kappa_i$  - defines the internal loss rate and represents the coupling of the system to the uncontrolled environment and  $\sqrt{\kappa_c}a_{\text{in}}$  is identified as the drive for the system. Here,  $a_{\text{in}}$  is crucial for manipulating the resonator's state but also introduces undesired field fluctuations. To address this issue, these systems usually operate in the "stiff-pump" regime, where the effects of  $\kappa_c$  are negligible compared to the resonator's frequency. In the stiff-pump approximation, the drive is characterized by the Hamiltonian,

$$\frac{H_d}{\hbar} = \epsilon(t)a^\dagger + \epsilon(t)^*a \quad (2.27)$$

$$\text{where, } \epsilon(t) = \sqrt{\kappa_c}a_{\text{in}}$$

Having discussed each component above, it is vital to delve into the integrated operation of Transmon qubits and cQED elements, understanding how they work together to control and measure the qubit states. The interaction Hamiltonian of the system can be described as,

$$H_{\text{int}} = \hbar g_0 n_R n_T = -\hbar g(a^\dagger - a)(q^\dagger - q) \quad (2.28)$$

In this context,  $g_0$  symbolizes the coupling between the subsystems, where T and R stand for Transmon and Resonator, respectively, and all charge zero-point fluctuations are encapsulated in the term  $g$ .

To further comprehend the physics the Hamiltonian is diagonalized, but for the sake of brevity of this thesis the approach in [12] is followed and an approximate diagonalized result of the Hamiltonian is presented under the commonly chosen operating regime of a

Transmon coupled with a cavity.

Here,  $g \ll |\Delta| = |\omega_T - \omega_R|$ , the large detuning between the qubit and cavity results in a dispersive interaction, avoiding resonant energy exchange. A weak anharmonicity of the qubit AHO is usually chosen, i.e.,  $\frac{E_c}{\hbar} \ll |\Delta|$ , and finally, as per Rotating Wave Approximation (RWA),  $|\Delta| \ll \omega_T + \omega_R$ .

Now, applying RWA to the interaction Hamiltonian we get

$$\frac{H_{\text{int}}}{\hbar} = (aq^\dagger - qa^\dagger) \quad (2.29)$$

Utilizing 2.29 to write the Langevin equations in the Heisenberg picture we get,

$$\frac{\partial a}{\partial t} = -i(\omega_R - i\frac{\kappa}{2})a - igq \quad (2.30)$$

$$\frac{\partial q}{\partial t} = -i\omega_T q - iga - \frac{i}{\hbar}[q, H_{4(+)}\phi^{\text{ZPF}}(q + q^\dagger)] \quad (2.31)$$

Diagonalizing the linear part of 2.31 by the matrix,

$$M = \begin{pmatrix} \omega_R - i\frac{\kappa}{2} & g \\ g & \omega_T \end{pmatrix} \quad (2.32)$$

the eigen values to the first order are described by,

$$\tilde{\omega}_R = \omega_R + \frac{g^2}{\Delta} - i\frac{\kappa}{2} + i\left(\frac{g}{\Delta}\right)^2 \frac{\kappa}{2} \quad (2.33)$$

$$\tilde{\omega}_T = \omega_T - \frac{g^2}{\Delta} - i\left(\frac{g}{\Delta}\right)^2 \frac{\kappa}{2} \quad (2.34)$$

The resonator and Transmon frequencies  $\tilde{\omega}_R$  and  $\tilde{\omega}_T$  in the system with dispersive coupling experience shifts compared to the uncoupled system due to the Lamb shift given by

$$\Lambda_x = \frac{g^2}{\Delta} \quad (2.35)$$

Additionally, the Transmon experiences dissipation from the cavity, quantified by the Purcell rate, which is crucial to consider.

$$\Gamma_P = \left(\frac{g}{\Delta}\right)^2 \kappa \quad (2.36)$$

The Purcell rate introduces a potential trade-off between achieving a substantial Transmon-resonator coupling for rapid operations and preserving the qubit's lifetime. Nevertheless, practical solutions involve the effective mitigation of the Purcell effect through the implementation of well-designed Purcell filters. In subsequent chapters, efforts to suppress Purcell decay using these filters will be explored.

While an extensive derivation of the Transmon-cavity Hamiltonian is presented in [12] it is of essence to note the effective Hamiltonian in the dispersive regime,

$$\frac{H}{\hbar} = \omega_T q^\dagger q + \omega_R a^\dagger a - \frac{\alpha}{2} q^{\dagger 2} q^2 - \frac{K}{2} a^{\dagger 2} a^2 - \chi(q^\dagger q)(a^\dagger a) \quad (2.37)$$

where,

$$K = \frac{E_J}{2\hbar} (\phi^{\text{ZPF}})^4 \left(\frac{g}{\Delta}\right)^4 = \frac{2E_C}{\hbar} \left(\frac{g}{\Delta}\right)^4 \quad (2.38)$$

$K$  and  $\chi$  are denoted as the self-Kerr and cross-Kerr nonlinearities, respectively, characterizing the interaction between the resonator and the Transmon. In a physical sense, the impact of dispersive coupling manifests as a state-dependent frequency shift between the two modes. The coupling is deemed to be in the strong dispersive regime when this state-dependent shift surpasses the linewidth of the resonator.

Having grasped the physics of superconducting qubits and cQED, the subsequent chapters delve into the intricacies of Transmon qubit design and optimization methods, all directed toward achieving a scalable platform. With the understanding of the Physics of superconducting qubits and cQED, the following chapters focus on the design of Transmon qubits and optimization methods aimed at a scalable superconducting qubit platform.

# CHAPTER 3

## Methods

This chapter details the tools and techniques used to design, simulate, and characterize the devices and associated packaging for optimal operation at the temperature range of 15mK, maintained inside the dilution fridge.

### 3.1 Device Design and Simulation

#### 3.1.1 Qiskit Metal

Qiskit Metal stands as an open-source Electronic Design Automation (EDA) tool developed by IBM [86], with a primary focus on the layout integration of superconducting circuits using Python. This tool offers a framework for quantum device design, incorporating auto-routing algorithms and analysis frameworks like the lumped oscillator model and energy participation ratio. These features empower users to simulate the performance of their devices. Additionally, Qiskit Metal is compatible with standard electromagnetic simulation tools such as ANSYS HFSS, facilitating in-depth analysis of the design before the final tapeout.

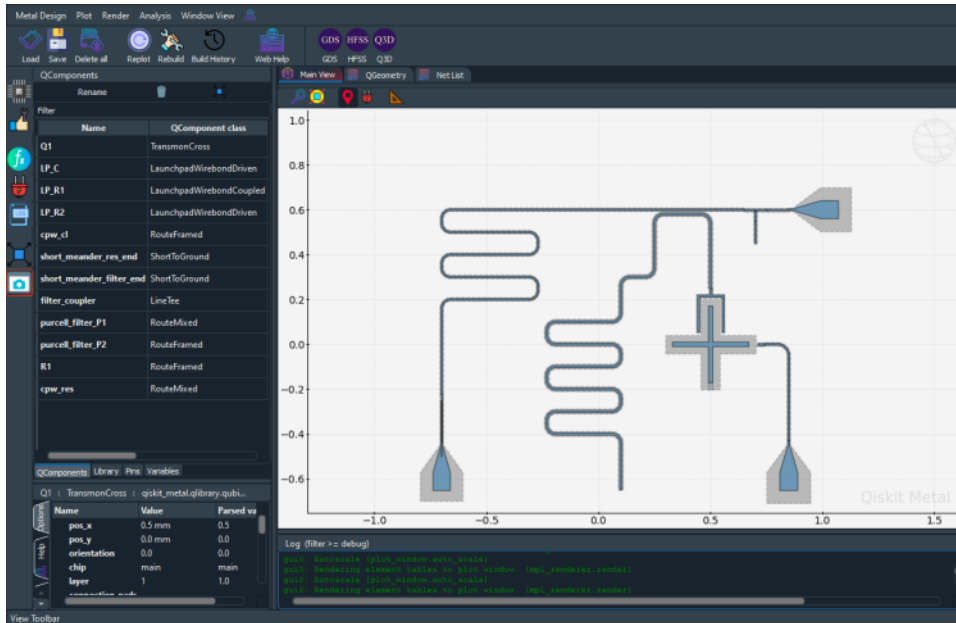


Figure 3.1: Displays the Graphical User Interface (GUI) provided by Qiskit Metal. This interface allows users to adjust design parameters and observe layout changes before finalizing the design. The GUI can be utilized either in conjunction with Python or as a standalone interface.

The devices discussed in the upcoming chapters have been designed and analyzed using Qiskit Metal and the associated tools available within the framework.

### 3.1.2 Lumped Oscillator Model

The Lumped Oscillator Model (LOM), integrated into Qiskit Metal, serves as an analytical tool for designing and analyzing the devices for quantum processors. This tool employs a modular analysis flow, breaking down the system into subsystems and simulation cells. These cells, representing small domains of the device layout, enable independent analysis using analytical or numerical simulations, enhancing computational efficiency. Subsystems act as familiar building blocks, optimizing the modeling process. Figure 3.2 illustrates the partitions of the system.

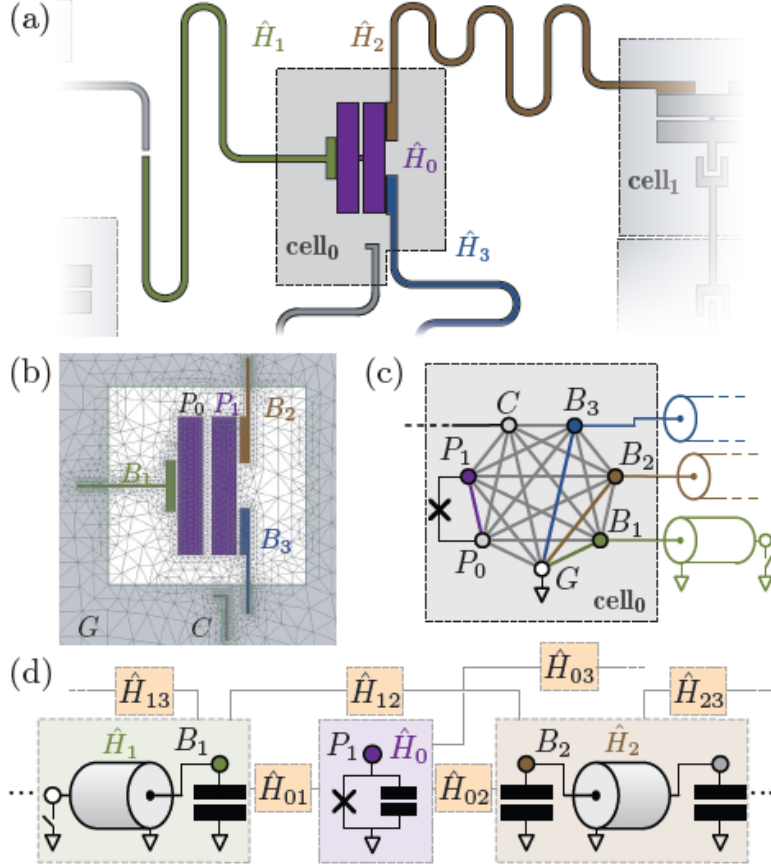


Figure 3.2: Illustration provides an overview of the methodology employed by the Lumped Oscillator Model. (a) This illustration showcases a section of the layout from a larger quantum processor. The highlighted section considers a transmon qubit with two large capacitive plates and four co-planar waveguides used for readout, bus coupling resonators, and a charge line. The partition illustrates the classification into subsystems and the corresponding Hamiltonian for each subsystem that LOM intends to evaluate. (b) Further subdivision of the subsystems into simulation cells is illustrated. (c) The partial schematic defines the subsystem network to effectively evaluate the pairwise interaction Hamiltonian in the presence of all the subsystems in the network. (d) The illustration depicts the reduced, dressed subsystems, serving as essential building blocks, along with their dressed interactions. Image source [13]

The objective of LOM is to construct the composite system Hamiltonian  $\hat{H}_{\text{full}}$  within the limits of the analytical quasi-lumped approximation under the LOM method, considering no other approximations. The Hamiltonian is described by 3.1.

$$\hat{H}_{\text{full}} = \hat{H}_0 + \sum_{n=1}^K \hat{H}_n + \sum_{n=0}^{K-1} \sum_{m=n+1}^K \hat{H}_{nm} \quad (3.1)$$

Here, each sub-system is connected to  $K$  neighbors, where  $\hat{H}_0$  and  $\hat{H}_n$  denote the dressed Hamiltonians of the sub-system and its  $n^{th}$  neighbor, respectively. The interaction between the  $n^{th}$  and  $m^{th}$  sub-systems is denoted by  $\hat{H}_{nm}$  and is characterized by,

$$\hat{H}_{nm} = \frac{\hat{Q}_n \hat{Q}_m}{C_{nm}^{\text{eff}}} + \frac{\hat{\Phi}_n \hat{\Phi}_m}{L_{nm}^{\text{eff}}} \quad (3.2)$$

Where,  $C_{nm}^{\text{eff}}$  is the coupling capacitance and  $L_{nm}^{\text{eff}}$  is the inductance between the  $n^{th}$  and  $m^{th}$  sub-systems.

While a detailed breakdown of the LOM method is documented in [13], it is crucial to note that the efficiency of the LOM method was validated against experimental results. A two-fold improvement in experimental agreement was observed compared to methods making weak coupling approximations and not fully considering the non-perturbative dressing of distributed modes. Further details and a comprehensive list of agreements on different parameters can be found in [13].

The remarkable alignment of this tool with experimental results led us to employ it for the analysis of the devices described in this thesis.

### 3.1.3 Energy Participation Ratio (EPR)

In an effort to comprehend the non-linear interactions of multi-mode distributed quantum devices and circuits, as discussed in this thesis, the Energy Participation Ratio (EPR) [14] computational tool is integrated into the Qiskit Metal framework. This allows for evaluating EPR in Josephson junction-based circuits, using eigenmode simulations on an electromagnetic solver like ANSYS HFSS. Figure 3.3 describes the overview of the EPR method described here,

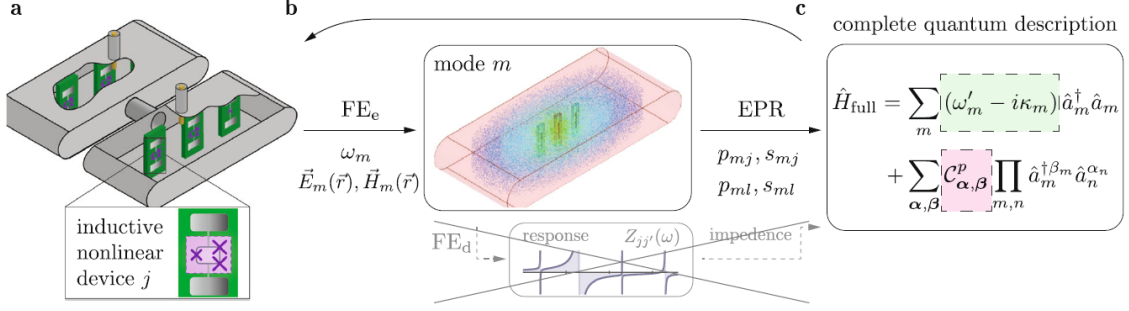


Figure 3.3: Illustration provides a conceptual overview of the method with an example quantum device. (b), Results from a finite-element eigenmode analysis (FEE) of the Josephson circuit linearized about its equilibrium are presented, showcasing the eigenfrequency and electric/magnetic fields. Notably, additional FE-driven simulations (FE<sub>d</sub>) are unnecessary, and the impedance matrix is not calculated. In (c), the Hamiltonian  $\hat{H}_{\text{full}}$ , encompassing nonlinear interactions to arbitrary order, is computed directly from eigenanalysis via Energy Participation Ratios. Dissipative contributions are also calculated from loss EPRs, which is unique to the EPR method. The iterative modification of the classical model's geometry allows for the extraction of desired dissipative and Hamiltonian parameters. Image source [14]

EPR quantifies the energy stored in each element of the circuit, expressed as a value ranging from 0 to 1. This information is instrumental in defining the quantum Hamiltonian for the system under analysis.

The EPR method begins by separating the system Hamiltonian identified as  $\hat{H}_{\text{full}}$  as below,

$$\hat{H}_{\text{full}} = \hat{H}_{\text{lin}} + \hat{H}_{\text{nl}} \quad (3.3)$$

Here,  $\hat{H}_{\text{lin}}$  consists terms related to the linear response of the cavity and junction.

$$\hat{H}_{\text{lin}} = \hbar\omega_c \hat{a}_c^\dagger \hat{a}_c + \hbar\omega_q \hat{a}_q^\dagger \hat{a}_q \quad (3.4)$$

Where,  $\omega_c$  and  $\omega_q$  are the angular frequencies of the cavity and qubit eigenmodes, and  $\hat{a}_c$  and  $\hat{a}_q$  are the respective annihilation operators. Consequently,  $\hat{H}_{\text{nl}}$  includes terms associated with the non-linear response of the junction and is represented by,

$$\hat{H}_{\text{nl}} = -E_J \left[ \cos(\hat{\varphi}_j) + \frac{\hat{\varphi}_j}{2} \right] \quad (3.5)$$

where,  $E_J$  is the Josephson energy and

$$\hat{\varphi}_j = \varphi_q(\hat{a}_q + \hat{a}_q^\dagger) + \varphi_c(\hat{a}_c + \hat{a}_c^\dagger) \quad (3.6)$$

and the classical variable flux is defined as

$$\varphi_j = \int_{-\infty}^t \frac{v_J(\tau)}{\phi_0} d\tau \quad (3.7)$$

$\hat{H}_{lin}$  is associated with quantities from an eigenanalysis of the classical distributed circuit,  $\omega_c$ , and  $\omega_q$ . EPR focuses on extracting and computing these quantities, to ascertain the unknown parameters to evaluate the linear part of the Hamiltonian. Once obtained the participation of each junction in a particular mode  $m$  is determined.  $p_m$  is the ratio of inductive energy stored in a junction to the total energy stored in mode  $m$ . and can be determined by 3.8

$$p_m = \frac{\langle \psi_m | \frac{1}{2} E_J \hat{\varphi}_j^2 | \psi_m \rangle}{\langle \psi_m | \frac{1}{2} \hat{H}_{lin} | \psi_m \rangle} \quad (3.8)$$

Where,  $|\psi\rangle$  represents a coherent state or a Fock excitation of mode  $m$ . Further, the zero point fluctuations are also represented in terms of the participation ratios described in 3.8.

$$\varphi_p^2 = p_q \frac{\hbar\omega_q}{2E_J} \quad \text{and} \quad \varphi_c^2 = p_c \frac{\hbar\omega_c}{2E_J}$$

At this point it is sufficient to calculate the non-linear part and consequently the full Hamiltonian of the system. While designing a system using EPR, extracting transition frequencies and nonlinear couplings between modes from  $\hat{H}_{full}$  is necessary. Depending on the case, this extraction can be performed approximately or exactly using numerical or analytical techniques. The process is straightforward if  $\hat{H}_{nl}$  is a perturbation to  $\hat{H}_{lin}$ , allowing for an approximation of  $\hat{H}_{full}$  in our qubit-cavity example by the effective as described in 3.9

$$\hat{H}_{\text{eff}} = (\omega_q - \Delta_q)\hat{n}_q + (\omega_c - \Delta_c)\hat{n}_c - \chi_{qc}\hat{n}_q\hat{n}_c - \frac{1}{2}a_q\hat{n}_q(\hat{n}_q - 1) - \frac{1}{2}a_c\hat{n}_c(\hat{n}_c - 1) \quad (3.9)$$

where,  $\hat{n}_i = \hat{a}_i^\dagger \hat{a}_i$  signifies the excitation operator,  $\Delta_i$  is the lamb shift,  $a_i$  is the respective anharmonicities and  $\chi_{qc}$  denotes cross-Kerr coupling between qubit and cavity. Further the qubit and cavity anharmonicities can be described by 3.10 and cross-Kerr coupling by 3.11

$$\alpha_i = \frac{1}{2} \chi_{ii} = p_j^2 \frac{\hbar \omega_i^2}{8E_J} \quad (3.10)$$

$$\chi_{qc} = p_q p_c \frac{\hbar \omega_q \omega_c}{4E_J} \quad (3.11)$$

Detailed and well-documented physics behind the EPR method is presented in [14] it does mention the following relation between  $p_c$  and  $p_m$  as described below

$$0 \leq p_q, p_c \leq 1 \quad \text{and} \quad p_q + p_c = 1$$

The outcomes obtained from the EPR method, akin to the LOM mentioned earlier, were compared against experimental results, demonstrating substantial agreement with the experimental findings.

### 3.1.4 PCB Design and Simulation

The work detailed in Chapter 6 discusses the design and fabrication of printed circuit boards (PCBs) specifically crafted for RF and cryogenic applications. Crafting such a platform required precise management of design parameters, encompassing layout automation, stackup control, and impedance matching.

Altium Designer was selected for designing these PCBs to house the superconducting qubit devices presented in Chapter 4. This choice was driven by its comprehensive features and meticulous Design Rule Check (DRC) protocol.

Following the design phase, simulations were conducted using SIwave by ANSYS, a dedicated PCB and package electromagnetics simulation software. This tool served for cross-verification of track impedances and eigenmodes of the PCB. Detailed results of this analysis are presented in Chapter 6.

## 3.2 Experimental Setup and Characterization Methodology

The experimental configuration for a superconducting qubit setup necessitates a dilution fridge to maintain the device at ultra-low temperatures, and arbitrary waveform generators (AWGs) and spectrum analyzers for effective characterization of the devices within the dilution fridge. The following subsections provide insights into the overall measurement setup and the process of characterizing a Josephson parametric amplifier.

### 3.2.1 Measurement Setup and Dilution Fridge

Superconducting qubits, and indeed any qubit platform, demands a sophisticated array of equipments to ensure isolation from the environment and maintenance at cryogenic temperatures, allowing for effective control and manipulation of the devices.

At the core of this setup is the cryogen-free dilution refrigerator, a closed-loop cooling system capable of providing temperatures in the order of  $10mK$  without the need for moving parts at the low-temperature stages. In our experimental configuration (Figure 3.4), we employed a Bluefors dilution refrigerator with a base temperature of approximately  $15mK$ . A dilution refrigerator comprises multiple cooling stages connected by numerous RF and microwave cables.

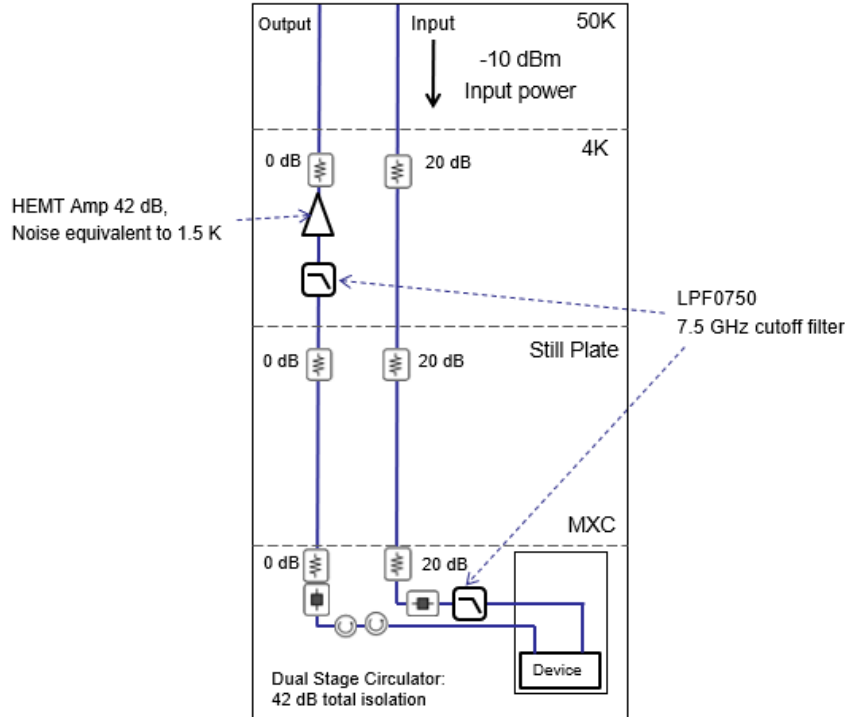


Figure 3.4: Schematic of the experimental setup for qubit characterization within the Bluefors dilution fridge. The outer box represents the dilution fridge, with each inner dashed line depicting a cooling stage. The devices operate in the bottom most stage, maintaining temperatures  $15\text{mK}$ . The blue lines in the schematic denote the microwave lines responsible for conveying input signals to the device and transmitting output signals to and from the room-temperature electronics.

Superconducting Qubits are also extremely sensitive to noise, even from minute amounts of thermal noise like Johnson-Nyquist (J-N) noise, generated by the thermal agitation of electrons in the microwave lines can disrupt the characterization of the qubits. Cryo attenuators are crucial in mitigating J-N and other noise sources, particularly on the drive lines in setups like these.

To generate input signals, Arbitrary Waveform Generators (AWGs) are employed (kept at room temperature), sending requisite microwave pulses down to the device. These signals are attenuated to minimize noise before reaching the cryogenic temperatures of the device. Subsequently, circulators and isolators are strategically placed to guide only the desired signals through the output line. To enhance the output signal, a High Electron Mobility Transistor (HEMT) amplifies it before reaching spectrum analyzers at room

temperature. HEMT operates at microwave frequencies, combining low noise figures and superior amplification, thus making them desirable for this setup.

Thermal load management is crucial in this setup, and sufficient care was taken to choose components that were specifically designed for reliable operation at cryogenic temperatures, minimizing self-heating and ensuring efficient noise reduction.

### 3.2.2 Josephson Parametric Amplifier

Superconducting qubits platforms operate and transfer information through microwave signals. During the measurement of these devices, the signals are recorded at room temperature electronic devices, as discussed earlier. As the microwave signals for these systems typically consist of very few photons, amplification is necessary to achieve reasonable signal-to-noise ratios. Low-noise amplification of these signals is crucial. Thus, the use of superconducting Josephson parametric devices, such as a Josephson Parametric Amplifier (JPA), as the one discussed here, becomes essential. A part of the work documented here was installing and characterizing a Raytheon broadband JPA TM-2035 (Figure 3.5).

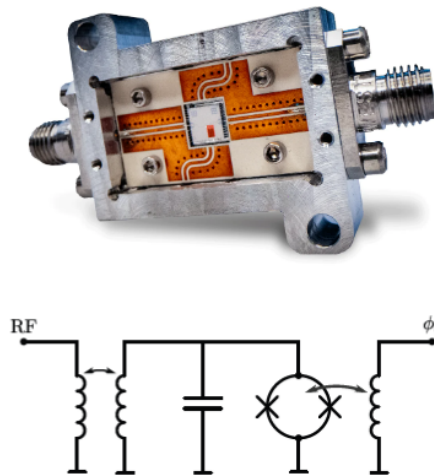


Figure 3.5: JPA TM-2035 by Raytheon (top) circuit schematic (below) was installed and characterized.[15]

At the core of a JPA is a superconducting quantum interference device (SQUID)

combined with a coplanar waveguide, forming a tunable nonlinear microwave resonator. A squid consists of two Josephson junctions in the loop of a superconducting circuit (Figure 3.6). Its frequency can be adjusted in situ via an external magnetic field.

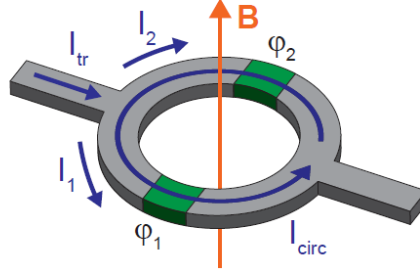


Figure 3.6: Schematic of a superconducting quantum interference device (SQUID). [16]

While the theoretical background of the physics of SQUIDS in the context of a JPA is well documented in [78], it is of essence to point out the non-linear inductance (3.12) of a SQUID here to comprehend how the external flux can be used to tune the inductance of the circuit which in term is of benefit for a device like JPA.

$$L_s(\Phi_{\text{ext}}) = \frac{\Phi_0}{2\pi I_{\text{max}}} = \frac{\Phi_0}{4\pi I_c \cos \pi \frac{\Phi_{\text{ext}}}{\Phi_0}} \quad (3.12)$$

In the output (readout) circuitry of the experimental setup inside the dilution refrigerator, the signal passes through a resonator circuit, inducing a qubit state-dependent phase shift. The JPA then amplifies the signal in a reflectometer configuration with a circulator. It undergoes further amplification by HEMT before being directed to a room-temperature in-phase/quadrature demodulation circuit, and before being digitally processed, output determines the qubit state. The experimental setup to characterize the JPA is described in Figure 3.7.

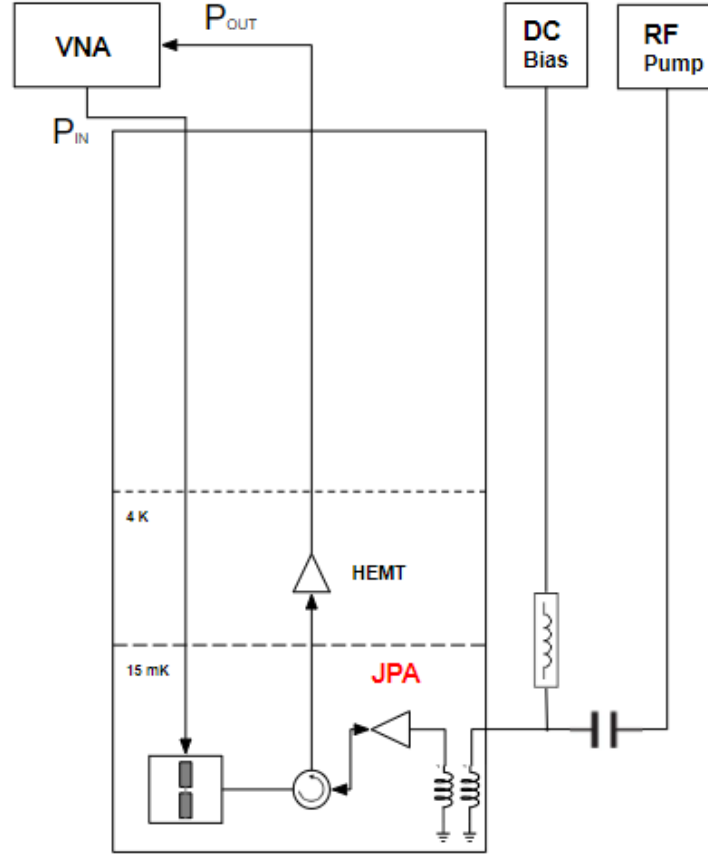


Figure 3.7: Schematic of the experimental setup for characterizing the qubit. The input signals were sent from a vector network analyzer (VNA) at room temperature, and in the input line was attenuated by  $-60\text{dB}$  (not shown in the figure). A cavity with a qubit was placed in the circuit, and the effects of the same are pronounced in the results obtained during characterization.

Effective qubit readout necessitates maintaining a small probe signal power to prevent incoherent fluctuations in the qubit state. The goal is to maximize the signal-to-noise ratio in the readout signal, which necessitates incorporating a preamplifier that approaches the quantum limit for amplification. However, the constrained by the available cooling power at the lowest stages of the dilution refrigerator ( $\sim 10\mu\text{W}$ ) pose further limitations. Despite the effectiveness of standard low-noise cryogenic solid-state amplifiers, their power dissipation in the order of milliwatts prompted the introduction of a Josephson Parametric Amplifier (JPA) in the readout circuitry to address these challenges.

The comprehensive derivation of the underlying physics of the Josephson Parametric

Amplifier (JPA) is thoroughly covered in [16, 87]; however, for brevity, it is not delved into here. The JPA is operated in a non-degenerate mode, with the pump frequency ( $\omega_{pump}$ ) set to twice the signal frequency  $2\omega_{signal}$  for efficient operation. The characterization of the JPA involved two key steps:

1. Setting the bias current by sweeping the frequency and current of the input signal.
2. Tuning the RF pump.

Figure 3.8 presents the results from step 1, where the current was swept for a fixed input power (VNA output power), and the phase response was observed. Reference lines were employed to track the relative shift of the phase as the DC bias was tuned from 0A.

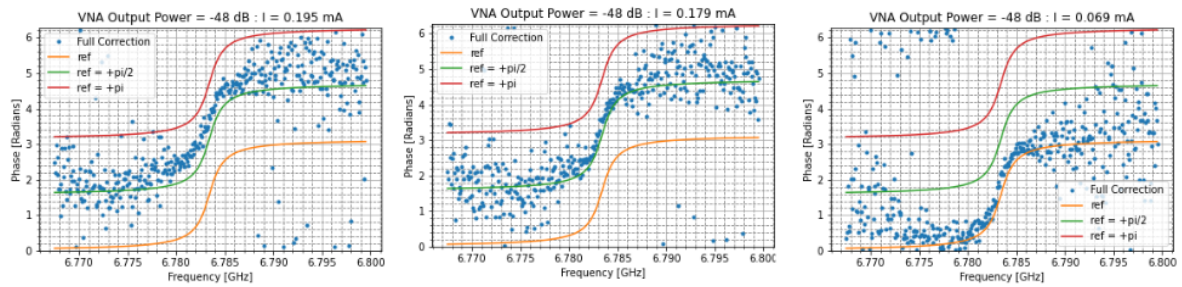


Figure 3.8: Phase of  $S_{21}$ , with a specific bias current, as the frequency is swept across the vicinity of the cavity frequency.

Further Figure 3.9 illustrates the phase of  $S_{21}$  recorded as both bias current and frequency were swept for a specific VNA power. The objective was to pinpoint an optimal point within the periodic phase response as the bias current was varied.

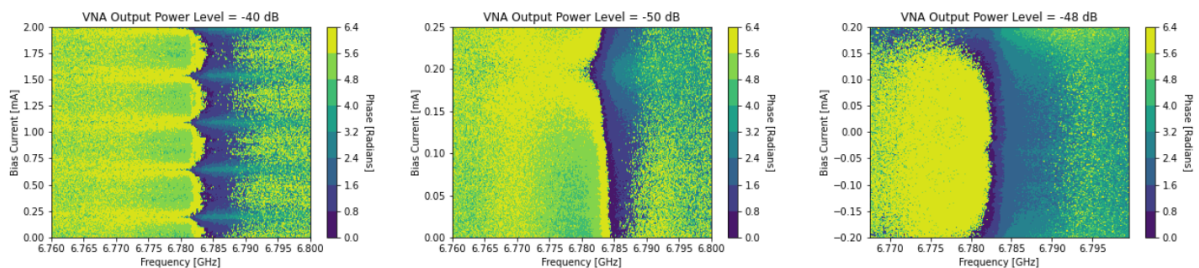


Figure 3.9: Phase of  $S_{21}$  for the JPA, covering a complete sweep of bias current and frequency across the vicinity of the cavity frequency. Sweeps from left to right zoom in on a smaller range of bias current to find an optimal current of operation.

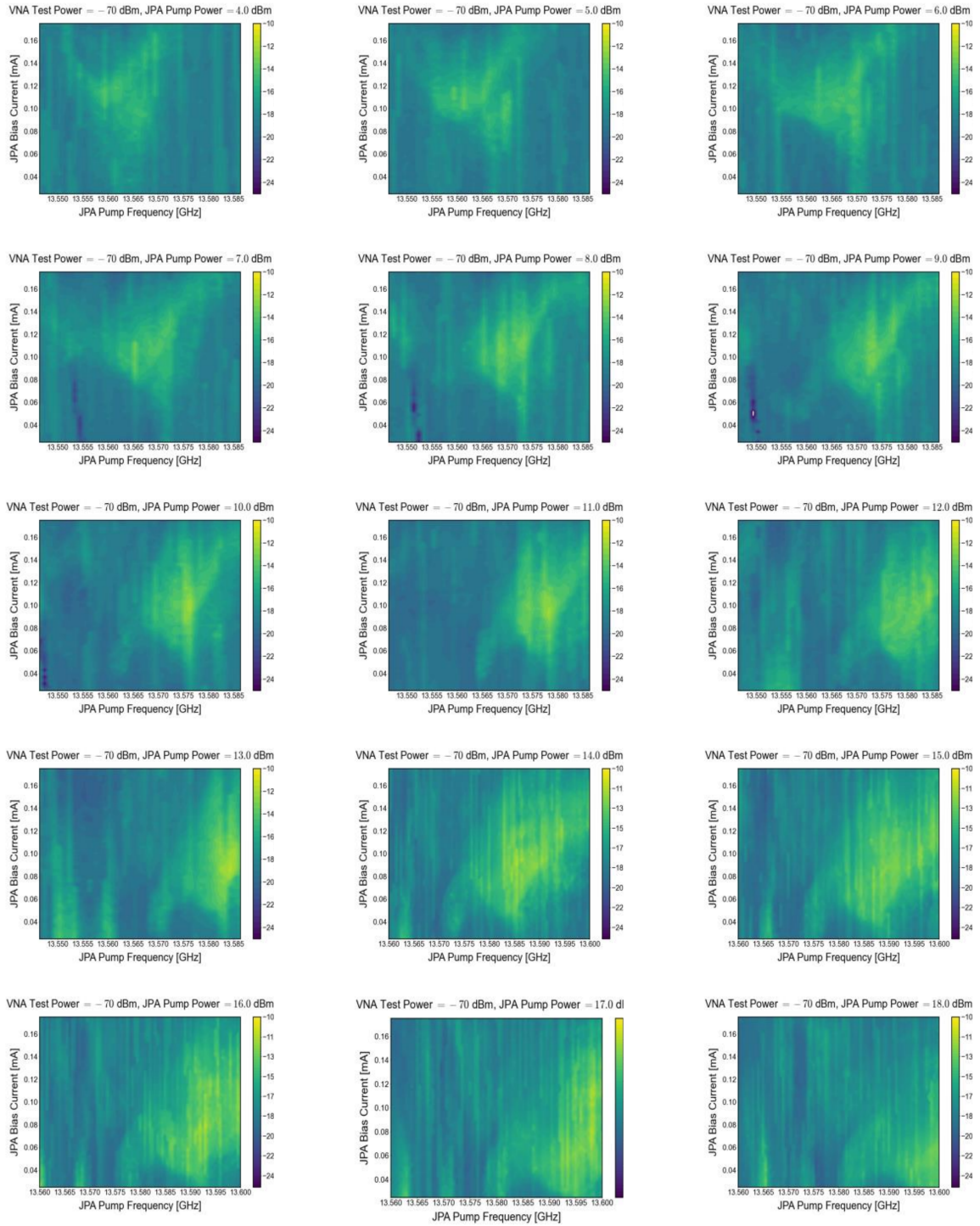


Figure 3.10: Presents the magnitude of  $S_{21}$  measurements, with a sweep of bias current and pump frequency. The JPA input signal power was set at -70 dB for all the experiments, and subsequent experiments were also performed by sweeping the JPA pump power, as illustrated in each section while keeping the other sweeping ranges the same.

An optimal signal and pump frequency were obtained from the above experiments, while an approximate value of the bias current was comprehended. Step 2 of the characterization involved sweeping through the bias current and the pump frequency to identify the region for optimal amplification by examining the amplitude of the output signal. The pump power was also swept, and it was observed to shift the region of maximum amplification, as depicted in Figure 3.10. Finally, the JPA was tested with the power turned on and off, as presented in Figure 3.11, to assess the limits of amplification. The pump frequency here was for maximum amplification, and it was observed to maximize amplification for  $\omega_{signal} = 6.84$  GHz, with the optimal bias current set at 0.1 mA, while the pump power was set at 11 dBm.

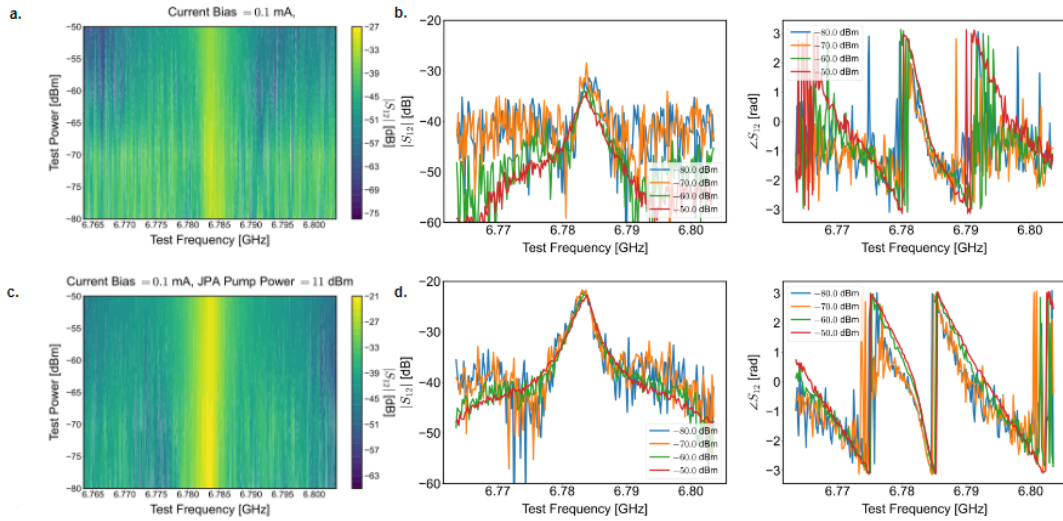


Figure 3.11: Illustrates the performance of the JPA with and without RF pump. Panels a. and b. show the JPA's performance when no pump is applied, indicating no amplification. Panel A sweeps the input power against the input frequency in the vicinity of  $\omega_{signal}$ . Panel B reports the magnitude and phase of the output signal for different input signal powers. Note that the signal power is close to the cavity frequency. Panels c. and d. depict the performance of the JPA with the RF pump, showing an amplification of 10 dB in this case. The experimental setup and conditions for both trials were kept the same.

Figure 3.11 reports an amplification of  $\sim 10$  dB. It leaves room for further optimization of the calibration process. A reduction in amplification could be attributed to the presence of the cavity in the input line during calibration, which might affect the optimization of operating parameters.

# CHAPTER 4

## Planar Qubits

The previous chapters delved into the physics and experimental setup surrounding a superconducting qubit device. This chapter shifts its focus to the device design and architecture employed within this thesis.

The study of superconducting qubits remains divided into two main categories. The first involves 3D architectures, where a vacuum inside a cavity serves to provide the linear modes in the cQED Hamiltonian. These modes weakly couple to transmission lines through coaxial center pins extended into the cavity through the cavity wall, as depicted in Figure 4.1.

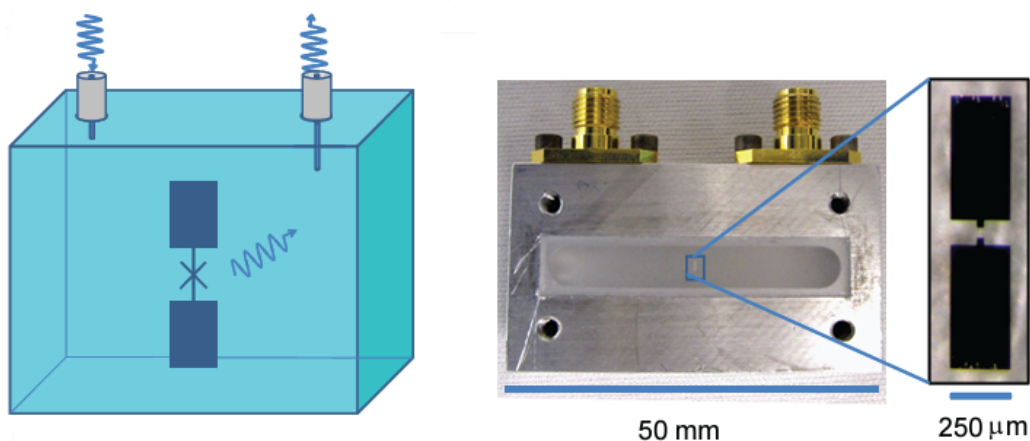


Figure 4.1: Transmon qubit coupled to a 3D cavity. Illustration of a Transmon placed in a 3D cavity (left), Picture of fabricated cavity and zoomed-in image of Transmon placed inside the cavity. Figure from ref [17]

The second category encompasses planar qubits, which are patterned on a wafer using lithographic techniques. These qubits couple to the environment using on-chip coplanar

waveguides and are then bonded on a PCB or interposer, eventually interfacing with the microwave lines in the dilution refrigerator.

The 3D architecture remains popular in various groups due to its inherent advantages, such as the small size of devices and the provision of a clean electromagnetic environment. Its lack of supporting structures reduces engineering efforts to suppress spurious modes in the device package, and it demonstrates good coherence times owing to the small surface-to-volume ratio of quantum modes. However, these advantages are often overshadowed when considering platform scaling. The large spatial extent of the 3D cavity electromagnetic field makes it challenging to achieve desired mode isolation within the same cavity. Additionally, the sheer volume of each device and the cavity renders it impractical for a scenario where scaling up these systems involves millions of physical qubits.

Considering these aspects, and given that scaling up superconducting qubits is the central theme of the presented work, the architecture of planar qubits was selected. The following section delves into the device design, simulation results, and challenges associated with this choice.

## 4.1 Planar qubit with on-chip Purcell Filters

The type of superconducting qubit for the work outlined here is the Transmon qubit, which was selected due to its mentioned benefits in Chapter 2.3. While designing a Transmon, the primary objective is to replicate the circuit depicted in Figure 2.5, where a capacitive pad and a Josephson junction form the Transmon qubit. A coplanar waveguide, capacitively coupled to the Transmon, acts as the resonator, and the principles of cQED govern its physics, as discussed in Chapter 2.4.

Over the years, various innovations in the device layout of Transmons to optimize the footprint of each device have been proposed, particularly in designing the capacitor pads. The presented designs below showcase two popular architectures. The first features larger capacitor pads with a Josephson junction in the center as illustrated in Figure 2.5. It is quite an intuitive layout once one comprehends the underlying circuit. In contrast, the

second, popularly known as X-mon, has 'X'-shaped pads serving as capacitors, with the Josephson junction (or SQUID, in case tunability of junction inductance is desirable). X-mons have gained more popularity in the industry, especially in platforms focused on scalability, owing to their smaller footprint and ease of coupling to coplanar waveguide resonators.

When designing a Transmon or any qubit, minimizing decay to the immediate environment is a crucial consideration. While a strong coupling to the cavity, in this case, the resonator, facilitates fast measurement, it also introduces an undesirable decay channel. Careful engineering of the devices and associated systems becomes essential to mitigate the effects of Purcell decay, as mentioned in equation 2.36. The designs presented below incorporate on-chip Purcell filters to address and implement solutions for this challenge.

#### 4.1.1 Transmon Qubit with a Notch Filter

In the pursuit of designing a Purcell filter, a crucial factor is comprehending how the Purcell rate can be minimized. Drawing inspiration from a device reported in [18], where the Purcell rate was reduced by a factor of 50 when the qubit frequency was placed in the rejection band of the filter. The design also reported achieving qubit measurements within 140 ns, attaining high fidelities ( $F|1\rangle = 98.7$  and  $F|0\rangle = 99.3$ ).

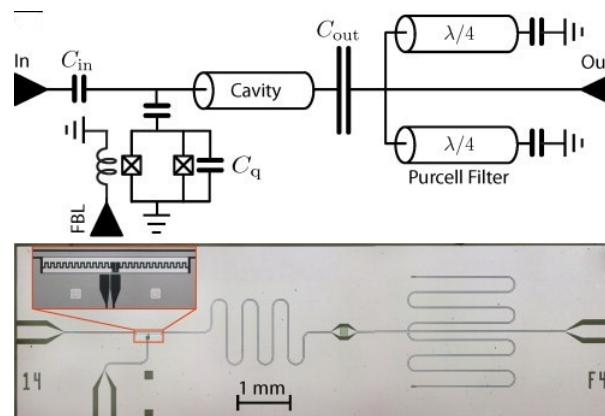


Figure 4.2: Circuit and device layout proposed in [18]

The device layout for this qubit device is depicted in Figure 4.3. The design encom-

passes a Transmon qubit with charge and flux bias lines for qubit control. It is capacitively coupled by a  $\lambda/2$  resonator for readout, further capacitive coupling to the output pad. Capacitors are strategically employed for input-output coupling of the resonator, ensuring precise control over efficient modulation of  $\kappa$ . The output feed is additionally coupled to two  $\lambda/4$  resonator stubs, functioning as the Notch filter, to keep the qubit frequency in the rejection band of the filter as presented in [18].

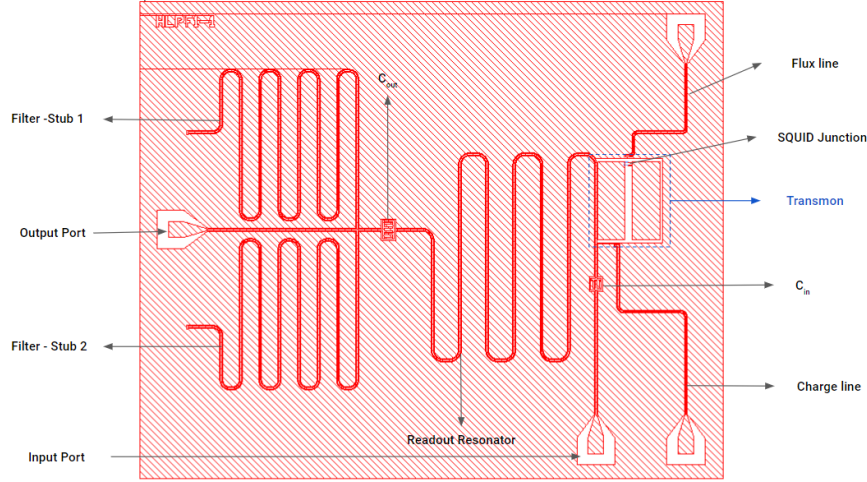


Figure 4.3: Depicts the layout for Device 1, featuring a Transmon qubit with SQUID junctions for flux tunability. The design incorporates charge and flux lines for qubit control. The readout resonator is a  $\lambda/2$  waveguide open to the ground on both ends, coupled using finger capacitors  $C_{in}$  ( $C_{out}$ ) on the input (output) side for effective input-output coupling control. Filter stubs 1 and 2 serve as the notch filter, implemented as  $\lambda/4$  coplanar waveguides. All input-output lines are impedance-matched to  $50 \Omega$ .

The design was then simulated through eigenmode simulations, as presented in Figure 4.4, for the first three modes to comprehend the native modes of each device component. Subsequently, qubit parameters were extracted using EPR and LOM analyses, as detailed in Table 4.1.

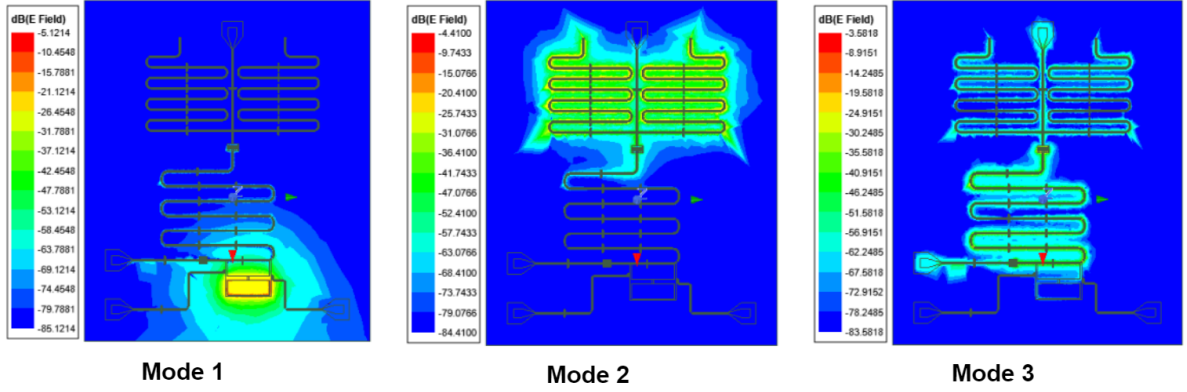


Figure 4.4: The first three eigenmodes for the device are presented here: Mode 1 at 4.29 GHz, Mode 2 at 4.56 GHz, and Mode 3 at 7.43 GHz.

Table 4.1: Device parameters for Transmon with Notch Filter extracted using EPR method.

Qubit Frequency	Resonator Frequency	Filter Frequency	Anharmonicity	Qubit-Resonator $\chi$	Device Dimensions
4.29 GHz	7.49 GHz	4.56 GHz	246 MHz	5.38 MHz	2.5 mm x 3 mm

Further, the transmission through the readout resonator was also evaluated and is depicted in Figure 4.5. The transmission was simulated to align with the expectations based on the results reported in [18].

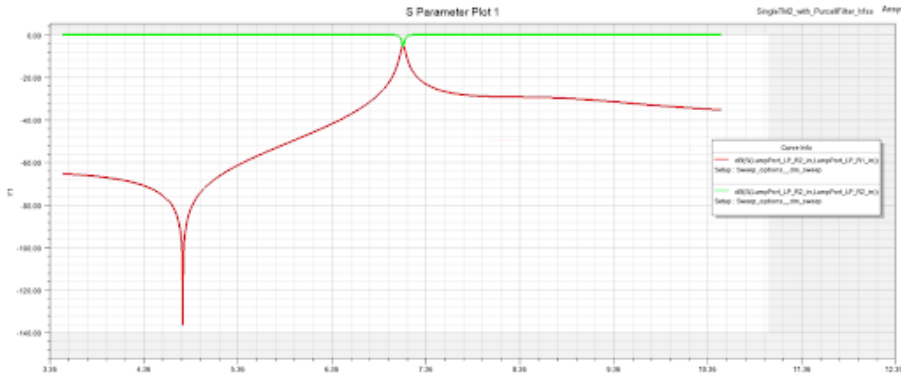


Figure 4.5: Shows the transmission through the readout resonator with the filters incorporated in the design.

To comprehend and characterize the performance of the on-chip filters, various modifications were implemented in the device, as outlined in Table 4.2.

Table 4.2: Device variations in final tapeout to experimentally verify the effects of variation in input-output coupling and incorporation of flux line in the device.

Variation	Purcell Filter	Capacitance (fF)		Flux Line
		$C_{in}$	$C_{in}$	
1	Yes	22.55881	44.20115	No
2	Yes	11.01630	44.20912	No
3	Yes	35.15819	43.68182	No
4	Yes	22.55881	44.20115	Yes
5	No	22.55881	44.20115	Yes

#### 4.1.2 X-mon Qubit with a BandPass Filter

This design focused on compatibility with multiplexed readout for multiple qubits, aiming at scalability of the platform. The inspiration for this design came from the results presented in [19], showcasing its capability for multi-qubit measurement at high speed. The reported filter allows simultaneous measurement of 4 qubits, achieving intrinsic fidelities reaching 99% in less than 200 ns after the start of the measurement pulse.

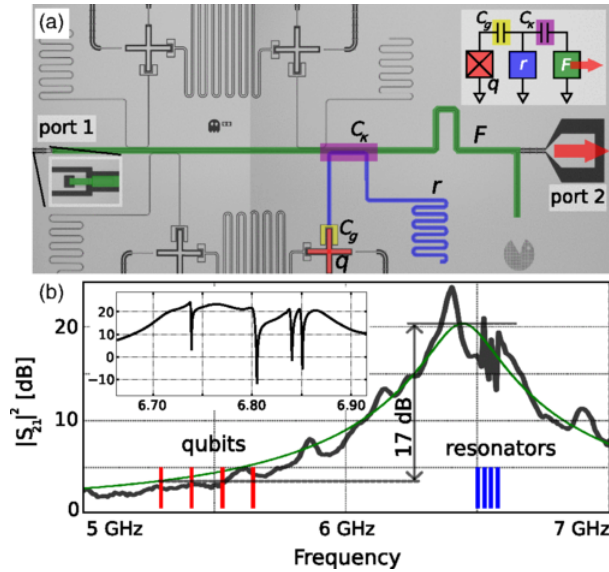


Figure 4.6: Illustrates (a) the device layout and lumped element model and (b) the frequency response of the 4-qubit device designed for high-speed measurements, as presented in [19].

The device layout, as depicted in Figure 4.7 and designed as part of the work presented here, showcases an X-Mon with labeled charge and flux lines. Additionally, it includes a

$\lambda/4$  coupling resonator that couples to the qubit through a claw coupler. This resonator is shunted to ground on one end and capacitively coupled to the filter. The filter, apart from its primary function, also serves as the multiplexed readout bus in the presence of multiple devices (although, in this case, the performance was intended to observe only one qubit).

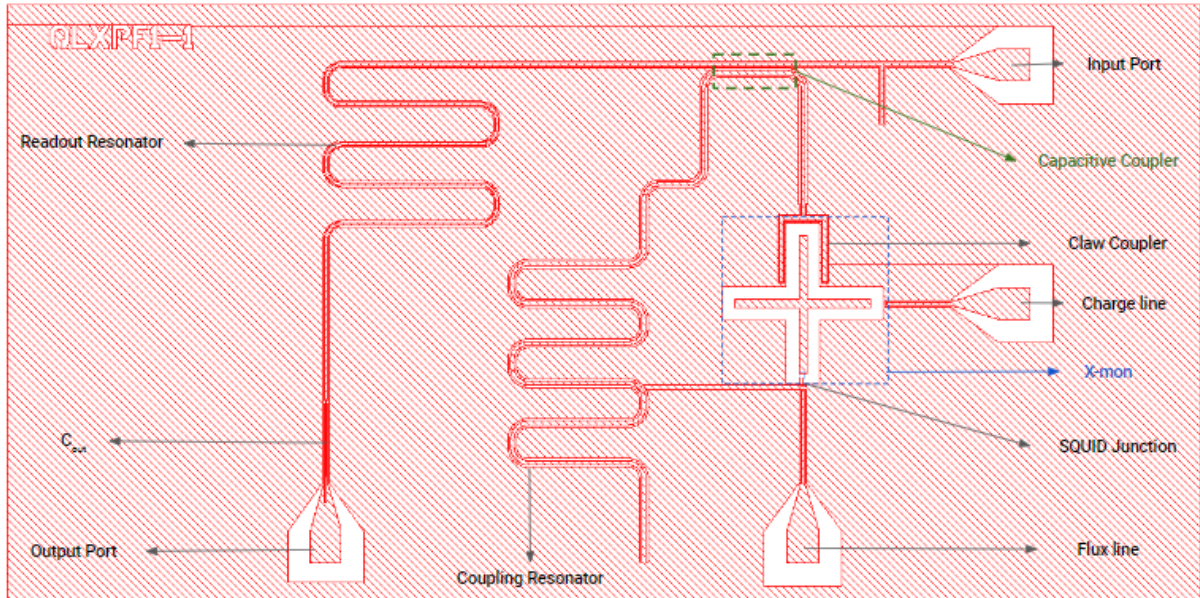


Figure 4.7: The device layout features an X-Mon with a tunable SQUID junction, along with labeled charge and flux lines for qubit control. The coupling resonator utilizes a claw coupler, as indicated in the label, and is capacitively coupled to the filter/readout resonator. The charge and flux lines, along with the readout resonator are impedance-matched to  $50 \Omega$ .

Similar to the device presented in 4.1.1, this device design underwent eigenmode simulations, as presented in Figure 26, for the first three modes to understand the native modes of each device component. Subsequently, qubit parameters were extracted using EPR and LOM analyses, detailed in Table 4.3.

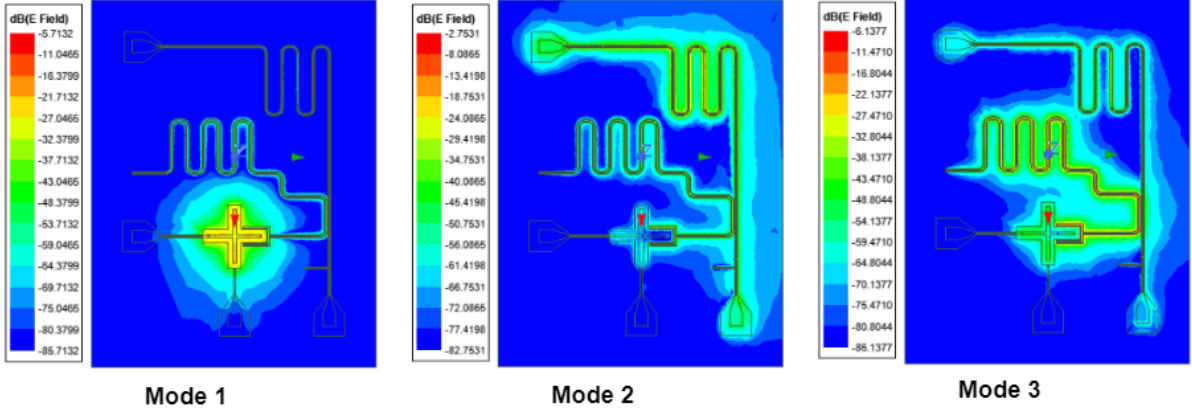


Figure 4.8: The first three eigenmodes for the X-mon qubit and peripheral circuit elements are presented here: Mode 1 at 5.46 GHz, Mode 2 at 6.81 GHz, and Mode 3 at 7.04 GHz.

Table 4.3: Device parameters for X-mon with BandPass Filter extracted using EPR analysis.

Qubit Frequency	Coupling Resonator Frequency	Readout Resonator Frequency	Anharmonicity	Qubit-Resonator $\chi$	Device Dimensions
5.46 GHz	7.04 GHz	6.81 GHz	243 MHz	0.769 MHz	1.5 mm x 3 mm

Transmission analysis was then conducted on the device to comprehend the transmission through the filter. Figure 4.9 reports the S-parameters with the filter incorporated in the design. Various modifications of this design were sent for tapeout to evaluate the performance of the on-chip filters, as outlined in Table 4.4.

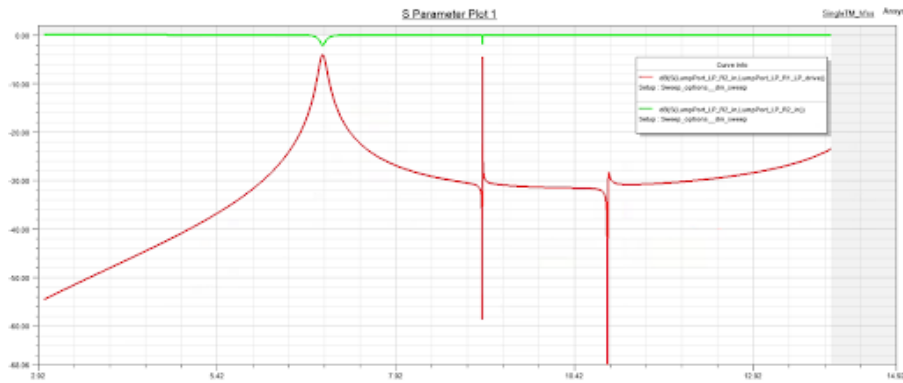


Figure 4.9: Simulation results of transmission parameters through readout resonator of the device.

The mentioned layouts, along with other superconducting devices from the group, were sent to the Institute of Microelectronics (IME) for fabrication on a 12-inch Silicon

Table 4.4: Design variations for the X-mon based qubit devices included in the final tapeout.

<b>Variation</b>	<b>Purcell Filter</b>	<b>Flux Line</b>
1	Yes	No
2	Yes	Yes
3	No	Yes

wafer with superconducting layers made of Aluminum and Manhattan-style Josephson junctions were used as the non-linear inductor for the Transmon qubits. As of writing this thesis, the tapeouts are yet to be fully fabricated, and characterizing them remains a future work for the presented research.

## CHAPTER 5

### High Dimensional Qudit – Trimon

This chapter describes and explores the design and simulation of planar Trimons. Trimons are multi-modal superconducting qubits aimed at high-dimensional quantum computation, first proposed here [20]. A Josephson ring modulator-based device, Trimons can accommodate 3 qubits in one device. The following sections delve into the physics of a 3D Trimon, as discussed in [20, 88], and the subsequent section will elaborate on the work related to planar Trimons, providing simulation results to extract important device parameters.

#### 5.1 3D Trimon

While popular in the superconducting qubit community, Transmons come with certain limitations. This motivates the exploration and work with alternate superconducting devices such as Trimons, a type of multi-modal superconducting device. All modes of Trimons exhibit transmon-like behavior due to all-to-all longitudinal coupling, and Purcell protection dependent on the symmetry of the device. The hybridization of modes allows for easier interaction by introducing asymmetry. Figure 5.1 illustrates a Trimon device, the lumped circuit schematic, and its operation in a 3D cavity.

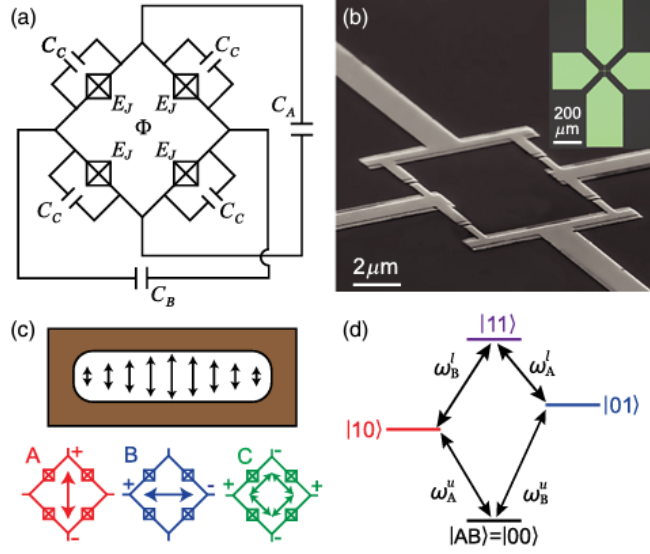


Figure 5.1: Trimon and its operation as described in [20]. (a) Illustrates the circuit model of a Trimon, while (b) shows the Josephson ring modulator structure at the center of the Trimon with four Josephson junctions. Inset: a complete Trimon device. (c) The device is placed in a cavity, and qubit (mode) A of the Trimon couples to the cavity. Qubits (modes) B and C are not coupled to the cavity, providing Purcell Protection. States of qubits B and C are measured using the dispersive shift of A, dependent on the states of B and C. (d) The energy level diagram illustrates the coupled two-qubit subspace involving qubits A and B, while qubit C remains in its ground state. The  $\sigma_z\sigma_z$  coupling results in the transition frequency of each qubit being dependent on the state of the other, enabling the readout of qubits B and C while A couples to the cavity. Image from ref [20]

The system Hamiltonian and dispersive shifts of the Trimon as described in [20] are presented below

$$\frac{1}{\hbar}H_{\text{system}} = -\frac{1}{2}\left[\sum_{i=A,B,C}(\omega_i - 2\beta_i)\sigma_z^i + \sum_{i\neq j}J_{ij}\sigma_z^i\sigma_z^j\right] + \left(\omega_{\text{cav}} - \sum_{i=A,B,C}\chi_i\sigma_z^i\right)a^\dagger a \quad (5.1)$$

$$\chi_A = g_A^2 \left( \frac{1}{\Delta_{A0}} - \frac{1}{\Delta_{A0} - 2J_A} \right) \quad (5.2)$$

$$\chi_B = \frac{g_A^2}{2} \left( \frac{1}{\Delta_{A0}} - \frac{1}{\Delta_{A0} - 2J_{AB}} \right) \quad (5.3)$$

$$\chi_C = \frac{g_A^2}{2} \left( \frac{1}{\Delta_{A0}} - \frac{1}{\Delta_{A0} - 2J_{CA}} \right) \quad (5.4)$$

Additionally, a Transmon device optimized for 3-qubit operations has also been reported in [88], achieving ideal level spacing by operating at a flux bias corresponding to an integer multiple of the flux quantum for the ring and a fractional flux quantum for the small SQUID loops. The key features are the flux tunability with a robust cross-Kerr matrix, symmetry-dependent Purcell protection, and hybridization of modes for easier interaction. The results presented in [88] benchmark the processor by implementing a three-qubit version of various quantum algorithms. These results highlight the advantage of having native three-qubit gates, crucial for improving the performance of larger systems with Trimons as building blocks. They are also proposed to find use in error correction and mitigation, particularly with logical or protected qubits.

Thus, Trimons prove to be suitable devices for exploration in planar and scalable applications. The following section provides detailed insights into the work on Trimons as part of the research conducted for this thesis.

## 5.2 Planar Trimon

The design process for planar Trimons commenced with the modulation of the device to achieve desirable qubit frequencies. In Figure 5.2, a Trimon device is depicted, showcasing modified pad sizes and gap positions, optimizing the qubit frequencies and spacing between them.

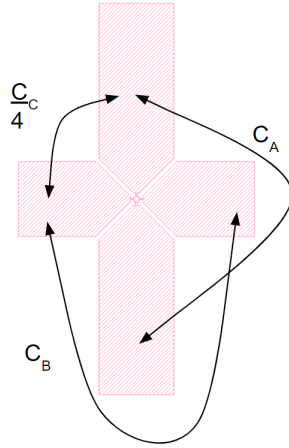


Figure 5.2: Layout of a Trimon device, highlighting the pads and the associated contributions towards the capacitances in the schematic illustrated in Figure 5.1

The effective circuit schematic device remains the same as illustrated in Figure 1. The Trimon was further designed to couple with two  $\lambda/2$  resonators, facilitating coupling to qubit A of the planar Trimon while maintaining resonator frequencies. This coupling mechanism allows interaction with the environment through capacitive coupling to bond pads interfacing with the microwave electronics. The Physics of multimodal quantum circuits is further presented [89], here two planar Trimon devices are presented, each with specific characteristics, and corresponding eigenmode simulation results are presented below. Device parameters were extracted using the EPR method.

The first device presented in Figure 5.3 showcases eigenmode simulations for a planar Trimon coupled to two resonators. The first three modes correspond to Qubits A, B, and C, while Modes 4 and 5 represent the resonator modes. Despite efforts to make the resonators identical, the separation in the eigenmodes observed here is attributed to numerical errors.

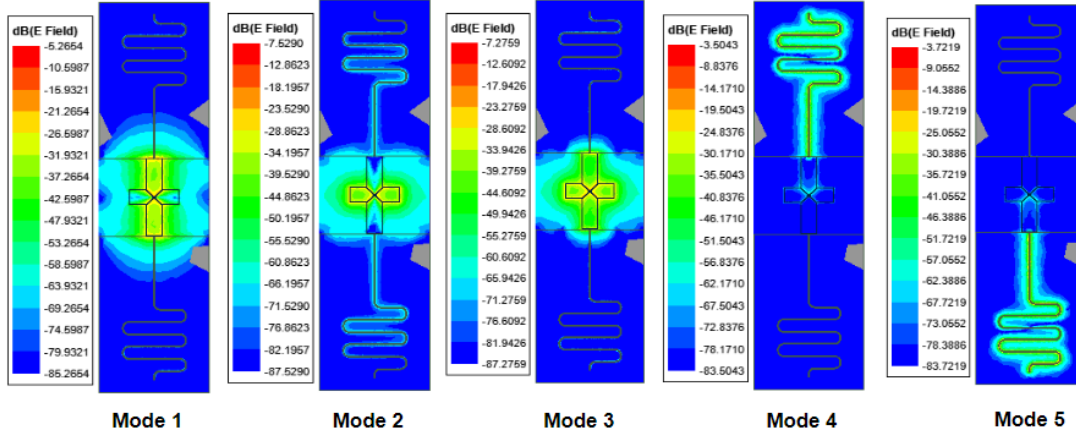


Figure 5.3: Trimon device with 2 resonators coupling to mode A of the device. The frequencies for each qubit mode ( $\omega_q$ ) are identified as  $\omega_A : 5.625$  GHz;  $\omega_B : 7.072$  GHz, and  $\omega_C : 7.971$  GHz. The corresponding anharmonicities extracted from EPR are  $\alpha_A = 48.3$  MHz;  $\alpha_B = 78.7$  MHz, and  $\alpha_C = 99.7$  MHz. Modes 4 ( $\omega_{r1} = 8.897$  GHz) and 5 ( $\omega_{r2} = 8.899$  GHz) were expected at the same frequency, attributed to resonator frequencies, and are hypothesized to be separated due to numerical errors. Here, qubit B can be observed to couple to the resonators, which is undesirable and creates a decoherence channel for Qubit B, in contrast to the 3D Trimons.

The second device, as described in Figure 5.4, builds on the layout presented above and attempts to improve the coupling of the resonator to qubit A. Although improved coupling is observed, coupling of qubits B and C to the resonator can be observed here too.

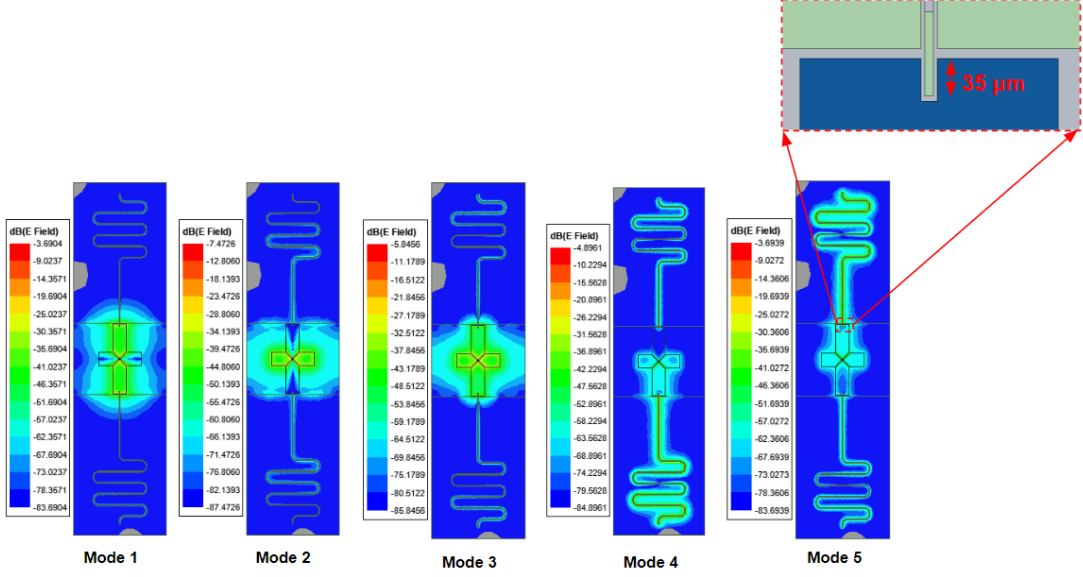


Figure 5.4: Trimon with improved coupling of resonators. The frequencies for each qubit are extracted as  $\omega_A : 5.557$  GHz;  $\omega_B : 7.100$  GHz, and  $\omega_C : 7.984$  GHz. The corresponding anharmonicities are  $\alpha_A = 46.8$  MHz;  $\alpha_B = 79.3$  MHz, and  $\alpha_C = 98.9$  MHz. Modes 4 ( $\omega_{r1} = 8.884$  GHz) and 5 ( $\omega_{r2} = 8.846$  GHz) were expected as the resonator frequencies. Inset: Coupling the resonator to capacitor pads on either side to improve coupling to mode A.

The notable challenges with planar Trimons involved low anharmonicities of the qubits and coupling qubits B and C to the resonators. The coupling of these modes to resonator modes risked creating decoherence channels for these qubits, compromising their Purcell protection. The circuits were developed for symmetrical Trimons, with ongoing efforts aimed at improvements and optimizations to achieve performances comparable to those reported for 3D Trimons. The challenges in incorporating planar Trimons notwithstanding, their demonstrated advantages in 3D cavities warrant further investigation and justify the endeavor to explore a Trimon-based quantum processor in an attempt to scale up the superconducting qubit platforms further.

## CHAPTER 6

### Multi-Planar Qubit Packaging

Integrated circuit packaging is the conclusive phase in the fabrication of any semiconductor device. It plays a crucial role in providing both mechanical support and electrical isolation from the noisy components of the environment while also serving as an essential interface with the rest of the circuit efficiently.

A microwave package for any superconducting qubit device serves multiple functions:

1. Creates an interface between the microscopic qubit chips and the control equipment.
2. It provides the mechanical stability of qubit chips within the dilution refrigerator.
3. The package acts as a shield, protecting the enclosed qubit chip from external radiation and stray magnetic fields.
4. It is equipped to provide impedance-matched inputs and outputs, ensuring efficient signal transmission.
5. The design minimizes crosstalk in communication channels.
6. The package establishes a thermal link to the dilution refrigerator for effective cooling.

Microwave packaging can be divided into two parts for a better understanding of constraints and package design: the platform of the qubit and the shielding of the qubit. Each has specific constraints and design requirements. The following section looks into various proposed and existing structural architectures for superconducting qubit packaging, while the subsequent sections of this chapter will delve into detailed design constraints,

considerations, and results for the microwave package designed for the devices described in this thesis.

## 6.1 Existing Architecture

Various packaging ideas have been proposed for qubit designs. One prominent approach in academia is the use of 3D architectures, as illustrated in Figure 4.1. In this design, the cavity serves as both the package and the environment for the qubit devices. The qubits couple to microwave tones sent to the cavity through SMA cables to ports and eventually to coupling pins. However, there are also reported designs specifically proposed for planar superconducting qubits.

For planar qubit devices, packaging of the devices can be performed through two methods. The first involves flip-chip bonding, where the chips are bonded to an interposer using indium bumps. The interposer then connects to a PCB, which interfaces with macroscopic traces and lines linked to control electronics. While flip-chip bonding is efficient and widely used in industry, its incorporation in an academic setup poses challenges due to the availability of tools to perform flip-chip bonding. As a result, the second choice has gained popularity in academic settings. In this approach, a chip is directly placed on a PCB and wire-bonded to it to interface with control instruments. This method is easier to implement in an academic setup due to accessibility to mature PCB manufacturing techniques for RF applications and the availability of wire bonding tools. Figure 6.1 illustrates the different packaging techniques reported in the published literature. It is essential to note that in both cases, shielding is essential to protect the devices from stray electric and magnetic fields and provide mechanical support for mounting inside a dilution fridge.

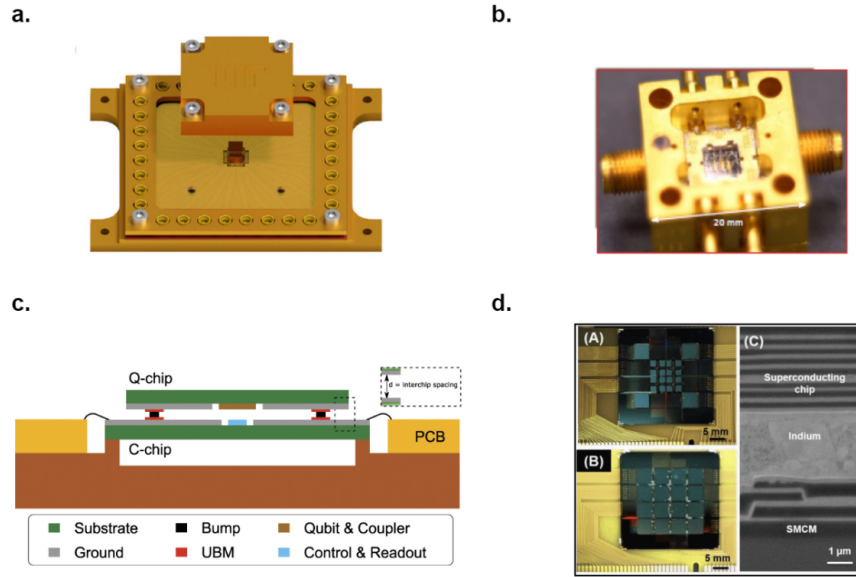


Figure 6.1: Illustration of various packaging methods for superconducting qubit processors presented in published literature. Images (a) from ref [21] and (b) from ref [22] © (2021 IEEE, Reprinted, with permission), respectively, showcase examples of chips directly mounted on a PCB and wirebonded to associated tracks for interfacing with control electronics, with a metal shield protecting the superconducting chips from external electric and magnetic fields during operation. Careful design of the PCB for RF and cryogenic applications is essential, and it is easier to implement, as all the techniques used are easily accessible to users, even in an academic setup. Images (c) ref [23] and (d) [24] © (2018 IEEE, Reprinted, with permission) present a proposal for flip-chip bonding of an integrated superconducting processor, along with fabricated results of flip-chip bonding performed on superconducting qubit devices.

## 6.2 Current Designs

The qubit packaging topology reported here involves wire-bonding the chips to a PCB designed for RF application in cryogenic environments. It was also ensured to provide sufficient shielding from stray fields and adequate mechanical support for mounting the platform inside the dilution refrigerator. The packaging design occurs in two stages: one for a 2-qubit device package and another for an 8-qubit device package. These microwave packages incorporate necessary control and readout lines, with only the 8-qubit package supporting an additional flux bias line to all the devices. Due to the limited time frame for reporting the results and extended turnaround times for PCB and shield fabrication,

only the 2-qubit package was fabricated and characterized. The design and simulations for the 8-qubit package are presented in the later subsection.

### **6.2.1 Packaging 2 Qubit Devices**

This microwave package was specifically designed to accommodate two single-qubit devices developed as part of the superconducting qubit tapeout undertaken by the group. It has the capability to handle 4 RF channels utilized for readouts and charge lines. The design incorporates a multi-layer architecture to minimize crosstalk and efficiently accommodate supporting elements. Additionally, embedded coplanar waveguides were employed to enable high field strength and strong coupling to both Qubit and Qudit devices discussed in the prior chapters.

#### **6.2.1.1 Design Considerations**

The design of the microwave package discussed here is divided into two main components: the PCB platform and microwave shielding, each with its own set of design considerations, from material choices to physical design.

Starting with the PCB, it serves as the immediate platform for placing the superconducting qubits. The first step in designing any RF PCB for critical applications is understanding system requirements and selecting an ideal dielectric layer stack-up. The layout should prevent parasitic stub resonances and crosstalk, ensuring impedance matching, low insertion losses, and improved signal integrity. The chosen stack-up involved burying signal layers within the stack using embedded guidelines, isolating them between ground planes to minimize exposure to the external environment. Two materials, Rogers 4350B and Megatron 6, were selected for their low dissipating factors and compatibility with cryogenic environments. Figure 6.2 details the chosen stack-up for performance comparison.

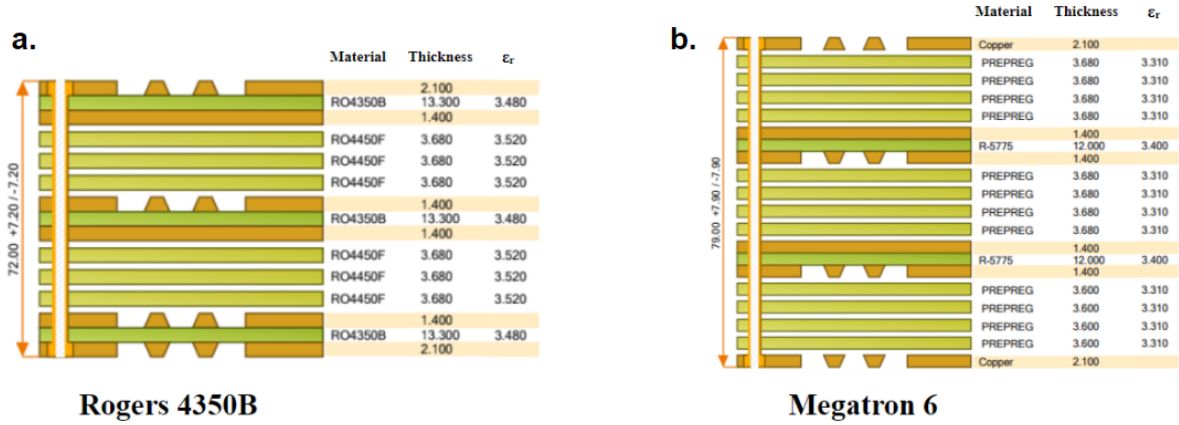


Figure 6.2: The figure presents the comprehensive stack-ups, featuring copper layers (depicted in gold) for signal layers and ground planes, along with Rogers/Megatron 6 (in green) as the core dielectric and prepreg layers (in light-green). Rogers was selected for its favorable properties:  $\epsilon_r$  (dielectric constant) of 3.48, dissipation factor of 0.0037, and a Z-axis coefficient of thermal expansion of 32 ppm/°C. On the other hand, Megatron 6 offers  $\epsilon_r$  of 3.4, a dissipation factor of 0.004, and a Z-axis coefficient of thermal expansion of 45 ppm/°C. Both stack-ups are well-suited for cryogenic applications.

Considering that qubits can spontaneously couple to undesirable package modes, suppressing these modes becomes crucial. Eigenmode simulations were conducted to identify PCB-based modes in the operating frequency range, and shielding vias strategically added on the board were found to fend off-resonant modes that could affect the placed chip. Figure 6.3 illustrates the effects of shielding vias in eliminating the effects of resonating modes in the qubit chip placed at the center of the PCB.

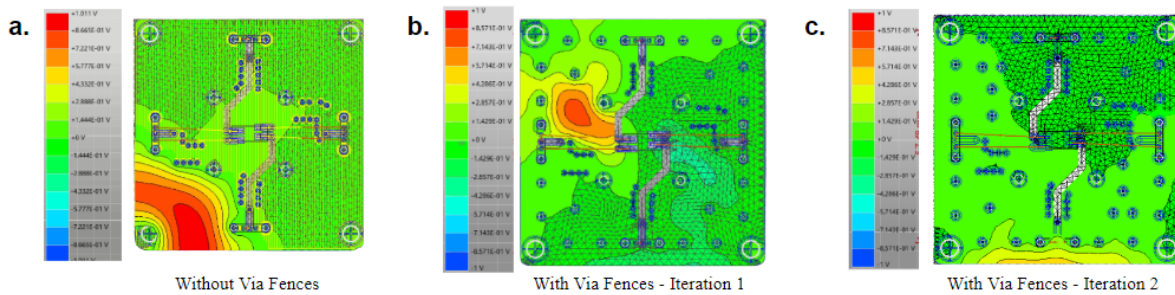


Figure 6.3: Eigenmode simulations using SIwave for the PCB stack-ups revealed certain PCB-based eigenmodes within the operational frequency range. To mitigate any potential impact on the qubits, strategic positioning of shielding vias was implemented, aiming to avoid modes near the chip that could potentially introduce a package-based dephasing channel for the qubits.

The choice of epoxy for chip attachment was also critical, and a silver-based epoxy was selected based on reported performances. [90]

After meticulously considering the PCB requirements, the focus shifted to the design of the metal enclosure or microwave shielding. This crucial component addressed concerns related to material-dependent losses of magnetic, conductive, or dielectric origin. Given that tunable qubits/qubits are sensitive to magnetic fields, the choice of material was paramount. Copper, known for its higher thermal conductivity and lower dielectric losses compared to Aluminum, was selected for the shielding body. An additional layer of Aluminum was applied to the top enclosure (as shown in Figure 6.4) to protect the chips from stray magnetic fields inside the dilution fridge, leveraging the Meissner effect at the operating temperature of  $\sim 15mK$ .

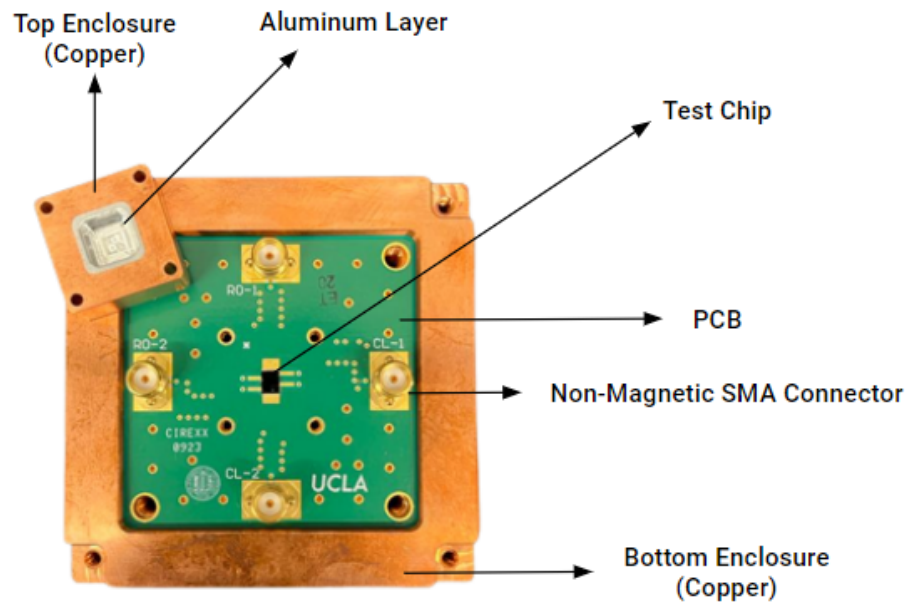


Figure 6.4: Microwave packaging including PCB and a test chip. The bottom enclosure accommodates the PCB and is directly attached to the mounting plate of the dilution refrigerator. Constructed from copper, the bottom enclosure is chosen owing to the thermal conductivity and lower dielectric losses. The top enclosure serves the purpose of shielding the chip from external radiation. It contains an outer shield made of copper, while it incorporates a 1 mm thick layer of aluminum to protect the chip from stray magnetic fields in the surrounding environment. Non-magnetic SMA contact connectors are used to interface with SMA cables within the dilution refrigerator.

While [21] suggests that an aluminum-evaporated cover might be a superior material choice, copper was chosen due to its easier fabrication availability. The comparative analysis of using aluminum-evaporated copper as the metal enclosure material remains a potential area for future exploration.

Another critical consideration involved avoiding undesirable coupling of qubits to package modes by eliminating box modes < 10 GHz. Box modes can be evaluated by the expression 6.1 Eigenmode simulations, depicted in Figure 6.5, revealed that the box modes commenced at 25.11 GHz, significantly exceeding the set threshold of 10 GHz.

$$f_{ijk} = \frac{c}{2\pi\sqrt{\mu_r\epsilon_r}} \sqrt{\left(\frac{i\pi}{x}\right)^2 + \left(\frac{j\pi}{y}\right)^2 + \left(\frac{k\pi}{z}\right)^2} \quad (6.1)$$

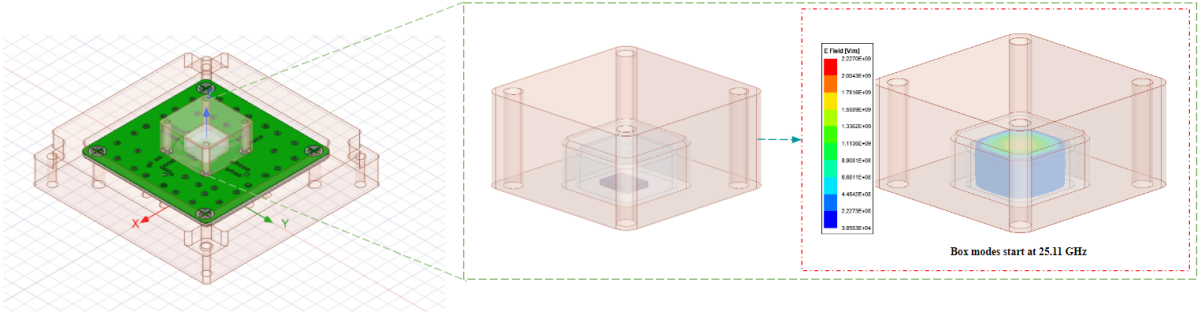


Figure 6.5: Eigenmode simulations on ANSYS HFSS report the box modes to start from 25.11 GHz. The calculations are in agreement with the expression 6.1

The subsequent section delves into the performance and challenges associated with the current design.

### 6.2.1.2 Performance

The integrated microwave package (Figure 6.6) underwent evaluation for performance with a test chip positioned within the package and wirebonded using aluminum wires (diameter 25  $\mu\text{m}$ ) secured with silver-based epoxy, as described in Subsection 6.2.

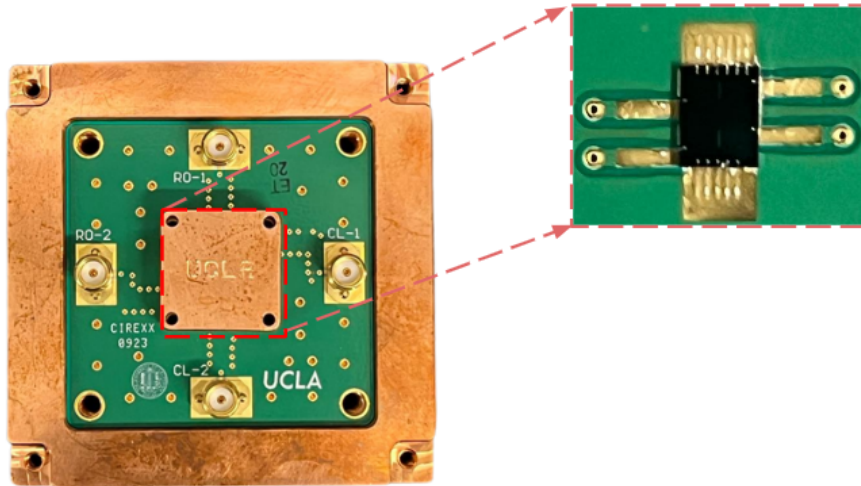


Figure 6.6: Assembled microwave package. Inset: Wirebonded test chip.

The essential performance features, as depicted in Figure 6.7, were characterized, focusing on transmission and crosstalk in RF tracks on the same and different layers to assess the impact of employing a multilayer architecture for the PCB. While the transmissions were characterized for the range of 1 GHz to 10 GHz, the targeted operating frequency for this design was 4.5 GHz to 7.5 GHz. Regarding crosstalk, an observable increase was noted as the frequency increased. However, transitioning from the nearest neighbor to other tracks on the same layer and different layers resulted in a respective decrease of 10 dB in crosstalk. This trend favors the use of a multilayer architecture for the PCB.

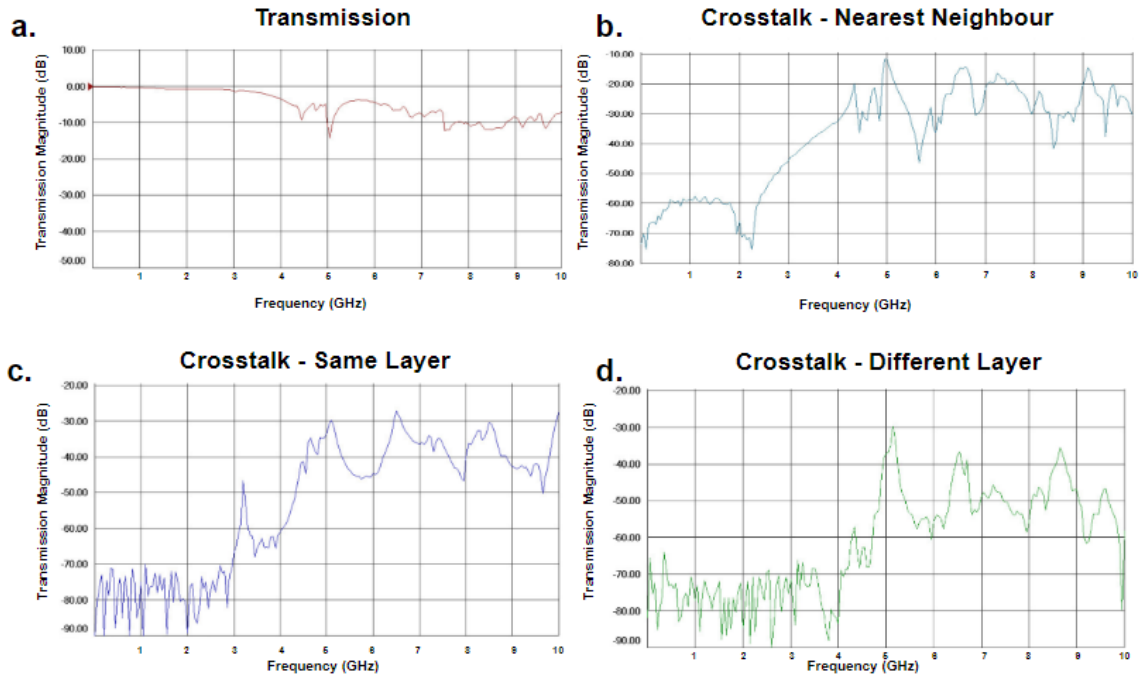


Figure 6.7: Transmission and crosstalk performance characterization of the microwave package was conducted in the frequency range of 1 GHz to 10 GHz. All these experiments were performed at room temperature.

While testing for any potential degradation of the PCBs in a cryogenic environment, both the Rogers and Megatron6 PCBs were placed inside a dilution fridge for a month. Subsequently, their performance was characterized and compared with those that were not subjected to the cryogenic environment. No degradation in the physical quality and performance of the PCBs was not observed to degrade over time.

Although there is room for improvement in the transmission and crosstalk results, they align with the primary expectations. Figure 6.8 illustrates the  $S_{11}$  characterization of the Megatron6 PCB to identify unwanted modes, which are labeled on the figure. While the exact source of these modes cannot be definitively stated, it is hypothesized to be either a PCB-based mode or a result of impedance mismatch at the SMA contact connector end.

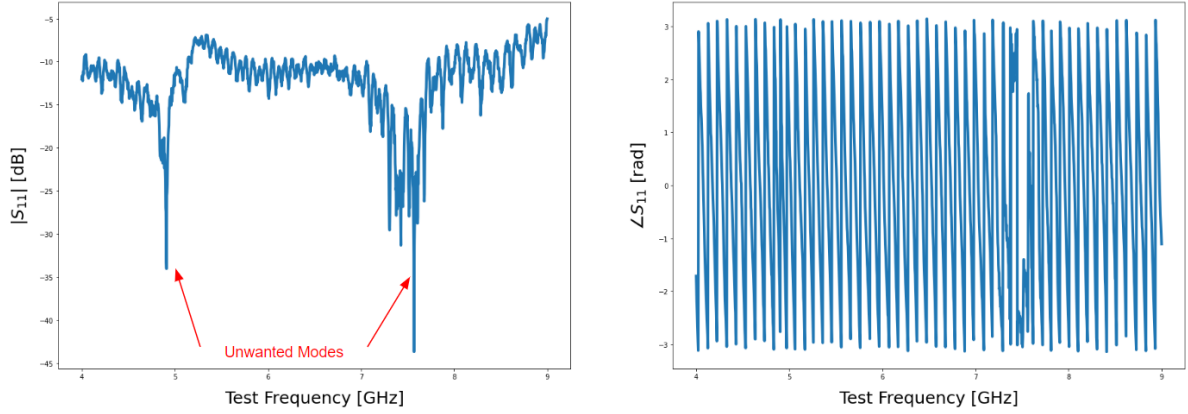


Figure 6.8: Measurements using the Megatron6 PCB exhibited unwanted frequency modes, as indicated in repeated experiments.

Future iterations aim to build upon the current results and enhance performance by eliminating any unwanted package modes within the operating frequency range.

### 6.2.2 Packaging 8 Qubit Devices

A scaled-up microwave package design, intended to accommodate eight qubit devices, was also developed and presented here. This scaled-up packaging follows a similar layer stack-up approach using Rogers 4350B as illustrated in figure 6.2. The key features of this design include an 8-layer configuration with 16 RF channels and 1 DC channel. The DC channel is specifically included to accommodate flux lines in the design. The multi-layer stripline architecture is employed to minimize crosstalk and has the capability to incorporate passive RF filters. In this design, stripline waveguides are used instead of embedded coplanar waveguides on the two-qubit platforms due to the compact structure and longer path length of tracks near the qubit. The dimensions of the PCB were chosen considering the mounting board dimensions inside the dilution refrigerator. The traces are matched for propagation delays, and Figure 6.10 illustrates the layout for the PCB that houses 16 RF channels and a DC channel for flux biasing the qubits.

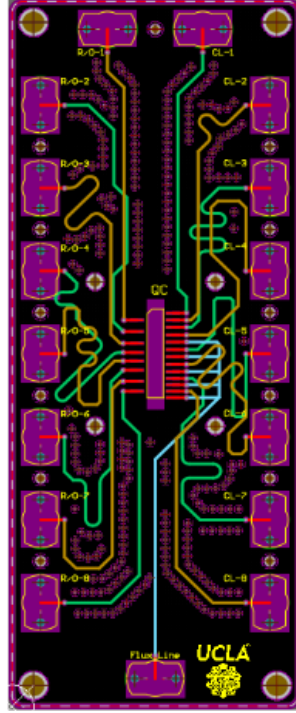


Figure 6.9: PCB layout (all layers), designed to package 8 qubit devices. This specific PCB configuration supports 16 RF channels and includes 1 DC channel designed to function as a flux line for tunable qubits. In the layout, the green and orange tracks represent RF channels on different layers, while the blue track indicates the DC flux line.

An analysis of near-end crosstalk was performed to address potential concerns with the compact architecture, as presented in Figure 43. Near-end crosstalk, described by the term  $K_{NEXT}$  and defined by Equation 6.2, can be critical for delicate devices such as superconducting qubits on a chip.

$$K_{NEXT} = \frac{1}{2} \frac{1}{\sqrt{L_{11}C_{11}} + \sqrt{L_{22}C_{22}}} \left( \frac{L_{21}}{Z_1} - Z_2 C_{21} \right) \quad (6.2)$$

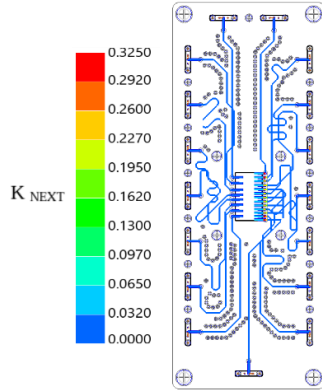


Figure 6.10: Analysis of near-end crosstalk performed using SIwave. It indicates that cross-layer crosstalk is negligible. However, higher crosstalk is observed in the charge lines that are closely packed on the right side of the chip footprint.

A scaled-up metal enclosure was also designed to house the PCB mentioned above, and associated box modes were evaluated. The box modes in this design start at a lower frequency than the previous design, aligning with expectations (set by 6.1). However, they still exceed the desired limit of 10 GHz.

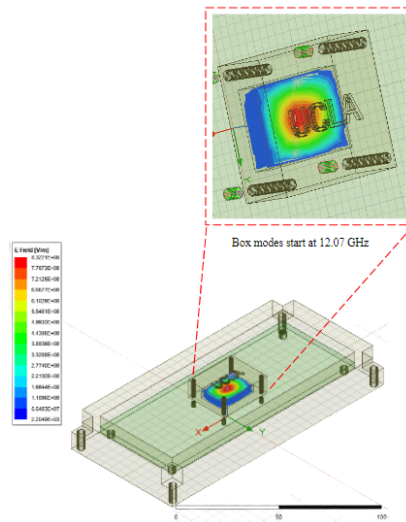


Figure 6.11: Box modes were evaluated using ANSYS HFSS and were observed to start at 12.07 GHz

Further iterations aim to refine and optimize the design while taking feedback from the two-qubit package results to meet the desired specifications.

# CHAPTER 7

## Conclusion

### 7.1 Summary

Superconducting qubit devices have emerged as the most popular architecture for quantum computation in both academia and industry. The work presented in this thesis focuses on exploring the overall scalability of these platforms, particularly in the NISQ regime where quantum computers currently operate.

Chapter 4 delves into planar qubit platforms designed for scalability, incorporating integrated Purcell filters. These filters not only enhance the quality of readouts but also contribute to scaling the devices for a higher number of qubits.

In Chapter 5, novel superconducting devices like planar Transmons are discussed, targeting high-dimensional quantum computing.

Chapter 6 addresses the packaging of these devices, considering the complexities of fabrication and packaging in the industry. The goal is to develop a platform suitable for packaging current and future superconducting devices, recognizing the limited resources available in an academic setup.

The pursuit of progress in engineering and scientific fields is continuous, and as such, identified areas for improvement and future work are outlined in Sections 7.2 and 7.3 respectively.

## 7.2 Scope of Improvement

As documented earlier, there are identified sections of the work where there is scope for improvement that would contribute to refining the work presented in this thesis.

In Chapter 4, proper characterization of planar qubits remains a potential area for future work. Scaling up the devices for a higher number of qubits and optimizing their coupling also stands out as a derivative of future work.

Regarding Trimon devices presented in Chapter 5, while they represent a novel structure, efficient designs are still a focus for preventing the coupling of modes B and C to the resonator, ensuring they remain as Purcell-protected. Another area of future work involves scaling up the platform with two Trimons coupled to each other using a bus resonator, a concept proposed in [91] but yet to be achieved in a planar regime.

Finally, for packaging qubit and qubit devices presented in Chapter 6, further suppression of unwanted modes and comprehensive measurement of a qubit on the platform are necessary for a complete characterization before further scaling. Additionally, once the desired efficiency is attained, a similar iterative cycle for the scaled-up version presented in Section remains a prospect for future work.

## 7.3 Outlook

With the recent progress in quantum computing, the goal of achieving a full-scale quantum computer appears within reach. There is already a better understanding of harnessing quantum phenomena and controlling different platforms, which has developed over the years. Although scaling presents challenges, it has been relatively rapid in recent years, and various groups are actively addressing the engineering challenges, some of which are documented in this thesis. As we continue to navigate the path towards a fully error-corrected quantum computer, the unwavering interest of the scientific community and the significant strides witnessed thus far instill hope that a system with the desired efficiency is on the horizon.

# APPENDIX A

## Fabrication of Test Chips

The purpose of this section is to detail the fabrication process for the resonator-based test chips used to evaluate the qubit package discussed in Chapter 6. The layout of the test chips is illustrated in Figure A.1.

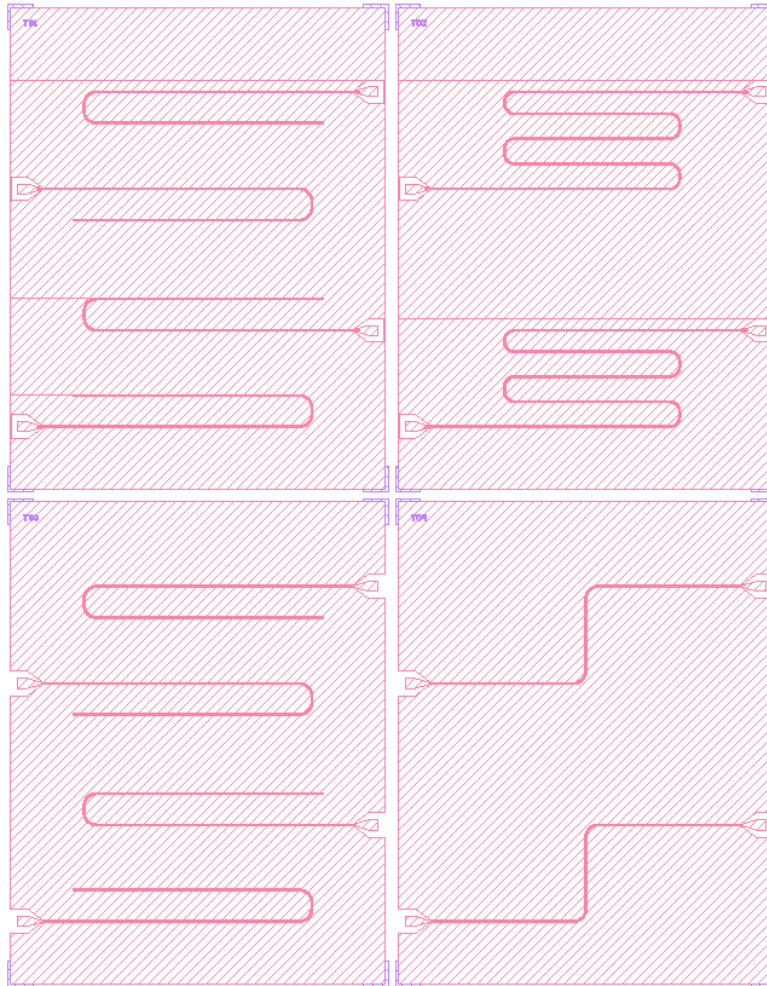


Figure A.1: Layout of the test chips. Test chips TC1 to TC4 feature distinct layouts of coplanar waveguides.

## 1. Wafer Preparation:

- (a) Clean the wafers using a sequence of solvents: Acetone, Methanol, and Isopropyl Alcohol (IPA).
  - i. Acetone removes organic impurities and oily contaminants.
  - ii. Methanol dissolves acetone residues without rapid evaporation.
  - iii. IPA serves as a rinse agent for methanol and residual acetone.
- (b) Use N<sub>2</sub> to blow dry the wafer.
- (c) Dehydrate at 120° C for 120 seconds.

## 2. HMDS Coating:

- Keep samples in the HMDS chamber for 60 seconds.

## 3. Photoresist (PR) Coating:

- NLOF2020 (negative resist) was used.
- Coat the wafer with resist before spinning.
- Use the Headway spinner with the following steps:
  - (a) 500 rpm speed for 5 seconds to ramp up (20000 rpm/sec).
  - (b) 3000 rpm speed for 8 seconds to ramp up (20000 rpm/sec).
  - (c) 500 rpm speed for 5 seconds to ramp down (20000 rpm/sec).
  - (d) 0 rpm speed for 5 seconds to ramp down (10000 rpm/sec).
- Soft bake at 110° C for 60 seconds.

## 4. Exposure:

- Use Karl Suss Contact aligners for exposure.
- Power: 8W, Time: 7.5s, Contact: Vacuum Contact.
- Post-expose bake at 110° C for 40 seconds.

## 5. Development and Cleaning:

- Develop using AZ 300MIF developer for 100 seconds.
- Clean the wafer with water and blow dry with N<sub>2</sub>.

#### 6. Descum Process:

- Use Matrix Asher for 60 seconds at 50° C.
- Power: 100W.

#### 7. Metal Deposition:

- Utilize e-beam evaporator (CHA Mark 40) to deposit 100 nm of Aluminum.

#### 8. Lift-Off Process:

- Perform lift-off using NMP for 60 minutes at 80° C.

#### 9. Challenges and Optimization:

- The main challenge encountered in the fabrication process was proper formation of finger capacitor region at the bonding pads, as illustrated in Figure A.2.

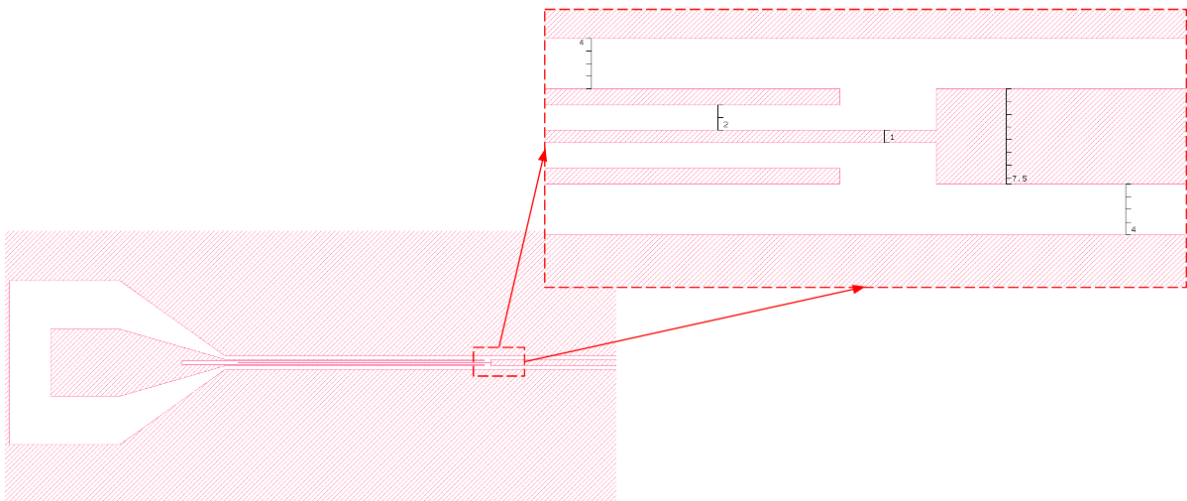


Figure A.2: Bonding pad with finger capacitor. Inset: Zoomed-in image of the figure capacitor with critical dimensions (units  $\mu\text{m}$ ).

- By employing vacuum contact on the Karl Suss contact aligner and optimizing the liftoff process, the fabrication of the resonator was achieved as intended.

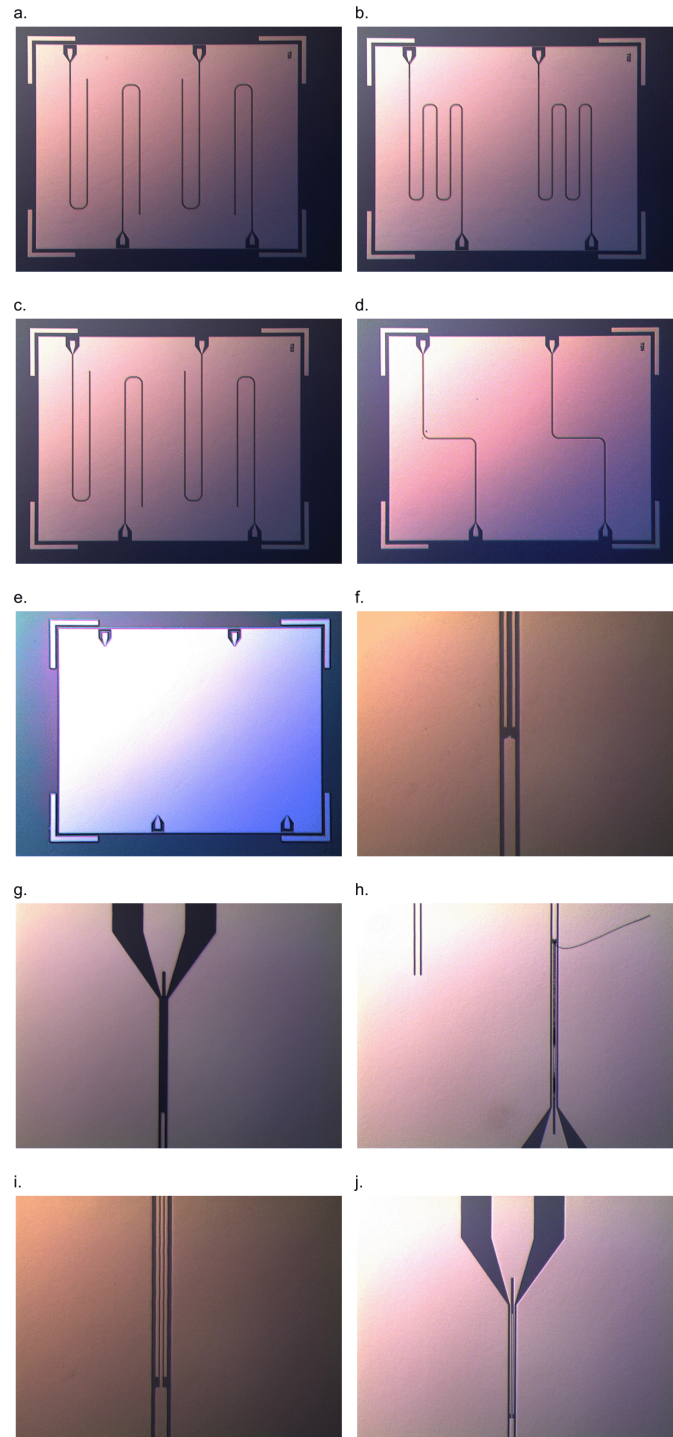


Figure A.3: Fabrication result and challenges. a-d. present successful outcomes for chips TC1-TC4, respectively. e-h. highlight various challenges. e. depicts the result of overexposure of the pattern. f. and g. display cases where the finger capacitor, as presented in Figure A.2, did not form when hard contact was used on the contact aligner instead of vacuum contact. h. represents a case where the properly exposed and developed finger capacitor region was damaged during an improper liftoff process. i. and j. exhibit instances where the results show proper formation of the finger capacitors using the reported recipe.

## REFERENCES

- [1] Farzan Jazaeri, Arnout Beckers, Armin Tajalli, and Jean-Michel Sallese. A review on quantum computing: Qubits, cryogenic electronics and cryogenic mosfet physics, 2019. URL <https://arxiv.org/abs/1908.02656>. vii, 4
- [2] Garrelt J N Alberts, M Adriaan Rol, Thorsten Last, Benno W Broer, Cornelis C Bultink, Matthijs S C Rijlaarsdam, and Amber E Van Hauwermeiren. Accelerating quantum computer developments. *EPJ Quantum Technology*, 8(1):18, July 2021. vii, 6
- [3] S.E. Rasmussen, K.S. Christensen, S.P. Pedersen, L.B. Kristensen, T. Bækkegaard, N.J.S. Loft, and N.T. Zinner. Superconducting circuit companion—an introduction with worked examples. *PRX Quantum*, 2:040204, Dec 2021. doi: 10.1103/PRXQuantum.2.040204. URL <https://link.aps.org/doi/10.1103/PRXQuantum.2.040204>. vii, 7
- [4] Marco De Michielis, Elena Ferraro, Enrico Prati, Louis Hutin, Benoit Bertrand, Edoardo Charbon, David J Ibberson, and Miguel Fernando Gonzalez-Zalba. Silicon spin qubits from laboratory to industry. *Journal of Physics D: Applied Physics*, 56(36):363001, 2023. vii, 8
- [5] Colin D. Bruzewicz, John Chiaverini, Robert McConnell, and Jeremy M. Sage. Trapped-ion quantum computing: Progress and challenges. *Applied Physics Reviews*, 6(2):021314, 05 2019. ISSN 1931-9401. doi: 10.1063/1.5088164. URL <https://doi.org/10.1063/1.5088164>. viii, 9
- [6] P. Krantz, M. Kjaergaard, F. Yan, T. P. Orlando, S. Gustavsson, and W. D. Oliver. A quantum engineer’s guide to superconducting qubits. *Applied Physics Reviews*, 6(2):021318, 06 2019. ISSN 1931-9401. doi: 10.1063/1.5089550. URL <https://doi.org/10.1063/1.5089550>. viii, 17, 19
- [7] Antonio Vettoliere, Paolo Silvestrini, and Carmine Granata. 3 - superconducting quantum magnetic sensing. In Mohamed Henini and Marcelo Oliveira Rodrigues, editors, *Quantum Materials, Devices, and Applications*, pages 43–85. Elsevier, 2023. ISBN 978-0-12-820566-2. doi: <https://doi.org/10.1016/B978-0-12-820566-2.00001-6>. URL <https://www.sciencedirect.com/science/article/pii/B9780128205662000016>. viii, 22
- [8] J Q You and Franco Nori. Atomic physics and quantum optics using superconducting circuits. *Nature*, 474(7353):589–597, June 2011. viii, 23
- [9] Jens Koch, Terri M. Yu, Jay Gambetta, A. A. Houck, D. I. Schuster, J. Majer, Alexandre Blais, M. H. Devoret, S. M. Girvin, and R. J. Schoelkopf. Charge-insensitive qubit design derived from the cooper pair box. *Phys. Rev. A*, 76:042319, Oct 2007. doi: 10.1103/PhysRevA.76.042319. URL <https://link.aps.org/doi/10.1103/PhysRevA.76.042319>. viii, 24

- [10] Alexander P M Place, Lila V H Rodgers, Pranav Mundada, Basil M Smitham, Mattias Fitzpatrick, Zhaoqi Leng, Anjali Premkumar, Jacob Bryon, Andrei Vrajitoarea, Sara Sussman, Guangming Cheng, Trisha Madhavan, Harshvardhan K Babla, Xuan Hoang Le, Youqi Gang, Berthold Jäck, András Gyenis, Nan Yao, Robert J Cava, Nathalie P de Leon, and Andrew A Houck. New material platform for superconducting transmon qubits with coherence times exceeding 0.3 milliseconds. *Nature Communications*, 12(1):1779, March 2021. ix, 25
- [11] Eric Hyypä, Suman Kundu, Chun Fai Chan, András Gunyhó, Juho Hotari, David Janzso, Kristinn Juliusson, Olavi Kiuru, Janne Kotilahti, Alessandro Landra, Wei Liu, Fabian Marxer, Akseli Mäkinen, Jean-Luc Orgiazzi, Mario Palma, Mykhailo Savytskyi, Francesca Tosto, Jani Tuorila, Vasili Vadimov, Tianyi Li, Caspar Ockeloen-Korppi, Johannes Heinsoo, Kuan Yen Tan, Juha Hassel, and Mikko Möttönen. Unimon qubit. *Nature Communications*, 13(1):6895, November 2022. ix, 26
- [12] Yvonne Y. Gao, M. Adriaan Rol, Steven Touzard, and Chen Wang. Practical guide for building superconducting quantum devices. *PRX Quantum*, 2:040202, Nov 2021. doi: 10.1103/PRXQuantum.2.040202. URL <https://link.aps.org/doi/10.1103/PRXQuantum.2.040202>. ix, 17, 27, 28, 29, 31
- [13] Zlatko K Minev, Thomas G McConkey, Maika Takita, Antonio D Corcoles, and Jay M Gambetta. Circuit quantum electrodynamics (cqed) with modular quasi-lumped models. *arXiv preprint arXiv:2103.10344*, 2021. x, 34, 35
- [14] Zlatko K Minev, Zaki Leghtas, Shantanu O Mundhada, Lysander Christakis, Ioan M Pop, and Michel H Devoret. Energy-participation quantization of josephson circuits. *npj Quantum Information*, 7(1):131, August 2021. x, 35, 36, 38
- [15] Bbn Raytheon. *Wide-Band Josephson Parametric Amplifier Operating Guide TM-2035 Application Note*. xi, 41
- [16] Kirill G. Fedorov Philipp Kruger. The josephson parametric amplifier, 2021. xi, 42, 44
- [17] Hanhee Paik, D. I. Schuster, Lev S. Bishop, G. Kirchmair, G. Catelani, A. P. Sears, B. R. Johnson, M. J. Reagor, L. Frunzio, L. I. Glazman, S. M. Girvin, M. H. Devoret, and R. J. Schoelkopf. Observation of high coherence in josephson junction qubits measured in a three-dimensional circuit qed architecture. *Phys. Rev. Lett.*, 107:240501, Dec 2011. doi: 10.1103/PhysRevLett.107.240501. URL <https://link.aps.org/doi/10.1103/PhysRevLett.107.240501>. xii, 47
- [18] M. D. Reed, B. R. Johnson, A. A. Houck, L. DiCarlo, J. M. Chow, D. I. Schuster, L. Frunzio, and R. J. Schoelkopf. Fast reset and suppressing spontaneous emission of a superconducting qubit. *Applied Physics Letters*, 96(20):203110, 05 2010. ISSN 0003-6951. doi: 10.1063/1.3435463. URL <https://doi.org/10.1063/1.3435463>. xii, 49, 50, 51

- [19] Evan Jeffrey, Daniel Sank, J. Y. Mutus, T. C. White, J. Kelly, R. Barends, Y. Chen, Z. Chen, B. Chiaro, A. Dunsworth, A. Megrant, P. J. J. O’Malley, C. Neill, P. Roushan, A. Vainsencher, J. Wenner, A. N. Cleland, and John M. Martinis. Fast accurate state measurement with superconducting qubits. *Phys. Rev. Lett.*, 112:190504, May 2014. doi: 10.1103/PhysRevLett.112.190504. URL <https://link.aps.org/doi/10.1103/PhysRevLett.112.190504>. xii, 52
- [20] Tanay Roy, Suman Kundu, Madhavi Chand, Sumeru Hazra, N. Nehra, R. Cosmic, A. Ranadive, Meghan P. Patankar, Kedar Damle, and R. Vijay. Implementation of pairwise longitudinal coupling in a three-qubit superconducting circuit. *Phys. Rev. Appl.*, 7:054025, May 2017. doi: 10.1103/PhysRevApplied.7.054025. URL <https://link.aps.org/doi/10.1103/PhysRevApplied.7.054025>. xiii, 56, 57
- [21] Sihao Huang, Benjamin Lienhard, Greg Calusine, Antti Vepsäläinen, Jochen Braumüller, David K. Kim, Alexander J. Melville, Bethany M. Niedzielski, Jonilyn L. Yoder, Bharath Kannan, Terry P. Orlando, Simon Gustavsson, and William D. Oliver. Microwave package design for superconducting quantum processors. *PRX Quantum*, 2:020306, Apr 2021. doi: 10.1103/PRXQuantum.2.020306. URL <https://link.aps.org/doi/10.1103/PRXQuantum.2.020306>. xiv, 64, 68
- [22] Benjamin Lienhard, Jochen Braumüller, Wayne Woods, Danna Rosenberg, Greg Calusine, Steven Weber, Antti Vepsäläinen, Kevin O’Brien, Terry P. Orlando, Simon Gustavsson, and William D. Oliver. Microwave packaging for superconducting qubits. In *2019 IEEE MTT-S International Microwave Symposium (IMS)*, pages 275–278, 2019. doi: 10.1109/MWSYM.2019.8701119. xiv, 64
- [23] Sandoko Kosen, Hang-Xi Li, Marcus Rommel, Daryoush Shiri, Christopher Warren, Leif Grönberg, Jaakko Salonen, Tahereh Abad, Janka Biznárová, Marco Caputo, Liangyu Chen, Kestutis Grigoras, Göran Johansson, Anton Frisk Kockum, Christian Križan, Daniel Pérez Lozano, Graham J Norris, Amr Osman, Jorge Fernández-Pendás, Alberto Ronzani, Anita Fadavi Roudsari, Slawomir Simbierowicz, Giovanna Tancredi, Andreas Wallraff, Christopher Eichler, Joonas Govenius, and Jonas Bylander. Building blocks of a flip-chip integrated superconducting quantum processor. *Quantum Science and Technology*, 7(3):035018, jun 2022. doi: 10.1088/2058-9565/ac734b. URL <https://dx.doi.org/10.1088/2058-9565/ac734b>. xiv, 64
- [24] R N. Das, J.L. Yoder, D. Rosenberg, D.K. Kim, D. Yost, J. Mallek, D. Hover, V. Bolkhovskiy, A.J. Kerman, and W.D. Oliver. Cryogenic qubit integration for quantum computing. In *2018 IEEE 68th Electronic Components and Technology Conference (ECTC)*, pages 504–514, 2018. doi: 10.1109/ECTC.2018.00080. xiv, 64
- [25] Richard P Feynman et al. Simulating physics with computers. *Int. j. Theor. phys.*, 21(6/7), 2018. 2
- [26] Paul Benioff. The computer as a physical system: A microscopic quantum mechanical hamiltonian model of computers as represented by turing machines. *Journal of Statistical Physics*, 22(5):563–591, May 1980. 2

- [27] Charles Bennett and Gilles Brassard. Quantum cryptography: Public key distribution and coin tossing. volume 560, pages 175–179, 01 1984. doi: 10.1016/j.tcs.2011.08.039. 2
- [28] David Deutsch and Richard Jozsa. Rapid solution of problems by quantum computation. *Proceedings of the Royal Society of London. Series A: Mathematical and Physical Sciences*, 439(1907):553–558, 1992. doi: 10.1098/rspa.1992.0167. URL <https://royalsocietypublishing.org/doi/abs/10.1098/rspa.1992.0167>. 2
- [29] Ethan Bernstein and Umesh Vazirani. Quantum complexity theory. In *Proceedings of the Twenty-Fifth Annual ACM Symposium on Theory of Computing, STOC '93*, page 11–20, New York, NY, USA, 1993. Association for Computing Machinery. ISBN 0897915917. doi: 10.1145/167088.167097. URL <https://doi.org/10.1145/167088.167097>. 2
- [30] D.R. Simon. On the power of quantum computation. In *Proceedings 35th Annual Symposium on Foundations of Computer Science*, pages 116–123, 1994. doi: 10.1109/SFCS.1994.365701. 2
- [31] P.W. Shor. Algorithms for quantum computation: discrete logarithms and factoring. In *Proceedings 35th Annual Symposium on Foundations of Computer Science*, pages 124–134, 1994. doi: 10.1109/SFCS.1994.365700. 2
- [32] David P. DiVincenzo. The physical implementation of quantum computation. *Fortschritte der Physik*, 48(9-11):771–783, 2000. 2
- [33] Michael Brooks. Beyond quantum supremacy: the hunt for useful quantum computers. , 574(7776):19–21, October 2019. doi: 10.1038/d41586-019-02936-3. 3
- [34] John Preskill. Quantum Computing in the NISQ era and beyond. *Quantum*, 2: 79, August 2018. ISSN 2521-327X. doi: 10.22331/q-2018-08-06-79. URL <https://doi.org/10.22331/q-2018-08-06-79>. 3
- [35] Simon J Devitt, William J Munro, and Kae Nemoto. Quantum error correction for beginners. *Rep Prog Phys*, 76(7):076001, June 2013. 3
- [36] Vikas Hassija, Vinay Chamola, Vikas Saxena, Vaibhav Chanana, Prakhar Parashari, Shahid Mumtaz, and Mohsen Guizani. Present landscape of quantum computing. *IET Quantum Communication*, 1(2):42–48, 2020. 5
- [37] Philipp Gerbert and Frank Rueß. The next decade in quantum computing and how to play. *Boston Consulting Group*, page 5, 2018. 5
- [38] Hongbin Liu, Guang Hao Low, Damian S Steiger, Thomas Häner, Markus Reiher, and Matthias Troyer. Prospects of quantum computing for molecular sciences. *Materials Theory*, 6(1):11, March 2022. 5

- [39] Alejandro Perdomo-Ortiz, Marcello Benedetti, John Realpe-Gómez, and Rupak Biswas. Opportunities and challenges for quantum-assisted machine learning in near-term quantum computers. *Quantum Science and Technology*, 3(3):030502, 2018. 5
- [40] Johannes S Otterbach, Riccardo Manenti, Nasser Alidoust, A Bestwick, M Block, B Bloom, S Caldwell, N Didier, E Schuyler Fried, S Hong, et al. Unsupervised machine learning on a hybrid quantum computer. *arXiv preprint arXiv:1712.05771*, 2017. 5
- [41] Nicolas J. Cerf, Lov K. Grover, and Colin P. Williams. Nested quantum search and structured problems. *Phys. Rev. A*, 61:032303, Feb 2000. doi: 10.1103/PhysRevA.61.032303. URL <https://link.aps.org/doi/10.1103/PhysRevA.61.032303>. 5
- [42] Daniel J. Egger, Ricardo García Gutiérrez, Jordi Cahué Mestre, and Stefan Woerner. Credit risk analysis using quantum computers. *IEEE Transactions on Computers*, 70(12):2136–2145, 2021. doi: 10.1109/TC.2020.3038063. 5
- [43] Michael Marzec. *Portfolio Optimization: Applications in Quantum Computing*, chapter 4, pages 73–106. John Wiley Sons, Ltd, 2016. ISBN 9781118593486. doi: <https://doi.org/10.1002/9781118593486.ch4>. URL <https://onlinelibrary.wiley.com/doi/abs/10.1002/9781118593486.ch4>. 5
- [44] Román Orús, Samuel Mugel, and Enrique Lizaso. Quantum computing for finance: Overview and prospects. *Reviews in Physics*, 4:100028, 2019. ISSN 2405-4283. doi: <https://doi.org/10.1016/j.revip.2019.100028>. URL <https://www.sciencedirect.com/science/article/pii/S2405428318300571>. 5
- [45] Tong Liu, Qi-Ping Su, Jin-Hu Yang, Yu Zhang, Shao-Jie Xiong, Jin-Ming Liu, and Chui-Ping Yang. Transferring arbitrary d-dimensional quantum states of a superconducting transmon qudit in circuit QED. *Scientific Reports*, 7(1):7039, August 2017. 7
- [46] J M Elzerman, R Hanson, L H Willems van Beveren, B Witkamp, L M K Vandersypen, and L P Kouwenhoven. Single-shot read-out of an individual electron spin in a quantum dot. *Nature*, 430(6998):431–435, July 2004. 8
- [47] J. I. Cirac and P. Zoller. Quantum computations with cold trapped ions. *Phys. Rev. Lett.*, 74:4091–4094, May 1995. doi: 10.1103/PhysRevLett.74.4091. URL <https://link.aps.org/doi/10.1103/PhysRevLett.74.4091>. 9
- [48] Kenneth R Brown, John Chiaverini, Jeremy M Sage, and Hartmut Häffner. Materials challenges for trapped-ion quantum computers. *Nature Reviews Materials*, 6(10): 892–905, October 2021. 9
- [49] T. P. Harty, D. T. C. Allcock, C. J. Ballance, L. Guidoni, H. A. Janacek, N. M. Linke, D. N. Stacey, and D. M. Lucas. High-fidelity preparation, gates, memory, and readout of a trapped-ion quantum bit. *Phys. Rev. Lett.*, 113:220501, Nov

2014. doi: 10.1103/PhysRevLett.113.220501. URL <https://link.aps.org/doi/10.1103/PhysRevLett.113.220501>. 9
- [50] C. J. Ballance, T. P. Harty, N. M. Linke, M. A. Sepiol, and D. M. Lucas. High-fidelity quantum logic gates using trapped-ion hyperfine qubits. *Phys. Rev. Lett.*, 117:060504, Aug 2016. doi: 10.1103/PhysRevLett.117.060504. URL <https://link.aps.org/doi/10.1103/PhysRevLett.117.060504>. 9
- [51] Jing Tao, Nam Piau Chew, Luca Guidoni, Yu Dian Lim, Peng Zhao, and Chuan Seng Tan. Fabrication and characterization of surface electrode ion trap for quantum computing. In *2018 IEEE 20th Electronics Packaging Technology Conference (EPTC)*, pages 363–366, 2018. doi: 10.1109/EPTC.2018.8654328. 10
- [52] A.Yu. Kitaev. Fault-tolerant quantum computation by anyons. *Annals of Physics*, 303(1):2–30, 2003. ISSN 0003-4916. doi: [https://doi.org/10.1016/S0003-4916\(02\)00018-0](https://doi.org/10.1016/S0003-4916(02)00018-0). URL <https://www.sciencedirect.com/science/article/pii/S0003491602000180>. 10
- [53] Udagamage Wijewardena. Fractional quantum hall effect under tilted magnetic fields in gaas/algaas heterostructure hall bar devices, and the effect of current annealing in cvd graphene devices. 2023. 10
- [54] Elizabeth Gibney. Inside microsoft’s quest for a topological quantum computer. *Nature*, October 2016. 10
- [55] <https://newsroom.ibm.com/2022-11-09-IBM-Unveils-400-Qubit-Plus-Quantum-Processor-and-Next-Generation-IBM-Quantum-System-Two>, Nov 2022. 11, 16
- [56] Aaron Somoroff, Quentin Ficheux, Raymond A. Mencia, Haonan Xiong, Roman V. Kuzmin, and Vladimir E. Manucharyan. Millisecond coherence in a superconducting qubit, 2021. 11
- [57] Teruaki Yoshioka, Hiroto Mukai, Akiyoshi Tomonaga, Shintaro Takada, Yuma Okazaki, Nobu-Hisa Kaneko, Shuji Nakamura, and Jaw-Shen Tsai. Active initialization experiment of a superconducting qubit using a quantum circuit refrigerator. *Phys. Rev. Appl.*, 20:044077, Oct 2023. doi: 10.1103/PhysRevApplied.20.044077. URL <https://link.aps.org/doi/10.1103/PhysRevApplied.20.044077>. 11
- [58] Liangyu Chen, Hang-Xi Li, Yong Lu, Christopher W Warren, Christian J Križan, Sandoko Kosen, Marcus Rommel, Shahnawaz Ahmed, Amr Osman, Janka Biznárová, Anita Fadavi Roudsari, Benjamin Lienhard, Marco Caputo, Kestutis Grigoras, Leif Grönberg, Joonas Govenius, Anton Frisk Kockum, Per Delsing, Jonas Bylander, and Giovanna Tancredi. Transmon qubit readout fidelity at the threshold for quantum error correction without a quantum-limited amplifier. *npj Quantum Information*, 9(1):26, March 2023. 11

- [59] Ze Li, Ming-Jie Liang, and Zheng-Yuan Xue. Time-optimal universal quantum gates on superconducting circuits. *Phys. Rev. A*, 108:042617, Oct 2023. doi: 10.1103/PhysRevA.108.042617. URL <https://link.aps.org/doi/10.1103/PhysRevA.108.042617>. 11
- [60] Yuan Xu, Ji Chu, Jiahao Yuan, Jiawei Qiu, Yuxuan Zhou, Libo Zhang, Xinsheng Tan, Yang Yu, Song Liu, Jian Li, Fei Yan, and Dapeng Yu. High-fidelity, high-scalability two-qubit gate scheme for superconducting qubits. *Phys. Rev. Lett.*, 125:240503, Dec 2020. doi: 10.1103/PhysRevLett.125.240503. URL <https://link.aps.org/doi/10.1103/PhysRevLett.125.240503>. 11
- [61] Intel. Intel’s new chip to advance silicon spin qubit research for quantum computing, Jun 2023. URL <https://www.intel.com/content/www/us/en/newsroom/news/quantum-computing-chip-to-advance-research.html#gs.08ezd3>. 11
- [62] Kok Wai Chan, Harshad Sahasrabudhe, Wister Huang, Yu Wang, Henry C Yang, Menno Veldhorst, Jason C C Hwang, Fahd A Mohiyaddin, Fay E Hudson, Kohei M Itoh, Andre Saraiva, Andrea Morello, Arne Laucht, Rajib Rahman, and Andrew S Dzurak. Exchange coupling in a linear chain of three Quantum-Dot spin qubits in silicon. *Nano Lett.*, 21(3):1517–1522, January 2021. 11
- [63] Andrea Corna, Léo Bourdet, Romain Maurand, Alessandro Crippa, Dharmraj Kotekar-Patil, Heorhii Bohuslavskiy, Romain Laviéville, Louis Hutin, Sylvain Barraud, Xavier Jehl, Maud Vinet, Silvano De Franceschi, Yann-Michel Niquet, and Marc Sanquer. Electrically driven electron spin resonance mediated by spin–valley–orbit coupling in a silicon quantum dot. *npj Quantum Information*, 4(1):6, February 2018. 11
- [64] Ionq achieves new performance milestone of 29 algorithmic qubits (#aq) on ionq forte. <https://ionq.com/posts/ionq-achieves-new-performance-milestone-of-29-algorithmic-qubits-aq-on-ionq>. 11
- [65] Wonill Ha, Sieu D Ha, Maxwell D Choi, Yan Tang, Adele E Schmitz, Mark P Levendorf, Kangmu Lee, James M Chappell, Tower S Adams, Daniel R Hulbert, et al. A flexible design platform for si/sige exchange-only qubits with low disorder. *Nano Letters*, 22(3):1443–1448, 2021. 11
- [66] C H Yang, R C C Leon, J C C Hwang, A Saraiva, T Tanttu, W Huang, J Camirand Lemyre, K W Chan, K Y Tan, F E Hudson, K M Itoh, A Morello, M Pioro-Ladrière, A Laucht, and A S Dzurak. Operation of a silicon quantum processor unit cell above one kelvin. *Nature*, 580(7803):350–354, April 2020. 11
- [67] Reed W Andrews, Cody Jones, Matthew D Reed, Aaron M Jones, Sieu D Ha, Michael P Jura, Joseph Kerckhoff, Mark Levendorf, Seán Meenehan, Seth T Merkel, Aaron Smith, Bo Sun, Aaron J Weinstein, Matthew T Rakher, Thaddeus D Ladd, and Matthew G Borselli. Quantifying error and leakage in an encoded Si/SiGe triple-dot qubit. *Nature Nanotechnology*, 14(8):747–750, August 2019. 11

- [68] IonQ achieves new performance milestone of 29 algorithmic qubits (#aq) on IonQ forte. <https://ionq.com/posts/ionq-achieves-new-performance-milestone-of-29-algorithmic-qubits-aq-on-ionq>. 11
- [69] Pengfei Wang, Chun-Yang Luan, Mu Qiao, Mark Um, Junhua Zhang, Ye Wang, Xiao Yuan, Mile Gu, Jingning Zhang, and Kihwan Kim. Single ion qubit with estimated coherence time exceeding one hour. *Nature Communications*, 12(1):233, January 2021. 11
- [70] Fangzhao Alex An, Anthony Ransford, Andrew Schaffer, Lucas R. Sletten, John Gaebler, James Hostetter, and Grahame Vittorini. High fidelity state preparation and measurement of ion hyperfine qubits with  $igt; \frac{1}{2}$ . *Phys. Rev. Lett.*, 129:130501, Sep 2022. doi: 10.1103/PhysRevLett.129.130501. URL <https://link.aps.org/doi/10.1103/PhysRevLett.129.130501>. 11
- [71] A. H. Myerson, D. J. Szwer, S. C. Webster, D. T. C. Allcock, M. J. Curtis, G. Imreh, J. A. Sherman, D. N. Stacey, A. M. Steane, and D. M. Lucas. High-fidelity readout of trapped-ion qubits. *Phys. Rev. Lett.*, 100:200502, May 2008. doi: 10.1103/PhysRevLett.100.200502. URL <https://link.aps.org/doi/10.1103/PhysRevLett.100.200502>. 11
- [72] J. P. Gaebler, T. R. Tan, Y. Lin, Y. Wan, R. Bowler, A. C. Keith, S. Glancy, K. Coakley, E. Knill, D. Leibfried, and D. J. Wineland. High-fidelity universal gate set for  ${}^9\text{Be}^+$  ion qubits. *Phys. Rev. Lett.*, 117:060505, Aug 2016. doi: 10.1103/PhysRevLett.117.060505. URL <https://link.aps.org/doi/10.1103/PhysRevLett.117.060505>. 11
- [73] A. Bermudez, X. Xu, R. Nigmatullin, J. O’Gorman, V. Negnevitsky, P. Schindler, T. Monz, U. G. Poschinger, C. Hempel, J. Home, F. Schmidt-Kaler, M. Biercuk, R. Blatt, S. Benjamin, and M. Müller. Assessing the progress of trapped-ion processors towards fault-tolerant quantum computation. *Phys. Rev. X*, 7:041061, Dec 2017. doi: 10.1103/PhysRevX.7.041061. URL <https://link.aps.org/doi/10.1103/PhysRevX.7.041061>. 11
- [74] Lieven M K Vandersypen, Matthias Steffen, Gregory Breyta, Costantino S Yannoni, Mark H Sherwood, and Isaac L Chuang. Experimental realization of shor’s quantum factoring algorithm using nuclear magnetic resonance. *Nature*, 414(6866):883–887, December 2001. 13
- [75] Stephan Gulde, Mark Riebe, Gavin P T Lancaster, Christoph Becher, Jürgen Eschner, Hartmut Häffner, Ferdinand Schmidt-Kaler, Isaac L Chuang, and Rainer Blatt. Implementation of the Deutsch–Jozsa algorithm on an ion-trap quantum computer. *Nature*, 421(6918):48–50, January 2003. 13
- [76] L DiCarlo, J M Chow, J M Gambetta, Lev S Bishop, B R Johnson, D I Schuster, J Majer, A Blais, L Frunzio, S M Girvin, and R J Schoelkopf. Demonstration of two-qubit algorithms with a superconducting quantum processor. *Nature*, 460(7252):240–244, July 2009. 13

- [77] Jonathan Wei Zhong Lau, Kian Hwee Lim, Harshank Shrotriya, and Leong Chuan Kwek. NISQ computing: where are we and where do we go? *AAPPS Bulletin*, 32(1):27, September 2022. 13
- [78] Austin G. Fowler, Matteo Mariantoni, John M. Martinis, and Andrew N. Cleland. Surface codes: Towards practical large-scale quantum computation. *Phys. Rev. A*, 86:032324, Sep 2012. doi: 10.1103/PhysRevA.86.032324. URL <https://link.aps.org/doi/10.1103/PhysRevA.86.032324>. 13
- [79] Atom Computing. Quantum startup Atom Computing first to exceed 1,000 qubits, 10 2023. URL <https://atom-computing.com/quantum-startup-atom-computing-first-to-exceed-1000-qubits/>. 14
- [80] IBM. IBM Quantum Computing — Roadmap, 2023. URL <https://www.ibm.com/quantum/roadmap>. 14
- [81] Sundar Pichai. What our quantum computing milestone means. 10 2019. URL <https://blog.google/technology/ai/what-our-quantum-computing-milestone-means/>. 14
- [82] Stefano Pellerano, Sushil Subramanian, Jong-Seok Park, Bishnu Patra, Todor Mladenov, Xiao Xue, Lieven M. K. Vandersypen, Masoud Babaie, Edoardo Charbon, and Fabio Sebastiano. Cryogenic cmos for qubit control and readout. In *2022 IEEE Custom Integrated Circuits Conference (CICC)*, pages 01–08, 2022. doi: 10.1109/CICC53496.2022.9772841. 14, 16
- [83] K. Bertels, A. Sarkar, and I. Ashraf. Quantum computing—from nisq to pirq. *IEEE Micro*, 41(05):24–32, sep 2021. ISSN 1937-4143. doi: 10.1109/MM.2021.3099195. 15
- [84] Chenlu Wang, Xuegang Li, Huikai Xu, Zhiyuan Li, Junhua Wang, Zhen Yang, Zhenyu Mi, Xuehui Liang, Tang Su, Chuhong Yang, Guangyue Wang, Wenyan Wang, Yongchao Li, Mo Chen, Chengyao Li, Kehuan Linghu, Jiaxiu Han, Yingshan Zhang, Yulong Feng, Yu Song, Teng Ma, Jingning Zhang, Ruixia Wang, Peng Zhao, Weiyang Liu, Guangming Xue, Yirong Jin, and Haifeng Yu. Towards practical quantum computers: transmon qubit with a lifetime approaching 0.5 milliseconds. *npj Quantum Information*, 8(1):3, January 2022. 16
- [85] B.D. Josephson. Possible new effects in superconductive tunnelling. *Physics Letters*, 1(7):251–253, 1962. ISSN 0031-9163. doi: [https://doi.org/10.1016/0031-9163\(62\)91369-0](https://doi.org/10.1016/0031-9163(62)91369-0). URL <https://www.sciencedirect.com/science/article/pii/0031916362913690>. 22
- [86] Dennis Wang, Priti Shah, Marco Facchini, John Blair, Jeremy Drysdale, Thomas McConkey, and Zlatko Minev. A framework for quantum device design-project qiskit metal. In *APS March Meeting Abstracts*, volume 2021, pages J30–011, 2021. 32
- [87] T. Yamamoto, K. Koshino, and Y. Nakamura. *Parametric Amplifier and Oscillator Based on Josephson Junction Circuitry*, pages 495–513. Springer Japan, Tokyo,

2016. ISBN 978-4-431-55756-2. doi: 10.1007/978-4-431-55756-2\_23. URL [https://doi.org/10.1007/978-4-431-55756-2\\_23](https://doi.org/10.1007/978-4-431-55756-2_23). 44
- [88] Tanay Roy, Sumeru Hazra, Suman Kundu, Madhavi Chand, Meghan P. Patankar, and R. Vijay. Programmable superconducting processor with native three-qubit gates. *Phys. Rev. Appl.*, 14:014072, Jul 2020. doi: 10.1103/PhysRevApplied.14.014072. URL <https://link.aps.org/doi/10.1103/PhysRevApplied.14.014072>. 56, 58
- [89] Kangdi Yu, Murat C Sarihan, Jin Ho Kang, Madeline Taylor, Cody S Fan, Ananyo Banerjee, Jonathan L DuBois, Yaniv J Rosen, and Chee Wei Wong. Stochastic modeling of superconducting qudits in the dispersive regime. *arXiv preprint arXiv:2310.18856*, 2023. 59
- [90] Ricardo I. Amils, Juan Daniel Gallego, José Luis Sebastián, Sagrario Muñoz, Agustín Martín, and Arnulf Leuther. Thermal conductivity of silver loaded conductive epoxy from cryogenic to ambient temperature and its application for precision cryogenic noise measurements. *Cryogenics*, 76:23–28, 2016. ISSN 0011-2275. doi: <https://doi.org/10.1016/j.cryogenics.2016.03.001>. URL <https://www.sciencedirect.com/science/article/pii/S0011227515300400>. 67
- [91] Tanay Roy, Madhavi Chand, Anirban Bhattacharjee, Sumeru Hazra, Suman Kundu, Kedar Damle, and R. Vijay. Multimode superconducting circuits for realizing strongly coupled multiqubit processor units. *Phys. Rev. A*, 98:052318, Nov 2018. doi: 10.1103/PhysRevA.98.052318. URL <https://link.aps.org/doi/10.1103/PhysRevA.98.052318>. 75